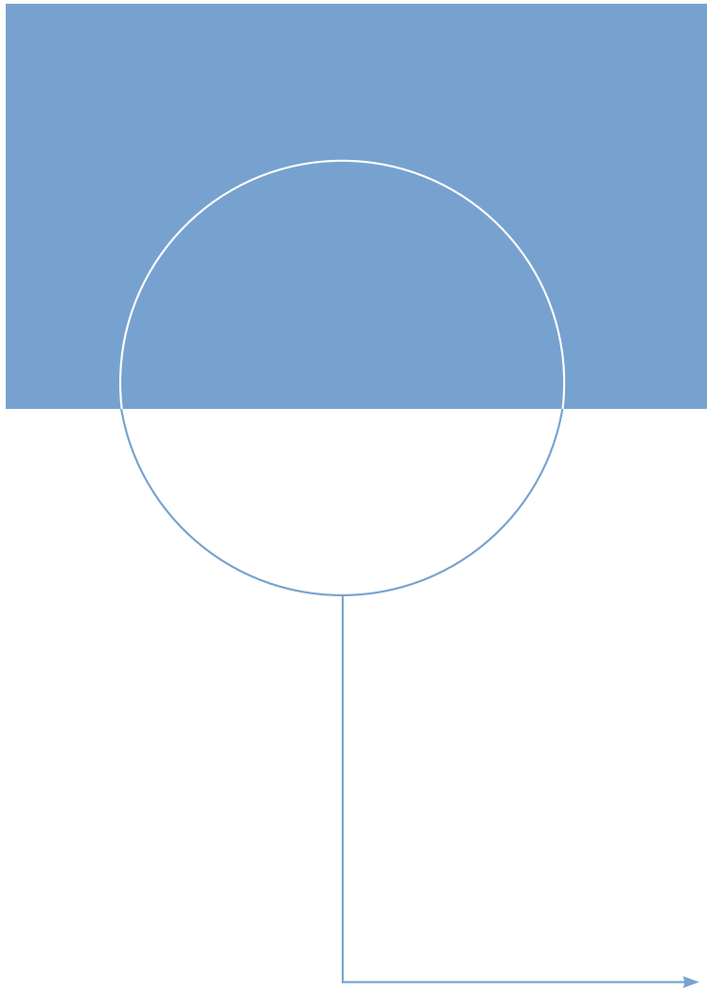

Master's thesis

2022

Lukas Okkenhaug Hartnik

NTNU
Norwegian University of
Science and Technology
Faculty of Engineering
Department of Civil and Environmental Engineering

Lukas Okkenhaug Hartnik

Experimental Study of Submarine Landslides and Impact Forces on Offshore Constructions

February 2022

NTNU
Norwegian University of
Science and Technology

NTNU
Norwegian University of
Science and Technology

NTNU
Norwegian University of
Science and Technology

Experimental Study of Submarine Landslides and Impact Forces on Offshore Constructions

Lukas Okkenhaug Hartnik

Civil and Environmental Engineering
Submission date: February 2022
Supervisor: Gudmund Reidar Eiksund
Co-supervisor: Erik Sørlie

Norwegian University of Science and Technology
Department of Civil and Environmental Engineering

Preface

This document constitutes my master's thesis (30 ECTS credits) in geotechnical engineering. It is written in relation with the course TBA4900, Geotechnical Engineering Master Thesis, and concludes 4.5 years of study at the Department of Civil and Environmental Engineering at the Norwegian University of Science and Technology (NTNU). The work is carried out during the fall and winter of 2021 and 2022.

The topic of this thesis was suggested by prof. Gudmund Eiksund (main supervisor) as a part of a research program related to submarine landslide and relating impact forces. The study is carried out in collaboration with the PhD project of Erik Sørlie titled "*Impact of Submarine Slides on Anchorage Systems*". This study is funded by Statens Vegvesen and NTNU in connection with the development of a fjord crossing over Bjørnafjorden related to ferry free E39.

First and foremost, I want to thank my Co-Supervisor, Erik Sørlie, for all valuable help, support, and good discussions throughout this thesis. I would also like to thank my supervisor Gudmund Eiksund for valuable guidance and Dr. Quoc Thran, Karl Ivar Kvisvik and Espen Andersen for vital assistance and guidance regarding laboratory testing.

In addition, I would like to express my gratitude to NGI for disposing personnel and equipment to conduct a cyclic DSS survey and Dr. Rune Dyvik (NGI) for providing valuable insight to these tests.

Finally, I want to thank family and friends for providing support and encouragement through this time.

Trondheim, Norway – 19.02.2022

Lukas Okkenhaug Hartnik

Summary and Conclusion

The Norwegian Ministry of Transport has engaged Statens Vegvesen to develop a proposal for a ferry free E39 (coastal highway) between Trondheim and Kristiansand. Today this 1100km coastal corridor accommodates 8 ferry connections uniting important cities and securing export of goods on the west coast of Norway. For Bjørnafjorden, one of the planned fjord crossings, a side anchored floating bridge is to be constructed where the mooring system will be anchored on the 500m deep seabed exposed to steep slopes. To better understand the submarine environment, relating geohazards and the bridge foundations integrity towards possible submarine landslides, computational and numerical models are being developed. These models rely on accurate input parameters, which subsequently are established through experimental model testing and soil analysis.

This thesis will investigate the slide behavior from initiation phase until impact phase, and further explore the effects of impact forces on submarine constructions of clay rich submarine landslides through small scale model flume tests using kaolin clay. To form an understanding of the soil behavior through various slide phases and impact, a supplementary soil investigation of kaolin is completed. Finally, to demonstrate a link to field conditions, the slide and impact behavior has been characterized through dimensionless number as well as that rheological and geotechnical properties of kaolin clay and clay from Bjørnafjorden (BF clay) has been compared.

Capturing the soil behavior through various phase transitions with the corresponding impact force in a submarine landslide represents a particular challenge. The original soil is typically characterized using traditional geotechnical methods, however, through a submarine landslide the soil will experience increased remolding and water entrainment, converting the soil to a fluid, as the slide progresses. Due to the solid to fluid transition, characterizations of soil/fluid strength are being addressed separately within the mechanical framework, resulting in both a fluid mechanical and a geotechnical approach.

To solve this, an extensive soil investigation based on fall cone, T-bar, viscometer, cyclic DSS and cyclic triaxial tests is conducted on kaolin clay and BF clay to investigate the strength and strain rate dependency of both materials. The soil characteristics were further mapped through hydrometer, pycnometer and Atterberg limit tests. Soil strength and strain rate dependency were, together with Herschel-Bulkley approximations, important for displaying the strength behavior with increasing water content. A total of 27 fall cone, 18 T-bar, 9 viscometer, 6 cyclic DSS and 6 cyclic triaxial tests were conducted. Kaolin and BF clay have been presented and compared using the liquidity index (LI), which has proven to be a suitable normalization when comparing both materials. The soil investigation ranged from LI:0.21-1.62 for BF clay and LI:0.82-3.05 for kaolin clay, exposing both soils to the transition of remolded and plastic state to fluid/liquid state.

Analysis of the results shows clear tendencies between kaolin and BF clay. The variation in yield stress and shear strength due to water entrainment can be described by unique power functions of liquidity index. Furthermore, the strain rate dependency over the solid to liquid range seems to deteriorate with increased water content, exhibiting a decreased strain rate dependency with increased LI. This results into material characteristics which seems to be dominated by the

transition from solid to fluid state where both materials exhibit non-Newtonian behavior for increased shear rate.

The model slides were investigated for kaolin at various water contents ranging between 80-113% using 2 slope angles, namely 12° and 18°. In total, 3 experiments were completed investigating slide runout, while 18 experiments were completed investigating impact force responses. The model slides were monitored through pore water pressure measurements, impact force response, total force response and video recordings.

The results showed an increased coherency with decreased water content which ranged between strongly coherent flow and weakly coherent flow depending on water content. A thin water layer, identified as hydroplaning, can be observed for all tests as it intrudes underneath the flow head after initiation and provides an efficient lubrication layer causing the slide to accelerate. The hydroplaning and flow coherency were further portrayed through empirical relations showing good agreement with the literature.

Based on the 3 slide runout trials, a clear relation towards clay rheology, hydroplaning and volume effects could be found, where increased water content and greater discharge volume implies longer runout distance as long as hydroplaning occurs. The impact forces were analyzed through a fluid dynamic approach using the rheological properties to establish the non-Newtonian Reynolds number. The measured impact force response corresponds to the drag force and exhibits a greater dependency towards water content and discharge volume than velocity. The impact force results were further evaluated through the established drag coefficient which is finally validated through an empirical approximation from literature.

Sammendrag

Samferdselsdepartementet har engasjert Staten Vegvesen til å utvikle et forslag om fergefri E39 mellom Kristiansand og Trondheim. I dag omfatter denne 1100km lange kystkorridoren 8 fergeforbindelser som forener viktige byer og sikrer eksport av varer på vestkysten av Norge. For Bjørnafjorden, en av de planlagte fjordkryssingene, skal det bygges en sideforankret flytebro der fortøyningssystemet skal forankres på den 500m dype havbunnen eksponert mot bratte skråninger. For å bedre forståelsen av de undersjøiske grunnforholdene, relaterte geofarer og brofundamentets integritet mot potensielle undersjøiske skred, utvikles det en beregningsmetodikk og tilhørende numeriske modeller for å kartlegge effekter og prosesser rundt submarin massetransport. Disse modellene er avhengige av representative inputparametere som etableres gjennom modelltesting og eksperimentell analyse av aktuelle løsmasser.

Denne oppgaven undersøker skredoppførselen fra initieringsfase til kollisjonfase, i tillegg til effekten av kollisjonskrefter på undersjøiske konstruksjoner fra leirrike undersjøiske skred. Dette er gjort gjennom en omfattende studie basert på småskala modelltester som skal simulerer undersjøiske skred gjennom ulike faser ved bruk av kaolin leire.

For å oppnå en forståelse av materialoppførselen gjennom ulike skredfaser og effekten av skredkollisjoner, er det gjennomført en supplerende materialstudie på kaolin. For å demonstrere en kobling til forhold i Bjørnafjorden, har leire fra Bjørnafjorden (BF leire) blitt karakterisert på samme måte som kaolin og sammenlignet i ettertid. Avslutningsvis har skredoppførselen og kollisjonsresponsen blitt karakterisert gjennom dimensjonsløse parametere for sammenligning med litteratur og å kunne skalere opp modellforsøkene til simulering av fullskala skred.

Å karakterisere materialoppførselen i et undersjøisk skred gjennom ulike faseoverganger med resulterende kollisojnskrefter, representerer en spesiell utfordring. Styrkeegenskaper i løsmasser blir normalt klassifisert gjennom geotekniske metoder, men i et undersjøisk skred vil skredmassene oppleve en økt omrøring og vanninntrenging. Ettersom skredet utvikler seg, vil vanninntrengingen bli større og de geomekaniske egenskapene endres. Dette fører til at det ellers faste og plastiske materialet vil oppleve en mindre partikkel-partikkel kontakt som gir materialet en mer viskøs oppførsel. På grunn av overgangen fra fast stoff til væske behandles karakteriseringen av løsmasse/væske separat innenfor det mekaniske rammeverket. Dette fører videre til to tilnærminger for å karakterisere materialegenskapene i et materiale, nemlig en geoteknisk og en fluid dynamisk tilnærming.

For å løse dette ble det gjennomført en omfattende laboratorietesting som omfattet konus, T-bar, viskometer, syklisk DSS og sykliske triaksialforsøk på kaolin og BF leire. Testresultatene har blant annet dokumentert styrke- og tøyningshastighetsavhengigheten til begge materialene. Kartlegging av indeks parametere har blit identifisert gjennom hydrometer, pyknometer og Atterberg grenser. Styrkeegenskapene og rate-avhengigheten for varierende vanninnhold danner, sammen med Herschel Bulkley approksimasjoner, hovedtyngden i denne materialanalysen. Totalt ble det utført 27 konus, 18 T-bar, 9 viskometer, 6 sykliske DSS og 6 sykliske triaksialtester. Kaolin og BF leire er presentert og sammenlignet på likviditetsindeksen (LI) som har vist seg å være en passende normalisering når materialene sammenlignes. Resultatene varierer fra LI:0.21-1.62 for BF-leire og

LI:0.82-3.05 for kaolinleire, godt innenfor intervaller som utsetter begge materialene for både en plastisk og flytende materialtilstand.

Analyse av resultatene viser klare tendenser mellom kaolin og BF leire. Variasjoner i bruddspenningen og skjærstyrken på grunn av økt vanninntrenging kan beskrives gjennom unike power funksjoner på bakgrunn av LI. Videre ser det ut til at rate-avhengigheten avtar med økende LI. Dette indikerer materialegenskaper som ser ut til å være dominert av overgangen fra fast til flytende tilstand, hvor begge materialer viser ikke-Newtonisk oppførsel for økt skjærhastighet.

Modellforsøkene ble undersøkt for kaolin med vanninnhold mellom 80-113% ved bruk av en skredbane utsatt for 2 helninger, 12° og 18°. Totalt ble det gjennomført 3 forsøk for å undersøke utløpsdistanse for skredet, og 18 forsøk ble gjennomført for å undersøke skredkollisjon. Skredoppførselen ble fanget opp gjennom poretrykksmålinger, totalkraftmåler, kollisjonsmåler og videoopptak.

Resultatene viser en økt koherens med redusert vanninnhold. Denne materialegenskapen varierte med endring i vanninnhold og kunne variere fra sterkt koherent til svakt koherent materialoppførsel. Et tynt vannlag, identifisert som vannplaning, ble observert for alle testene. En slik mekanisme reduserer friksjonen mellom skredmassene og underlaget som igjen fører til en akselerasjon av skredet etter initiering. Vannplaning og strømningsegenskapene er ytterligere blitt skildret gjennom empiriske relasjoner, hvor resultatene viste godt samsvar med litteraturen.

Basert på utløpsforsøkene, kunne man finne en klar relasjon til material-reologi, vannplaning og volumeffekter, hvor økt vanninnhold og større utslippsvolum gir lenger utløpsdistanse forutsatt at vannplaning forekommer. Effekter av skredkollisjoner ble analysert gjennom en reologisk og fluid dynamisk tilnærming ved å etablere en ikke-Newtonisk Reynolds tall-formulering. Den målte kollisjonsresponsen viser en større avhengighet av vanninnhold og utslippsvolum enn hastighet. Kollisjonsresponsen ble videre analysert gjennom en etablert drag-koeffisient og videre validert opp mot empiriske modeller fra litteraturen.

Table of Contents

List of Tables

List of Figures

Acronyms

Symbols

A_c	Activity of clay	$-$
CF	Clay fraction	%
C_u	Unremolded shear strength	Pa
C_{ur}	Remolded shear strength	Pa
C_{urcf}	Fall cone remolded shear strength	Pa
C_d	Drag coefficient	$-$
D_m	Internal diameter of membrane	mm
F_{rd}	Froude Number	$-$
h	Height of inner cylinder	mm
H_z	Hertz	$1/s$
L	Slide runout distance	cm
LI	Liquidity Index	$-$
I_P	Plasticity index	$-$
K	Consistency coefficient	$Pa \cdot s^n$
K	Correlation coefficient	$-$
m_c	Mass of clay grains	g
m_W	Mass of water	g
m_S	Mass of solids	g
N	Rotation speed	Rps
n	Herschel-Bulkley exponent	$-$
r	Radial cylinder coordinate	mm
r_u	Pore water pressure ratio	$-$
R^2	Coefficient of determination	$-$
R_i	Rotor radius	mm
R_0	Outer cylinder radius	mm
$Re_{non-Newtonian}$	Non-Newtonian Reynolds Number	$-$
S	Salinity	g/L
S_t	Sensitivity	$-$
$S_{u_{rem}}$	Remolded shear strength	Pa
S_u	Unremolded shear strength	Pa
T	Torque	mNm
u	Pore pressure	kPa
v	velocity	m/s
w	Water content	%
w_c	Water content	%
w_L	Liquid limit	%
w_P	Plastic limit	%
W_r	Initial weight	g
W_L	Discharge weight	g
Q	Impact force	kN

Greek symbols

γ	Shear strain	%
$\dot{\gamma}$	Shear strain rate	s^{-1}
$\dot{\gamma_{ref}}$	Reference shear rate	s^{-1}
τ	Shear stress	Pa
τ_0	Reference shear stress	Pa
τ_c	Yield stress	Pa
τ_f	Dynamic pressure	Pa
τ_y	Yield stress	Pa
τ_r	Residual stress	Pa
τ_{rem}	Remolded shear stress	Pa
ω	Angular velocity at radius r	rad/s
η	Viscosity	$Pa \cdot s$
ε	Strain	%
ρ	Density	g/cm^3
ρ_d	Solid density	g/cm^3
ρ_w	Water density	g/cm^3
σ	Stress	kPa
σ_c	Consolidation stress	kPa
σ_e	Effective stress	kPa

Abbreviations

1D	1-Dimensional
2D	2-Dimensional
BF	Bjørnafjorden
CSL	Critical State Line
CPTu	Cone Penetration Test
DSScy	Cyclic Direct Simple Shear
ESP	Effective Stress Path
FE	Finite Element
fps	Frames Per Second
Kyr	Thousand Years
MC	Mohr Coulomb
NGI	Norwegian Geotechnical Institute
NTNU	Norwegian University of Technology and Science
PWP	Pore Water Pressure

1. Introduction

1.1 Background

The Norwegian Ministry of Transport has engaged Statens Vegvesen to develop a proposal for a ferry free E39 (coastal highway) between Trondheim and Kristiansand. Today this 1100km coastal corridor accommodates 8 ferry connections uniting important cities and securing export of goods on the west coast of Norway. Most of these ferry connections consists of wide and deep fjord crossings which will require massive investments containing larger and longer spanning structures exposed to greater and more complex hazards than before. The choice of concept from The Ministry of Transport suggests a fjord crossing over Bjørnafjorden which promotes a bridge connection between Reksteren and Os. This project, Hordfast, along with remaining E39 related projects between Bergen and Stavanger is estimated to abbreviate the travel time from 4.5 hours to 2 hours (SVV, 2021).

The planned bridge will cross water depths of 500 meters and have an approximate length of 5 km. Such wide bridge spans over deep fjords limits design concepts to only contain floating bridges. For design purposes of an anchored floating bridge, challenges of controlling the lateral movement of a floating bridge can be identified as one of the main concerns. The current solution suggests 16 anchors divided into 4 pontoons, anchored on both sides of the bridge, illustrated in Figure 1. 1.

Bathymetric investigations from Bjørnafjorden reveal an asymmetrical fjord with an undulating seafloor. Figure 1. 1 displays steep slopes on the southern side while the north side consists of a shallower depth from about 50-150m, which mainly is made up of exposed bedrock. The basin, which constitutes the main part of the crossing, has a depth of about 550m characterized by steep flanks and large sediment deposits. The considered anchors can be classified into three groups: suction anchor, gravity anchor, and a mix of both. Seabed deposition and topography determines the type of anchor where gravity anchors are used at locations exposed to bedrock while suction anchors are used at spots with larger deposit of sediments or where inclination exceeds 5 degrees.

The sediment deposition in Bjørnafjorden is a result of heavy glacier activity the last 500kyr. where most sediments originate from the last 25 kyr. The shaped stratigraphy we see today can be explained by the deglaciation phases from this time. The first phase is characterized by a warmer climate causing the ice front to melt making the ice mass retreat to the mainland. The second phase is known as Younger Dryas (11.5-12.8 kyr.) and can be characterized by a climate change towards colder temperatures. This made the glaciers readvance, an ice expansion that can be seen through moraine deposits over large parts of mainland Norway. Phase 3 symbolizes the end of the ice age where the climate becomes warmer and stabilizes. These deglaciation processes caused large depositions of glaciomarine and hemipelagic sediments which dominates the seabed of Bjørnafjorden today (NGI, 2019c).

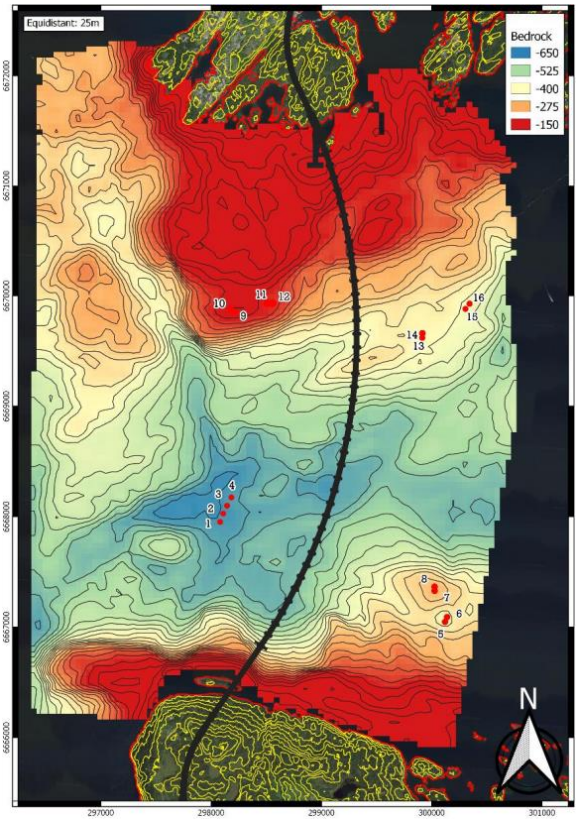

Figure 1. 1:Bathymetric image of Bjørnafjorden with calculated depth to bedrock. Point 1 – 16 represents suggested anchor locations while bedrock color signal depth beneath sea level. The black line represents the planned bridge (SVV, 2019)

Submarine instability and relating geohazards are considered as an important concern regarding the construction of the bridge. To maintain a proper understanding of the submarine environment and the relating geohazards in Bjørnafjorden, an extensive soil investigation survey was conducted by Fugro and Norges Geotekniske Institutt (NGI). The soil investigation included 21 borehole locations consisting of Cone Penetration tests (CPTUs), Seismic Cone Penetration tests (SCPTUs), pore pressure dissipation measurements and soil sampling. These results are summarized in 3 reports (NGI, 2019a, 2019b, 2019c) evaluating the soil properties, slope stability and recommendations regarding anchor locations. However, the anchor foundation integrity to possible future slide events remains an important design consideration, which required more detailed studies.

This thesis is a part of an ongoing research project at NTNU on submarine landslides in Bjørnafjorden and the development of a relating numerical model. To establish framework conditions, a series of 21 model tests of small-scale submarine landslide have been conducted to create a foundation for developing such a model. To get a proper understanding of the slide behavior and impact forces in the model tests, an understanding of the clay properties and behavior regarding Bjørnafjorden sediments (BF sediments), and kaolin clay (chosen model clay) will be crucial.

1.2 Scope

The scope of this thesis is to investigate the slide behavior of clay rich submarine landslides from initiation phase until impact phase, and further explore the effects of impact forces on submarine constructions. In addition, material behavior related to flow characteristics and slide development regarding constant remolding, water intrusion and slide impact are to be understood. Being able to realistically capture the flow behavior and slide impacts of clay rich debris flows and further describe the underlying material response, may form the foundation for establishing a numerical tool to simulate clay rich submarine landslides and relating impact forces.

1.3 Approach

The scope is to be approached by preforming experimental model flume tests involving both runout and impact simulations of clay rich submarine landslides. In order to obtain a sufficient understanding of mechanisms and behavior related to clay rich submarine landslides at various flow states, a set of model tests with changing water content, initial material state and slope angle are to be investigated. By using kaolin clay as model clay, large amounts of test material can be used, assuring that a comprehensive model slide investigation can be achieved.

To establish a proper understanding of the model test, results and underlying material behavior during the model slide events, rheological and geotechnical properties of kaolin must be studied through laboratory experiments. A similar study can be conducted on clay from Bjørnafjorden and further compared with kaolin clay to demonstrate a link between model tests and conditions in Bjørnafjorden.

1.4 Objectives

The following objectives can be presented based on the scope and approach of this thesis:

- Investigate the slide behavior of kaolin with various water content through small scale model tests and examine the relating effects of impact forces according to a fluid dynamic approach.
- Characterize and study the geotechnical and rheological properties of kaolin and Bjørnafjorden clay through hydrometer, fall cone, pycnometer, viscometer, T-bar, cyclic triaxial and cyclic DSS tests for changing water content.
- Compare the material behavior regarding kaolin and Bjørnafjorden clay to evaluate kaolin as a model clay and demonstrate a link between model tests and conditions in Bjørnafjorden.

1.5 Limitations

Several limitations can be introduced regarding the experimental model slide investigation and relating laboratory study.

- Slide triggering mechanisms are not studied in this thesis. All model tests are triggered using identical mechanism.
- Flow mechanisms related to slide material – impact pile interaction is not considered due to practical challenges.
- Flow characteristics related runout simulations are not monitored with video recordings after the runout channel.
- Only clay rich debris flow containing kaolin were studied, hence no material compositions related to clay-sand ratio was investigated.
- Soil that exhibits fluid characteristics, such as slurries or debris flows, may not be properly characterized by geotechnical testing methods. On the other side, rheometric tests such as viscometer tests are developed to characterize mechanical behavior of fluids with low strengths, making measurements of consolidated or firm soil difficult. This constitutes a device limitation when investigating the transition from solid to fluid state.
- Temperature and salinity dependency related to flow characteristics, strain rate dependency and strength characteristics has not been teste. It is, however, pointed out and discussed for viscometer tests.

1.6 Reference Made to Preliminary Study

Preliminary studies were carried out during the spring of 2021. The scope was to evaluate kaolin clay as model clay for Bjørnafjorden clay (From now on BF clay), which mainly consisted of viscometer studies of kaolin and BF clay. The preliminary studies form the unpublished work of the project thesis with the title: *E39 – Fjord crossing over Bjørnafjorden: The use of kaolin as a model clay for submarine slides* by Hartnik (2021), which constitutes the course TBA4510 holding 7.5 credits. Hence, several paragraphs and statements, possibly containing some modifications, are adopted. The respective paragraphs this applies to can summarized into:

- Chapter 1
- Chapter 2 (Specifically, chapter 2.4)
- Chapter 3 in general (chapter 3.1 to 3.5)
- Parts of chapter 5.1.5, particularly limitations related to viscometer testing.

1.7 Structure of the Thesis

This thesis is made up of 6 chapters including this introduction.

Chapter 1 – Gives an introduction to the project and covered topic, presenting the motivation alongside scope, approach, objectives and limitations.

Chapter 2 – Presents the literature review on fine-grained soil flow behavior, submarine slide processes and mass wasting, rheology and viscosity and their applications in geotechnical engineering. Important parameters affecting clay rheology and non-dimensionalized numbers describing flow characteristics and impact forces of submarine landslides slides are also introduced.

Chapter 3 – Gives an extensive introduction to conducted laboratory experiments including a description of materials tested.

Chapter 4 – Introduces to conducted model flume test and data processing.

Chapter 5 – Gives a detailed presentation and a critical discussion of obtained results from laboratory experiments and model tests. The discussion tries to describe and justify the model flume results based on obtained material understanding established from the laboratory tests.

Chapter 6 – Summarizes and concludes the conducted work in this thesis. In addition, recommendation of further work is suggested.

Appendix A – Cyclic triaxial tests

Appendix B – Cyclic DSS tests

Appendix C – Step by step procedure for conducted model flume tests.

2. Submarine Landslides and Properties of Rheology

2.1 Introduction

Submarine landslide constitutes an important agent of sediment transport across fjords and the continental shelf into the deep ocean bed (Masson et al., 2006). Sediments that are derived from land are transported by rivers until frictional energy exceeds the kinetic energy governed by the water flow, making the material deposit. This results in a grading of the material where coarser and granular material will deposit early and finer sediments, such as silt and clay, can travel until it reaches stagnant water. However, this deposition stage is normally a temporary storage, as accumulation of fine sediments can lead to slope instability ultimately leading to slope failure. Such failures can happen instantly and form landslides causing onward transport of the deposits. This constitutes a significant hazard for offshore constructions and life due to large mass movement and subsequent tsunami development.

Such large and instant sediment transports in water are highly affected by flow characteristics. Traditionally, landslide mobility is expressed based on slide characteristics from onshore slides. These methods are often based on geometrical description of slide runouts described by the horizontal runout distance and the vertical height drop. However, such methods are not sufficient to capture the fluidization process in submarine slides (Jeong et al., 2015). Literature ((Blasio et al., 2006; S. W. Jeong et al., 2015; Kvalstad et al., 2005) highlights 3 transitional mechanisms that influences the runout distance and the potential impact force: wetting, remolding and hydroplaning. Wetting can be considered as a progressive reduction of material shear strength as a consequence of increased water intrusion. Wetting and remolding will create a dilute suspension of sediments with a lower shear strength compared to the prior dense mass in a submarine slide. Such a process, where dens and firm sediments transforms to a thin diluted suspension, is what Fisher (1983) characterizes as *flow transformation.* To describe the transition from solid to liquid phase, both rheological and geotechnical characteristics of fine-grained sediments close to the transition area must be examined. Flow conditions, such as hydroplaning, will, together with material behavior, be the main influencers affecting a submarine slide.

This chapter will introduce debris flows and elements affecting impact forces from submarine slides on offshore structures. This relates to theoretical aspects of rheology combined with geotechnical properties connected to rheology and flow dynamics. These elements are key aspects of understanding the soil properties and soil behavior through the different phases of a submarine slide.

2.2 Slide Process and Mass Transport

Submarine slide processes are in general closely related and dependent on the material transitions from solid to liquified state. The slide behavior is closely related the material development and can be identified through 3 main phases: initial failure and formation of blocks and slabs, debris flows and turbidity currents (Figure 2. 1) (Bryn et al., 2005).

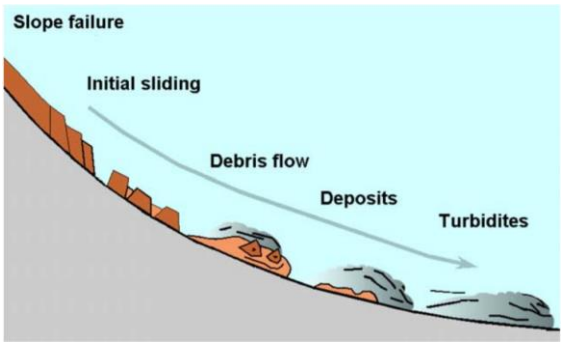

Figure 2. 1:Schematic illustration of the different stages/phases of a submarine slide form (Bryn et al., 2005)

The soil properties together with the seabed morphology and slide flow behavior are considered decisive in how these phases will occur. High velocity, mobility and large outruns of the slide sediments are important elements for the materials to reach debris flow, or even turbidities stage. Slide blocks with fine grained materials will be able to develop high velocities generating a high pressure close to the front of the slab which over time will cause remolding and wetting, further affecting the material composition. Remolded clay combined with lubrication by water entrainment and hydroplaning is considered as an explanation of the high mobility and flow transformation of slide sediments (Bryn et al., 2005).

Based on a geotechnical standpoint, initial failure will inflict large shear deformations and fracturing on the slide masses. A transitional process like this together with water intrusion due to remolding, will reduce the inherent shear strength. This process can be considered as the transition from solids to fluid. The water intrusion will influence the solid/water ratio, improving the soil mobility and reducing the shear strength. At sufficiently low shear strength the particles are unable hold their structure and flow will occur (Jeong et al., 2015).

A rheological standpoint explains the behavior of soil properties by evaluating the rate dependency of a material dissolved in a water. The designation of materials suspended in water can be characterized as viscosity, a material parameter which can measured through strength, creep and compressibility(Jeong et al., 2015). In sediment rheology, viscosity is obtained from normalized flow curves. These strength parameters presented in normalized flow curves can be considered important for understanding the rheological transformation from initial failure and post failure. Through the transition from sliding blocks to debris flows, the dominance of Coulomb frictional behavior and viscosity effects changes towards viscous behavior (Ilstad et al., 2004). Flow modelling presents several models for detecting the shear strength, τ, at determined strain rate, $\dot{\gamma}$. These models describes the inherent viscosity of a material, which according Jeong et al. (2015) can be further used to establish an understanding of the viscous behavior of soils close to the transition of solid to fluid behavior.

2.3 Relationship Between Water Content and Shear Strength

By including pre-failure to Bryn et al. (2005) original description of submarine slides, the full strength evolution for fine grained sediments can be captured. This expands now to four stages: pre-failure (I), failure (II), post-failure (III), and flow (IV). Figure 2. 2 illustrates the strength development through the various processes in a submarine landslide based on shear strength at given displacement.

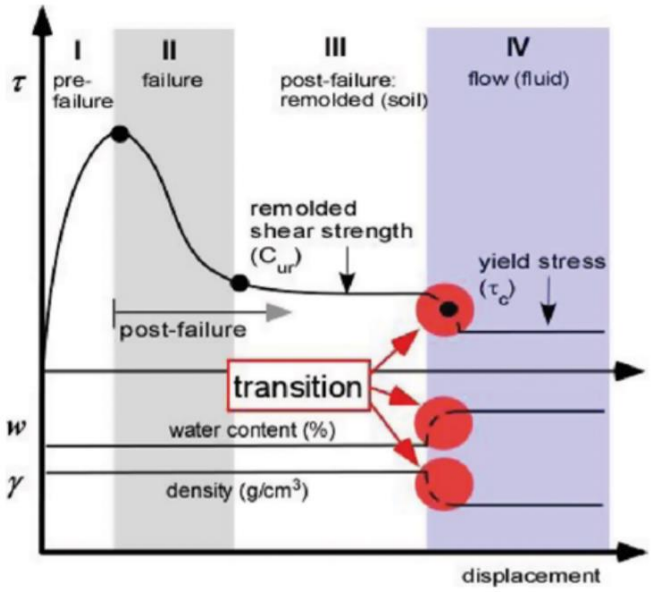

Figure 2. 2: Schematic illustration of the strength development with displacement (Jeong et al., 2015)

The transition between failure and post failure can be understood as a process involving state changes. The firm and structured material from slide initiation transforms into a remolded phase exposing the material towards water intrusion. Eventually, when enough water is mixed into to the diluted mass, a change in material properties occur. The strength evolution between remolded shear strength (C_{ur} in stage III) and yield stress (τ_c in stage IV) marks this transformation. This transition is based on the interaction between sediments and water as illustrated by the arrows in Figure 2. 2. The geo-mechanical properties changes due to the increased water infiltration during remolding (Jeong et al., 2015). Regulated by the strain softening and geo-mechanical properties, the general soil approaches a flow behavior drastically affected by the degradation of the soil structure caused by the increased water infiltration. This results in subsequently reducing the cohesion and shear strength.

2.4 Rheology

Rheology is *the theory of deformation and flow of matter* (Irgens, 2014). Based on the constitutive theory of highly viscous matter exhibiting viscoelastic and viscoplastic properties, rheology distinguishes matter into solids and fluids. Ideal solids will deform elastically, while ideal fluids

deform plastic by flow (Schramm, 1994). This constitutes two types of behavior: solids which will have a reversible behavior and fluids which will exhibit an irreversible behavior. Jeong et al. (2010) postulated that fine grained soils will behave as a debris which exhibits a rheological behavior like viscoplastic fluid, placing it between the ideal solid and fluid state.

2.5 Viscosity and non-Newtonian Fluids

Viscosity is the measure of a fluid's resistance to flow, representing a measure of the internal friction of moving fluids (Irgens, 2014). Fluids with high internal friction, meaning a high resistance to motion, can be classified as high viscous fluids, while fluids with high mobility and a lower internal friction can be classified as low viscous fluids. The properties associated to viscosity are highly dependent on many factors and often dependent on the material properties. Soft clays found *in situ* and fine slurries exhibits non-Newtonian flow behavior (Boukpeti et al., 2012). These are strain-rate and time dependent materials, which can be described by the relation between shear stress and shear strain rate. Eq 2.1 describes this constitutive relationship.

$$\tau = \eta(\dot{\gamma}) \cdot \dot{\gamma} \quad (Pa) \tag{2.1}$$

$\eta(\dot{\gamma})$ is the viscosity function in Pa·s, τ represents the shear stress (Pa) and $\dot{\gamma}$ the shear strain rate (S^{-1}). Viscosity is also a highly temperature and pressure dependent, which in total can be expressed through 6 parameters:

$$\eta = f(S, T, p, \dot{\gamma}, t\ E) \tag{2.2}$$

where S is physical-chemical dependence on viscosity, T is temperature dependency, p is pressure, $\dot{\gamma}$ is shear rate, t is times and E is electrical field.

To describe the characteristics of viscosity, a cylinder viscometer is commonly used (Irgens, 2014) an apparatus further described in chapter 3.5. Figure 2. 3 illustrates a fluid element subjected to normal stresses and shear stresses by a rotating cylinder. This element will deform according to Figure 2. 4, where the change in form can be expressed by the shear strain with the differential equation:

$$d\gamma = \dot{\gamma} dt = \frac{dv_x dt}{dy} \quad (-) \tag{2.3}$$

the strain rate between two parallel plates can further be quantified by:

$$\dot{\gamma} = \frac{dv_x}{dy} \quad (s^{-1}) \tag{2.4}$$

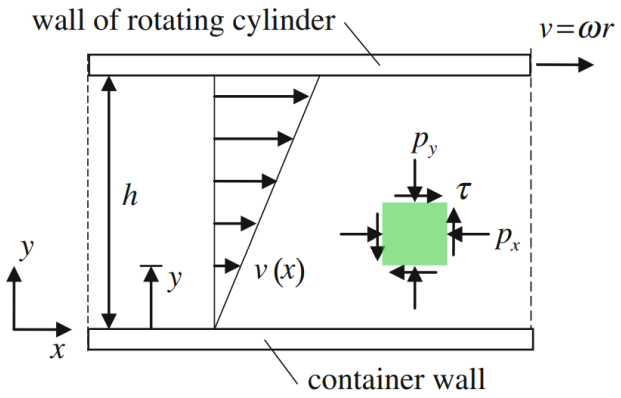

Figure 2. 3: Simple shear flow (Irgens, 2014)

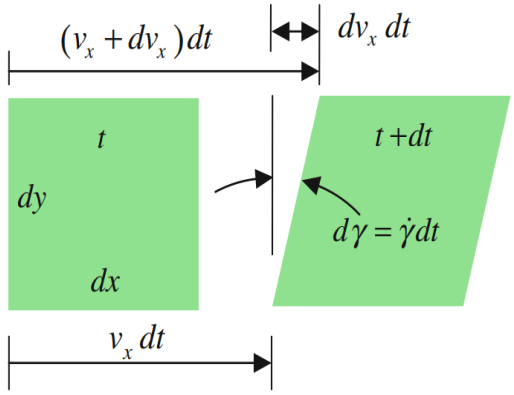

Figure 2. 4: Fluid element from Figure 2. 3 (Irgens, 2014)

The resulting shear strain rate and shear stress forms *flow curves*. These are together with viscosity curves describing the fluid behavior. Viscosity curves are formed by the shear stress, τ, viscosity, η, and the strain rate. Viscosity curves are described by the viscosity function and can be expressed as:

$$\eta(\dot{\gamma}) = \frac{\tau}{\dot{\gamma}} \tag{2.5}$$

The flow behavior can be classified into *Newtonian fluids* and *non-Newtonian fluids. Newtonian fluids* are defined as ideal liquids exhibiting a linear behavior between shear strain rate and shear stress. The viscosity is therefore unaffected by changes in the shear rate, resulting in a flat viscosity curve as illustrated by curve 1 in Figure 2. 5.

Non-Newtonian fluids can be defined as all other liquids not exhibiting the ideal flow behavior. By inflicting varying behavior, these fluids can be categorized as pseudoplastic, plastic fluids and fluids with dilatant flow based on the behavior.

- Shear thinning fluids can be described by plastic or pseudoplastic liquids (curve 2 and 4 in Figure 2. 5). Representing fluids which becomes thinner as the shear rate increases, these processes constitute mostly a reversible effect with some time lag. By terminating the shearing, the molecules obtain their natural state establishing a thixotropic hardening effect for most fluids. Thixotropic fluids can be identified by its potential to regain its structure at zero shear (Schramm, 1994).
- Liquids displaying dilatant behavior (curve 3 in Figure 2. 5) can be identified by increasing viscosity for higher shear rate, also called shear thickening fluids. Densely packed suspensions with a high void ratio are often characterized by dilatant behavior. These suspensions will at rest or low shear rates force particles with various size closer to each other, relocating the particles and reducing the voids. Higher shear rates will induce wedging causing a volume expansion or plastic deformation, which increases the necessary energy to maintain certain shear rate.

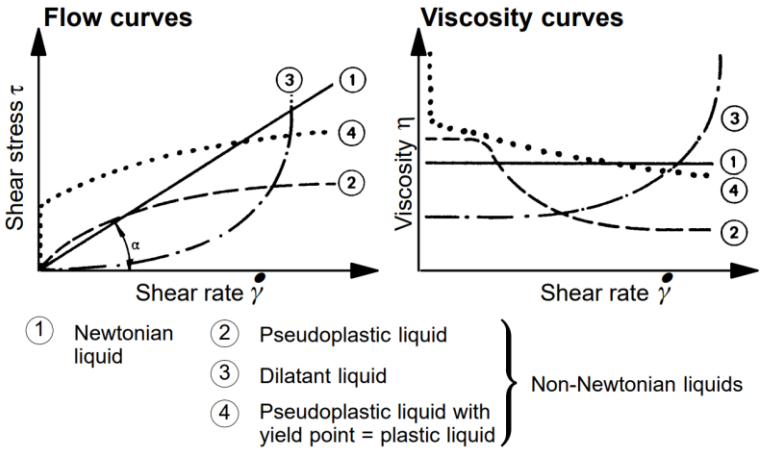

Figure 2. 5: Newtonian and non-Newtonian flow behavior (Schramm, 1994)

The viscosity of fine grained soils varies with the shear rate. By displaying both *shear thickening* and *shear thinning* behavior, fine grained soils exhibit a non-Newtonian behavior. This type of behavior is commonly described through a *power law*:

$$\eta(\dot{\gamma}) = K|\dot{\gamma}|^{n-1} \tag{2.6}$$

where K is the consistency parameter in Pa· s^n and a dimensionless exponent n representing the power law index. For $n > 1$, the material exhibits dilatant behavior and for $n < 1$ the material exhibits pseudoplastic behavior. At $n = 1$, the power law reduces to a linear function and the material can be identified as a Newtonian fluid.

2.5.1 Rheological Behavior of Fine-grained Sediments

Rheological behavior and properties of fine-grained soils represents an important topic of understanding and predicting slides. Fine grained soils can in in situ conditions be identified as yield stress fluids exhibiting viscoplastic behavior. Such viscoplastic fluids can rebuild a network of inter-molecular binding forces, also called thixotropic materials, after being remolded. The yield stress represents the threshold shear stress required to make a fluid flow. This is defined by the necessary shear force to break the intermolecular bonds which identifies the transition between elastic and plastic deformation.

Depending on water intrusion, material composition and behavior, two types of debris flow dynamics can take place: granular flow and viscous flow. Granular flow is based on the mechanics of granular media describing the physics of grain-grain and grain-fluid interactions. Viscous flow is, on the other hand, based on the assumption of a continuum material behavior with an inherent plastic viscosity, describing viscoplastic fluids containing fine material with a high water content. These different flow mechanism represents a large difference in flow mechanism where the rheological transition is not well defined (Jeong et al. 2010)

Bingham and Herschel-Bulkley are two models for modelling the flow behavior of fine-grained flows. Such rheological models are required to describe debris flow components and yield stress similar to actual field conditions. The simplicity of the models varies, and the use depends on area of interest. In this case the Herschel-Bulkley can be considered as a generalizations of the Bingham model.

Major & Pierson (1992) reported that small changes in the clay fraction, silt and sand proportion will modify the flow behavior, where high amounts of clay and sand tends to exhibit a Bingham-like behavior. Similarly Jeong et al. (2015) pointed out that Bingham and Herschel-Bulkley fluids could be applied for materials with high water contents.

2.5.2 Bingham Model

The Bingham model is considered as one of the simplest theoretical models to describe viscoplastic behavior. The shear stress, τ, and shear strain rate, $\dot{\gamma}$, describes a linear function, based on a pre-determined yield stress, τ_y, and critical shear rate, $\dot{\gamma_c}$. This demands shear stresses higher than the yield stress, meaning that flow will occur, for the model to be applicable. This is described in Figure 2. 6, and expressed by following equation:

$$\tau = \tau_y + \eta\dot{\gamma} \quad \text{for } |\tau| > \tau_y, \text{ and 0 otherwise} \tag{2.7}$$

where τ is shear stress in Pa, τ_y is yield stress in Pa, η is the plastic viscosity and $\dot{\gamma}$ is the shear strain rate in s^{-1}.

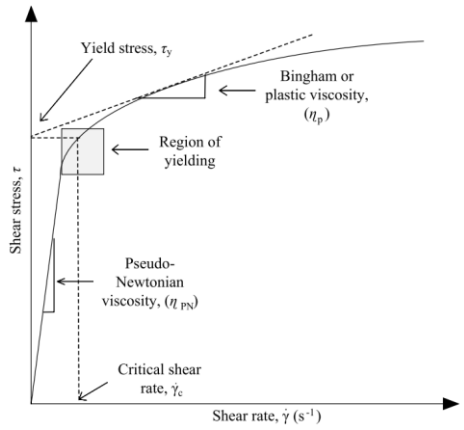

Figure 2. 6: Schematic illustration the Bingham model at steady state rheology. Dashed straight line represents Bingham fluid with yield stress and viscosity. Solid line represents the flow curve obtained from fine grained sediments (Jeong et al., 2010).

Jeong (2013) represents the flow behavior of viscous fluid with three flow regimes. Regime 1 identifies a creep regime characterized with high viscosity ($\tau < \tau_y$) representing a pseudo-Newtonian behavior. Regime 2 identifies a transitional region in where the yield stress is approached ($\tau = \tau_y$), illustrated as region of yielding (Figure 2. 6). Regime 3 identifies a state of flow where the shear stress exceeds the yield stress ($\tau > \tau_y$), commonly known as *Bingham fluid*.

The Bingham model presents the flow behavior as a linear function based on the yield stress at critical shear rate. Hence, a full representation off the rheological behavior is impossible. This model overestimates the shear stress at flow regime 1 (lower shear strain rates), Jeong et al. (2010) found this to be for rates below $20s^{-1}$. For higher shear rates, many fluids tend to approximate Bingham fluids, making the ideal Bingham model convenient.

2.5.3 Herschel-Bulkley Model

The Herschel-Bulkley model describes fluid behavior based on 3 parameters capturing all flow regimes. It assumes a nonlinear response controlled by the change in viscosity relative to the shear strain rate. The model is expressed by the following equation:

$$\tau = \tau_y + K\dot{\gamma}^n \quad for\ |\tau| > \tau_y, \text{ and 0 otherwise} \tag{2.8}$$

where τ_y is the yield stress in Pa, K is the consistency parameter in Pa$\cdot s^n$ and n is the Herschel-Bulkley exponent $(-)$, commonly known as the curvature exponent. However, as illustrated in Figure 2. 7, the yield stress τ varies depending on the model implying that τ for Bingham is different from τ in the Herschel Bulkley.

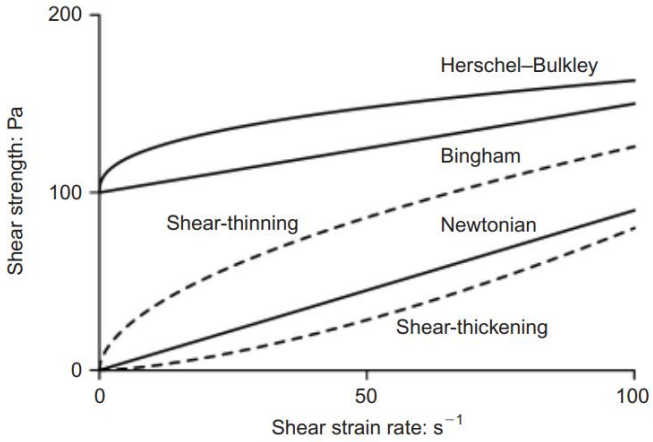

Figure 2. 7: Viscous strength for various fluid models (Boukpeti et al., 2012)

It is worth mentioning that literature highlights flow curves from viscometric tests of fine sediments as better fitted by Herschel-Bulkley model than by ideal Bingham model(Coussot & Piau, 1994; Jeong et al., 2012). Using three parameter, the model is proposed to fit the whole flow curve through all three regimes. This will according to Boukpeti et al. (2012) be sufficient to represent the behavior kaolin suspension.

2.6 Factors Affecting Clay Rheology

Mineralogy, grain size, soil structure and salinity are elements that heavily influence the viscous characteristics. Changes in these properties entails changes in the soil rheology influencing the viscous behavior. Fine grained slurries can be characterized as colloidal system where the soil

minerals are dispersed in the liquid. Highly liquid slurries are sensitive towards particle-to-particle interactions and forces between such colloidal systems. Fine grained material, especially clay, have a high surface to mass ratio allowing the effect of van der Waals forces. Clay particles carries further a net negative charge, when in contact with water, this magnifies the interparticle forces. This extent of influencing factors makes understanding clay rheology a complex process dependent on chemical and physical attributes.

For describing how particle interactions affects rheological characteristics in fine grained soils, an understanding of soil behavior and particle repulsion/attractions forces is necessary. The following sections are devoted to describing particle charge mechanism and material parameters that affects clay slurry rheology.

2.6.1 Pore Water Chemistry and Electrical Double Layer

Clays are surface-active materials with properties that are heavily influenced on the activity of surface phenomena (Mojid, 2011).The ion exchange of positive ions and ions with lower valency makes the particle surface negatively charged. For clays with high water content, this process will form a zone around each clay particle, commonly called the *diffuse double layer*. The size of this double layer is highly dependent on the ionic concentrations, in which a high concentration will generate a small double layer and low concentrations will generate a large double layer, as shown in Figure 2. 8.

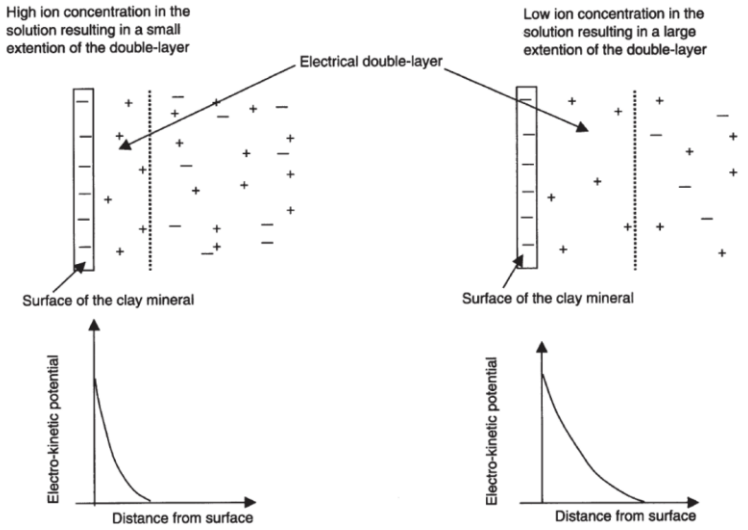

Figure 2. 8: Schematic illustration of the relationship between ionic concentration and the diffuse double layer (Ranekka et al., 2004).

Flocculation can be described through the flocculation value. This value defines the concentration of ions at which flocculation occurs, and is dependent on two factors: the flocculated clay mineral, and the ion causing flocculation. The effects of cations flocculation power can be described through the Hofmeister series (Lozano & Sánchez-Silva, 2019):

$$H^+ > Ba2^+ > Sr^{2+} > Ca^{2+} > K^+ > Na^+ \quad (2.9)$$

The Hofmeister series presents hydrogen ions as strongly adsorbed, making the particle-to-particle interactions highly influenced by pH. High ion concentrations cause a small double layer making the negative load of the clay particles neutralized from the excess positive ions. This forces the clay particles closer to each other, which makes the particle association dominated by van der Waals forces resulting in increased flocculation (Luckham & Rossi, 1999).

Clay particles will typically orient themselves towards following modes: Dispersed (a), Face to Face (FF) (b), Edge to Face (EF) (c), Edge to Edge (EE) (d), as illustrated in Figure 2. 9. Such modes are governed by the interactions of the double layers between clay particles.

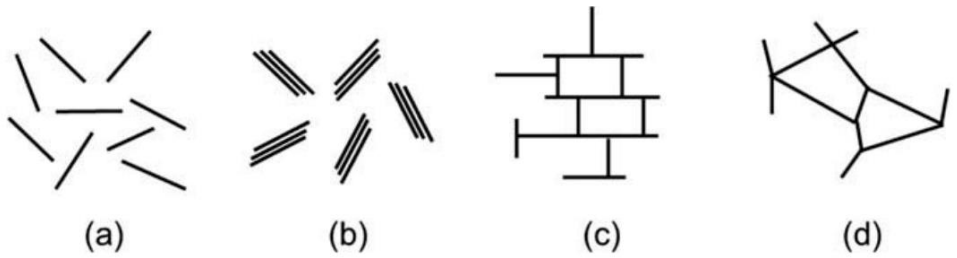

Figure 2. 9: Mode of particle association (a) Dispersed, (b) Face-to-Face, (c) Edge to Face, (d) Edge to Edge (Luckham & Rossi, 1999)

The amount of immobilized free water a clay suspension can hold is defined by the established structure. Flocculated structures containing EE or EF particle associations holds large voids making room for large amounts of pore water. The EF structure is a result of when the ionic conditions in the water favors charged particles having positive edges and negative basal surfaces, which is typically forming a "card house structure". This edge to face particle structure is typical for marine clays. The FF association on the other side creates an effectively thicker particle with smaller voids resulting in a lower capability of holding pore water.

Kaolin is a heterogeneously charged platelet-like particle exhibiting a high aspect ratio (face-edge ratio). This combination of geometry and charged surface complicates the relation between particle chemistry and rheology of kaolin. The relation between the silica-like faces and silica-alumnia-like edges governs the particle surface behavior, as illustrated in Figure 2. 10. The silica-like faces exhibit a negative charge while the silica-alumnia edges exhibits an alternating behavior affected by the pH depending alumina. The silica-alumina edges are considered positively charged for pH below 7, and negative for pH over. Hence, a highly pH dependent colloidal network will be formed based on the charge of the edge surface. The flocculated structure ranges from face-edge attraction repulsion and face-face attraction. pH 1-3 will exhibit high concentrations of electrolytes contributing to a thick double layer. The attraction will, as a result, lead to negatively charged surfaces resulting in a FF structure. For pH between 3-7, the pH dependent silica-alumina edge will progress towards an isoelectric stage (the point where the net charge of a particle becomes

zero). This induces a positively charged edge that is attracted to the negatively charged face, governing a house of cards structure. For pH over 7, repulsion between homogenously charged particles governs the colloidal structure (Perrot et al., 2016).

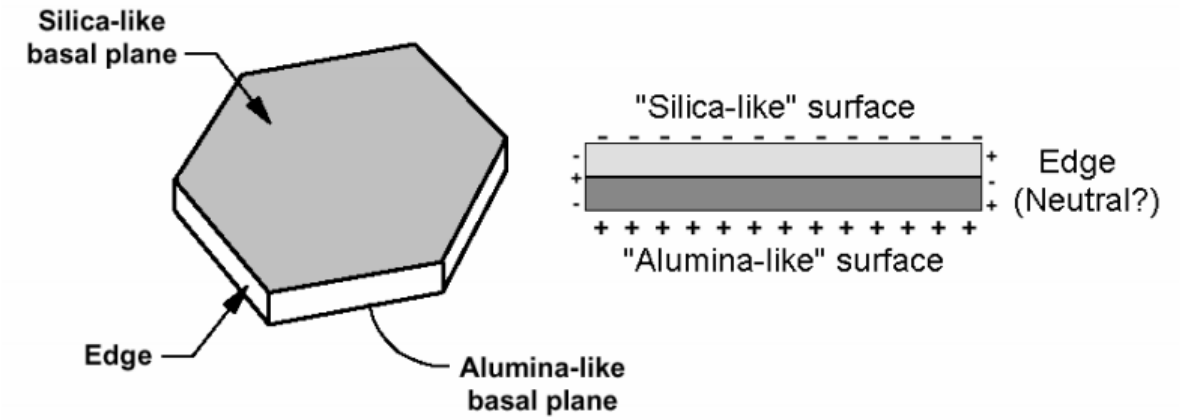

Figure 2. 10: Carty idealization of the kaolin particle charge distribution (Carty, 2001)

2.6.2 Water Content and Atterberg Limits

Fine grained soil can be categorized into one of following states depending on water content; dry/hard, crumbling/firm, plastic or liquid. The water content is defined by the ratio of mass water to mass dry solids in a material.

$$w = \frac{m_w}{m_s} = \frac{m - m_s}{m_s} \tag{2.10}$$

where m_s is the mass of dry solids, m_w is the mass of water and m is the mass of sample.

The Atterberg limits describes the behavior of fine grained soils through 3 semi-empirical indices. These indices are described below and illustrated in Figure 2. 11, and can be classified into plastic limit, liquid limit and plasticity index (Fitton & Seddon, 2012):

- The shrinkage limit (w_s) describes the limit where loss in moisture content no longer will reduce volume.
- Plastic limit (PL, w_p): represents the moisture content where the soil changes its behavior from brittle solids to plastic solids.
- Liquid limit (LL,w_L): represents the moisture content at which the soil material changes its behavior from plastic to liquid.
- Plasticity Index (PI, I_p): represents the plasticity of the soil material. This magnitude is defined by the difference in moisture content between LL and PL, represented in equation in the following equation:

$$I_p = w_L - w_P \tag{2.11}$$

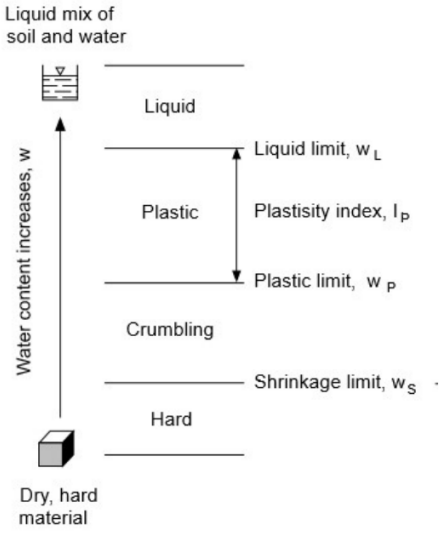

Figure 2. 11: Schematic illustration of propterties behind Atterberg Limits (NTNU, 2015)

Clays are commonly classified by plasticity, where PI <10 indicates low plasticity, PI between 10 and 20 indicates medium plastic clay and above indicates high plasticity (NTNU, 2015).

The liquidity index, (LI(−)) relates the natural water content to the Atterberg limits. By connecting these parameters, the material behavior can be described through both plasticity and water content further describing the relationship between material and rheological properties. This normalization can be expressed as:

$$LI = \frac{w - w_p}{w_L - w_P} = \frac{w - w_p}{I_P} \tag{2.12}$$

Correlation between viscosity and yield stress of fine-grained sediments due to volumetric concentration of solids can according to Jeong (2013) show a relationship between rheological parameters (plastic velocity and Bingham stress) and liquidity index. This relationship turns out to be strong for clay-rich materials compared to silty materials. Such a correlation between rheological parameters and liquidity index is applicable for both Bingham viscosity and pseudo-Newtonian viscosity, making index properties significant in linking geotechnical properties to rheological flow behavior of fine-grained sediments.

2.6.3 Grain Size

Soil minerals and grains found in marine clays are formed through weathering and deterioration (Masson et al., 2006). These chemical and physical processes influence the grain form, grain size, and general properties of the material. Clay particles represents all particles smaller than $2\mu m$ (0.002 mm), and a soil is defined as clay when 30% or more of the soil content is smaller than 2

μm (Statens vegvesen, 2018). The clay content (CF) can be expressed through the relative grain weight of the clay fraction:

$$CF = \frac{m_c}{m_s} \tag{2.13}$$

Where m_c is the mass of clay grains, and m_s is the total mass of soil sample.

2.6.4 Clay Activity

Clay activity was by Skempton (1953) introduced as a measurement of the plasticity index (PI) to the clay fraction (CF) ratio. This parameter distinguishes the mineralogic differences in fine-grained soils by describing the ability of clays to bind water molecules to the grain structure. Sensitive clays in Norway are typical dominated by illite-rich clays, a stable mineral which produces inactive materials when subjected to leaching (Bjerrum, 1954). Kaolin is commonly characterized as the clay having the lowest activity, contributing for a predictable behavior when used as a model clay. The clay activity can be expressed as:

$$A_c = \frac{I_p}{CF} \tag{2.14}$$

where inactive clays are defined by an activity below 0.75. Jeong (2013) discovered that viscous behavior of fine-grained sediments is related to level of clay activity. Figure 2. 12 illustrates his findings, where low to medium active clays (illustrated as the black line) will behave according to a Herschel Bulkley model, while high activity clays and silty clays exhibits a shear thickening behavior (presented in the red dotted line). Note that these experiments are conducted on soils hydrated with fresh water.

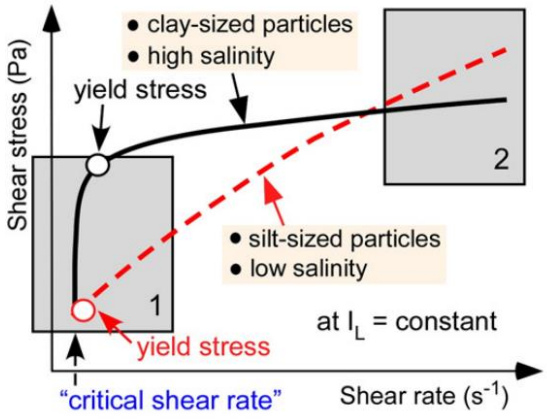

Figure 2. 12: Flow behavior as function of clay activity and grain size (Jeong, 2013)

2.7 Strength Measurement and Strain Rate Effects

Strength properties of soft seabed soils can be considered a crucial part of understanding the geohazards in a fjord and relating soil behavior. This section will introduce the various strength measurement methods used to characterize the BF clay and kaolin clay. Figure 2. 13 gives an indication of the possible strain rates for the conducted test. Method of implementation and procedures will be described in chapter 3.

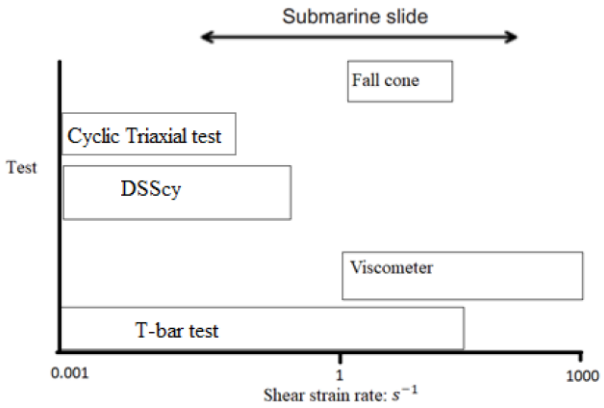

Figure 2. 13: Typical strain rates for strength measurements, inspired by (Boukpeti et al., 2012)

Measuring strength properties and relating soil behavior can be done through numerous methods and devices. Boukpeti et al. (2012) divides these methods into two categories: intrusive tests, and element tests. Intrusive tests describe tests which measures "in situ" strengths commonly carried out in the field, such as CPTU, penetrometer, torevane or fall cone tests. Element tests represents laboratory tests with high accuracy and quality such as triaxial, DSScy and oedometer tests. In this study, viscometer, fall cone, T-bar, cyclic triaxial and DSScy tests were conducted. Strain rates and the effects of strain rates will be presented in the discussion.

The strength-deformation behavior of soil structure interfaces plays an important role in predicting and understanding the behavior of submarine landslides and impact forces. Martinez & Stutz (2018) names three important factors controlling the shear behavior of fine-grained soil-structure interfaces: surface roughness, stress history and shear rate. The viscosity and shear effects from soil to soil interface has been highlighted by several authors (Boukpeti & White, 2016; Quinn & Brown, 2011) as having a significant impact on the strength behavior. Jung & Biscontin (2006) suggests that there is a unique relation between the shear stress at corresponding shear strain. This suggests that there is a pre-determined path for given stress strain curve. This is also, according to Graham et al. (1983), independent from loading history, since stress-strain relations goes back to a unique trace for given rate as the rate is changed during testing.

For soft clays, the cyclic resistance will normally decrease from the initial static shear stress. The total response will however increase in total shear strength, due to effects from the static and cyclic shear stress (Lefebvre & Pfendler, 1996). Strain rate dependency can be investigated through

drained and undrained conditions. Figure 2. 14 illustrates an idealized strain rate effect curve, identifying regions of different soil behavior. In fully drained phases, the shear-velocity is slow enough for water to dissipate. This changes for higher shear rate where less water dissipates, until no water dissipates and undrained conditions is reached. Typically, rate effects have been investigated on drained conditions, simulating clay behavior through various phases. For this study, the cyclic shear stress was applied for undrained conditions, demanding no volume change, in order to dissociate the effect of the cyclic shear stress from the effect of water dissipation that takes place during the application of a drained shear stress.

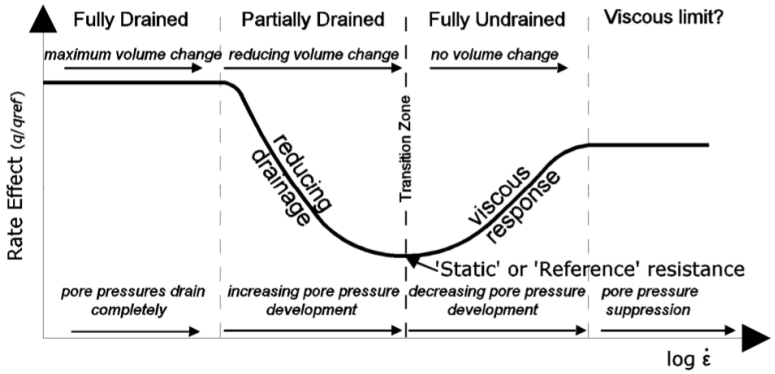

Figure 2. 14: Schematic illustration of an idealized strain rate effect curve, identifying regions of different soil behaviour. (Quinn & Brown, 2011)

2.8 Flow Behavior and Impact Forces of Fine-grained Debris Flows

Submarine debris flows can, as mentioned in 2.5.2, be described as Bingham fluids. Elverhøi et al. (2000) describes the simple shear situation in laminar flow, as a stress-strain relation for a viscoplastic Bingham fluid where no deformation takes place until a specified yield stress is applied. This is, as Jeong (2013) describes, representing the third phase, after which deformation is driven by excess stresses beyond the yield stress. The flow behavior of a debris flow is therefore heavily dependent on the viscoplastic relations in the material. Although the importance of material properties shouldn't be overlooked, literature (Blasio et al., 2006; Ilstad et al., 2004; Locat & Lee, 2005) highlights the relation between debris flow mobility and hydroplaning as crucial.

2.8.1 Hydroplaning

Hydroplaning represents a basal layer of water which can markedly reduce the friction between the seabed and debris flow. This phenomenon is considered the most prominent explanations for the high velocities and long travel distances of many submarine flows (Blasio et al., 2006). In some cases, the effect of hydroplaning causes the slide head to drift out ahead of the body, leading the physical effect of hydroplaning and flow properties to override the rheologic features of the

material. This in turn leads to a geometry change of the deposit different to what is associated with the yield strength of the debris flow.

For hydroplaning to take place, two criteria have to be fulfilled: the slide material cannot dissolve into a suspension, simultaneously as the mass is mobile enough to reach the critical velocity for the onset of hydroplaning (Elverhøi et al., 2000). If these conditions are fulfilled, a hydrodynamic stagnation pressure in front of the slide will be established. When this pressure equals the body mass (submerged weight per unit area of the flowing mass) the ambient fluid will start to flow beneath slide masses, establishing a lubricating layer between the seabed and debris flow head. This evidence of hydroplaning will cause the head to be lifted and potentially deform flow into a bulbous shape.

Following Bernoulli's principle, a body moving in an ideal non-viscous fluid, the relative velocity at the front and end point is zero. This point will acquire a higher-pressure, so-called stagnation pressure, compared to the rest of the body. This pressure can be described by:

$$P_f = \frac{1}{2}\rho_w U^2 \tag{2.15}$$

where ρ_w is the density of water, U is the debris flow velocity. For a fully developed hydroplaning, the lubrication layer supports the average load per unit area from the slide block. This pressure form is by Blasio et al. (2006) defined as $\Delta\rho g H cos\beta$ which describes the density difference between sediments and water, acceleration of gravity, block height and slope angle. A full stress situation of a slide block is illustrated in Figure 2. 15.

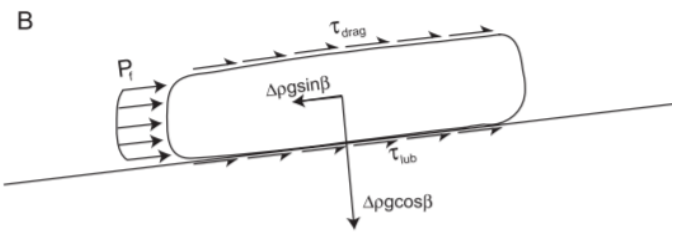

Figure 2. 15: Schematic illustration of stresses and forces acting on a slide block (Ilstad et al., 2004)

These properties combined with velocity defines the Froude number, Fr, indicating the influence of gravity on fluid motion. This way of representing Fr is recognized by several authors (Elverhøi et al., 2000; Ilstad et al., 2004; Mohrig et al., 1998) in the scaling of the dynamic pressure on a moving body.

$$Fr = \frac{U}{\sqrt{\left(\frac{\rho_d}{\rho_w} - 1\right) \cdot gHcos\beta}} \tag{2.16}$$

Mohrig et al. (1998) reported a Fr between 0.3 and 0.4 will trigger the onset of hydroplaning. However once effects of hydroplaning is established, values in the range of 0.8-1.4 are typically found (Ilstad et al., 2004).

2.8.2 Impact Force of Debris Flow

When assessing geohazards and damage resulting debris flow events, considering the effect of impact forces on structures is key (Ashenafi, 2020). Impact forces are a result of the geometry, material properties and velocity contributing and affecting the slide circumstances. Several studies have been conducted on the effects of impact forces on offshore structures where especially offshore pipelines related to oil and gas projects have been carefully investigated (Georgiadis, 1991; Liu et al., 2015; Randolph & White, 2012; Sahdi et al., 2019; Zakeri et al., 2008, 2009). The impact force can be decomposed into three orthogonal components: drag force normal to the axis in prevailing force direction, longitudinal drag force parallel to the axis, and vertical force (lifting or pushing down the object). The first component (normal to the axis) is normally considered the principal damaging factor for seafloor installations, while longitudinal and vertical forces are highly dependent on the geometry of structure.

Zakeri et al. (2008) identifies two perspectives for investigating the drag forces on offshore structures: a geotechnical approach and a fluid dynamical approach. The geotechnical approach relates to the undrained shear strength, s_u, and a parameter, k, relating to the s_u to the drag force.

$$F_D = k \cdot s_u \cdot A \tag{2.17}$$

where A is described by the projected front area and F_D represents the drag force in the prevailing flow directions perpendicular to the cylindrical pile or pipeline. The values k can be defined, either by a constant value, also known as the conventional approach, or as a power law function taking the strain rate effects into consideration.

By taking a fluid dynamic approach, the analyze of flume data and flow behavior is adopted. The characteristics of a fluid flow around a certain object with a given shape is greatly influenced by the object geometry and size, relative velocity between object and fluid, and fluid properties. The drag force will act as a product of a drag coefficient, C_D. C_D is further based on both Froude and Reynolds number, Re, which can be considered the most important dimensionless parameters for studying incompressible flow on an object (Zakeri et al., 2008). However, for many flows the effects of gravitational waves around a body or an airfoil can be considered negligible. For such cases the Froude number becomes irrelevant, and the drag coefficient becomes a function of only the Reynolds number (Kundu, 2004). The classical way of describing the Reynolds number for a Newtonian fluid is as follows:

$$Re_{newtonian} = \frac{\rho U_\infty D}{\mu} \tag{2.18}$$

here μ represents the dynamic viscosity, D is the characteristic length scale – the diameter of cylinder in this case, ρ is the fluid density and U_∞ is the approaching debris head velocity. However, this formulation is not directly applicable to the problem of a non-Newtonian material. Zakeri et al. (2008) proposes an ad hoc Reynolds number related to shear thinning, non-Newtonian fluids which can be described by either a power law or Herschel-Bulkley rheological model. This formulation is based on the apparent viscosity and defined as the relationship between shear rate

effects and apparent viscosity on non-Newtonian fluids. The suggested shear rate is then formulated as:

$$\dot{\gamma} = f \cdot \frac{U_\infty}{D} \tag{2.19}$$

where f represents and adjustment factor based on the flow around mechanism of the soil

The apparent viscosity μ_{app} can be presented as a Herschel-Bulkley fluid by dividing the shear stress for given shear rate:

$$\tau = \tau_y + K\dot{\gamma}^n \rightarrow \mu_{app} = \frac{\tau_y}{\dot{\gamma}} + K\dot{\gamma}^n \tag{2.20}$$

The Bingham model can be considered as a special case of the Herschel Bulkley model, where the plastic velocity, η, equals the unity and the consistency parameter, K, is identical to the Bingham viscosity.

By introducing the apparent viscosity into Herschel Bulkley formulation, we obtain an alternative formulation of the Reynolds number based on eq. 2.19 and 2.20:

$$Re_{non-Newtonian} = \frac{\rho U_\infty^2}{\mu_{app}\dot{\gamma}} = \frac{\rho U_\infty^2}{\tau} \tag{2.21}$$

where τ represents the fluid shear stress at given strain rate from Eq.2.19. The drag coefficient, C_D, can then be described based on the total drag force, F_D, influenced by Pazwash & Robertson (1975) dynamic interpretation of impact forces from debris flows:

$$F_D = \frac{1}{2}\,\rho \cdot C_D U_\infty^2 A \rightarrow C_D = \frac{F_D}{\frac{1}{2}\,\rho U_\infty^2 A} \tag{2.22}$$

The Reynolds number for non-Newtonian fluid is defined as a function of three parameter: shear stress (at given shear rate), fluid density and debris head velocity. Being directly proportional to the density and velocity squared, and inversely proportional to the shear stress, shows that the uncertainty in velocity has a much more pronounced impact compared to uncertainties in density and shear stress for the computed Reynolds number.

3. Laboratory Experiments

To better understand soil behavior for soft soils related to submarine landslides, debris flows, and mudflows, rheological models and instruments have become more common in geotechnical evaluations. The interaction between grains and water plays an important role in the strengths of soils. Terzhagi postulated in 1925 that the interactions between soil particles constituted the effective stress of a soil. This meant that the effective stress was defined by deducting the pore pressure from the total stress, $\sigma_e = \sigma - u$.

The soil behavior regarding solids/liquid relationship is determined by the soil properties, such as Atterberg limits. Test procedures for geotechnical equipment's are mostly designed with bearing capacity and slope stability in mind. Hence, the design of geotechnical tests methods are generally based on classifying material properties based on a pre-determined soil strength. However, some geotechnical devices are capable of evaluating soil characteristics at very low strengths or fluid states, such as vane, fall cone and T-bar tests. These tests have an increasing margin of error for very soft soils. Subsequently, soil that exhibits fluid characteristics, such as slurries or debris flows, may not be properly characterized by geotechnical testing methods. On the other side, rheometry tests such as viscometer tests, are developed to characterize mechanical behavior of fluids with good precision. These are therefore very sensitive test methods which often makes soil materials in high stages of consolidation or drying very hard or even impossible to measure. The limits to determine material characteristics for the range in between the use of a viscometer, representing fluid behavior, and more usual tools in geotechnics, representing a firmer state, is not established. As a consequence, material consistency, device limitations and application purposes must be taken into consideration.

3.1 Introduction

This chapter gives a description of the laboratory experiments preformed to map soil properties, strain rate dependency and general behavior to both BF and kaolin clay. A list of preformed tests to each given sample is presented in chapter 3.3, followed by material properties found through the various tests, listed in table Table 3. 1. Due to lack of general procedures and guidelines on viscometer and T-bar tests, a detailed review of the chosen approach and procedures is introduced. Regarding interpreted material properties of the Bjørnafjorden clay, test results have been evaluated in consideration to data found in the NGI reports (NGI, 2019a, 2019b, 2019c). All laboratory tests except from DSScy tests were conducted in the geotechnical lab at NTNU. The DSScy tests were conducted at NGI-Oslo, using their routines and procedures. Supervision, guidance and necessary tools was provided from lab technicians at both NGI and NTNU.

3.2 Purpose

The purpose of the laboratory experiments is to study the Rheological properties and strain rate dependency when influenced by different water content for both BF and Kaolin clay. The objective is to map similarities and differences in material and rheological properties. A study, which is important for the interpretation of small sized model slide and its impact forces, which is used to define the framework conditions of a numerical model.

3.3 Performed Tests

The tests mentioned and performed in this study are a part of a larger test program. Performed tests were chosen based on measured property, accuracy of tests, reproducible results, and availability of device for measurement. All test samples are obtained from either mixed kaolin clay or cylinder samples extracted from relevant test site in Bjørnafjorden.

Following tests were carried out:

- Fall cone (w)
- Atterberg limits (w)
- Pycnometer
- Hydrometer
- Viscometer (w)
- T-bar (w)
- Cyclic triaxial (w)
- DSScy (w)

(w) marks tests where water content was conducted.

3.3.1 Materials

Two different types of clays were compared. Clay from Bjørnafjorden (BF clay), extracted from the seabed, was stored in 74mm cylinder for two years, and kaolin clay, which was ordered from *Alt for keramikk AS* and delivered in dry powder form. Both BF clay and kaolin clay (after mixed with water) were stored in a room at 95% relative humidity at 4 ° C.

Table 3. 1: Soil characteristics for tested clays

$Clay$	$Depth[m]$	S_{ur}[kPa]	S_t[kPa]	w[%]	w_L[%]	w_p[%]	I_p	$\rho_S[g/cm^3]$
$Bjørnafjorden$	$2.1-2.8$	4.2	2.93	90	101	35	66	2.74
$Kaolin$	$[-]$	$[-]$	$[-]$	93	59	31	28	2.73

3.3.2 Bjørnafjorden Clay Sample

The Bjørnafjorden test results are based on Bore Hole 12A (BH-12A), Bore Hole 11A(BH-11A) and Bore Hole 13A (BH-13A), illustrated in Figure 3. 1 (a). Cyclic triaxial tests were carried out on BH-12A and DSScy on BH-13A, while viscometer and fall cone tests were conducted on both BH-12A and BH-11A. For storage periods the residual soil was stored in a cooling room with plastic and aluminum foil wrapped around. In case of longer periods between testing, only parts of the cylinder were extracted.

3.3.3 Kaolin Clay

The kaolin clay used in the experiments is consists mainly of Silicon dioxide (SiO_2) and Aluminium oxide (Al_2O_3) and, as mentioned, delivered in dry powder form stored in bags. A mortar machine was used combined with vibrator to mix dry kaolin powder with water, illustrated in Figure 3. 2. To ensure a homogeneous composition, kaolin clay with water contents of $100\%, 125\%$ and 150% where made. Afterwards, the clay was stored in double sealed bags and stored. Figure 3. 1 (b) illustrates a pre-consolidated triaxial specimen of kaolin clay. The pre-consolidated procedure was only used for triaxial tests. Preparations of kaolin samples for DSScy was done at NGI and will be described in chapter 3.7.

(a) (b)

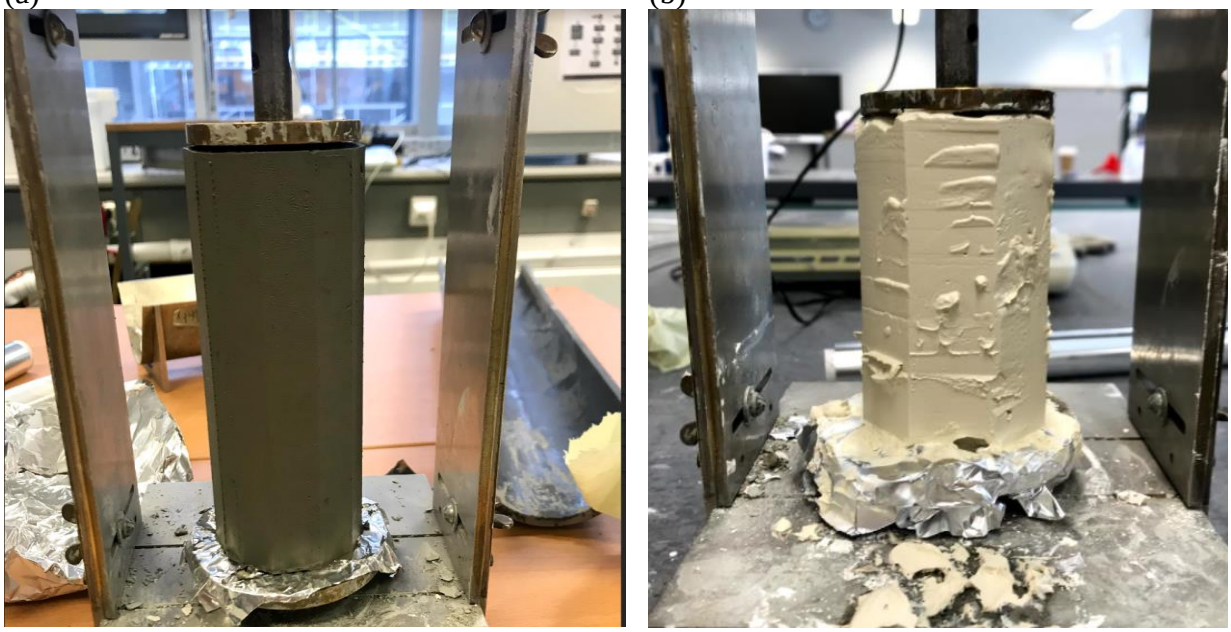

Figure 3. 1: (a) presents trimmed triaxial sample of BF clay sample (water content: 91%). (b) presents pre-consolidated trimmed triaxial specimen of kaolin clay sample (water content 62%).

Figure 3. 2: Mixing of kaolin and water using a mortar machine.

3.4 Index tests

3.4.1 Water Content

Water content conducted for current tests was done in accordance to *NS 8013 (*1982) and calculated by using Eq. 2.10.

3.4.2 Index Shear Strength – Fall Cone

The fall cone test was mainly developed to evaluate undrained shear strength, S_u, sensitivity, and liquid limit of fine-grained clays. A falling cone represents a bearing capacity situation. Assuming an undrained condition and rigid-plastic cohesive behavior of the soil based on the Tresca criterion, a relationship between penetration depth (caused by gravity and dead weight) and bearing capacity of the soil can be found. This relationship represents the correlation parameter *K*, described by Hansbo (1957) as:

$$S_{u,Fall\ cone} = \frac{KQ}{h^2} \tag{3.1}$$

where *Q* is the cone force and *h* is the penetrated depth. Correlation value, *K* = 0.27, and is according Boukpeti et al. (2012) found using a shear strain rate between 1-10 s^{-1}.

Undrained shear strength, remolded shear strength and sensitivity was determined according to *NS 8015* (1988) with fall cone tests. The fall cone test together with the T-bar test works as the best geotechnical method to examine the remolded shear strengths into the fluid phase, illustrated in Figure 3. 3 (a). The remolded shear strength found using fall cone is directly comparable to shear strengths found by viscometer and T-bar tests. It should be mentioned that the accuracy in this method drops significantly for low shear strengths. It is further assumed that the fall cone apparatuses were correctly calibrated for weight of the cone.

3.4.3 Atterberg Limits

Plastic limit (w_p) test was done according to (*NS-EN ISO 17892-12*, 2018) for both BF and kaolin clay. Two separate tests were performed and the average of these were used, illustrated in Figure 3. 3 (b). This test requires experience to assure correct results. The results documented in (NGI, 2019c) correlated well to conducted test results for BF clay.

Liquid limit (w_L) can be determined either with Casagrande method described in *NS 8001* (1982) or with fall cone, described in *NS-EN ISO 17892-12* (2018). For this study, the fall cone approach was chosen, illustrated in Figure 3. 3 (a).

Based on w_P and w_L, the plasticity index (I_P) and liquidity limit, LI, can be found through equation 2.11 and 2.12. For LI of kaolin clay, the in-situ water content is based on measured water content of sample.

(a) (b)

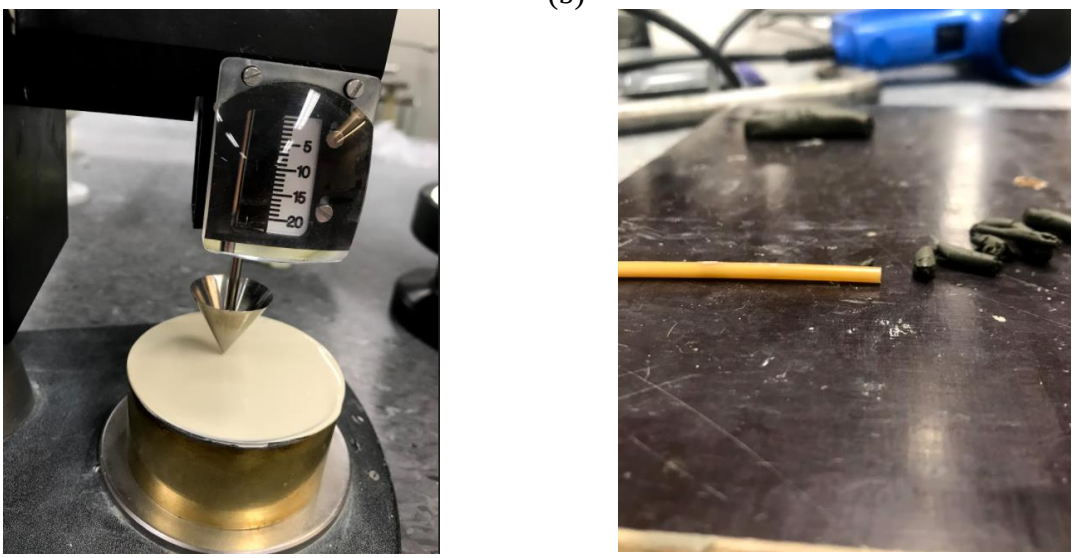

Figure 3. 3: (a) illustrates a fall cone experiment on remolded kaolin clay. (b) illustrates determination of plastic limit, w_P, on BF clay.

3.4.4 Grain Density

The average density of solid grains in kaolin clay was determined by using pycnometer. Grain density regarding Bjørnafjorden clay is found in (NGI, 2019c). The test with kaolin clay was conducted according to *NS-EN ISO 17892-4* (2016), with the water density already determined. To minimize error, two tests were carried out simultaneously. The results were checked with literature, and an average of the two tests were used.

3.4.5 Grain Size Distribution

The grain size distribution of kaolin clay was found through a hydrometer analysis. In case of Bjørnafjorden, the results were found in (NGI, 2019c). This method is based on Stoke's law for equivalent spheres sedimenting freely in a liquid or gas. A calibrated hydrometer was lowered into a suspension of water, sample, and a dispersive agent, which then measures the concentration at predetermined intervals. The test was carried out according to *NS-EN ISO 17892-4* (2016).

3.5 Viscosity and Couette Flow

Viscosity refers to a measure of fluid resistance to deformation at a given rate. To measure the viscosity and other rheological features, a coaxial cylinder viscometer was used on both kaolin and BF clay.

3.5.1 Coaxial Cylinder Viscometer

The coaxial cylinder viscometer, illustrated in Figure 3. 4 (a-b), is based on the Princip of couette flow, which means it measures the viscosity of a material in the space between two surfaces. One surface moving tangentially relative to the other, which imposes a shear stress on the material, which at a low viscosity induces flow.

(a) (b)

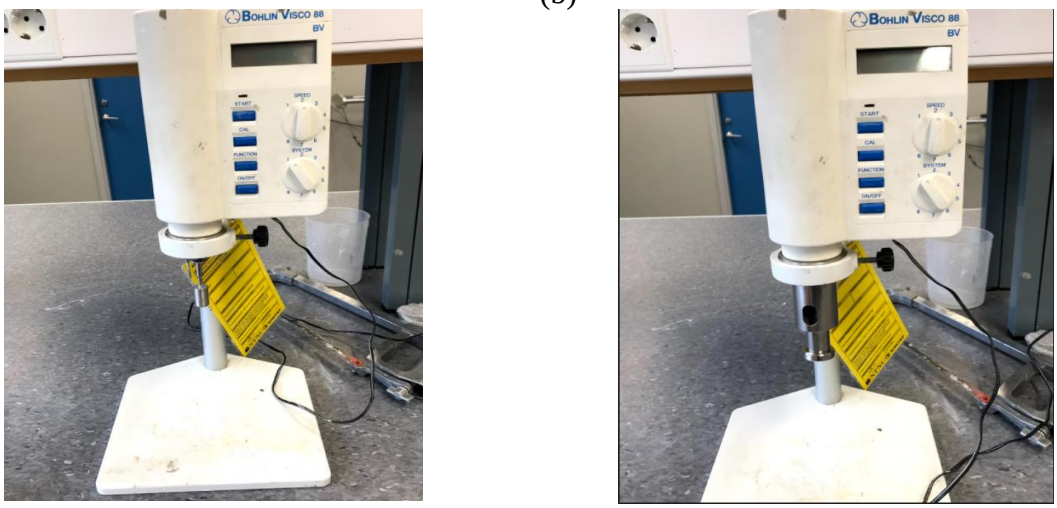

Figure 3. 4: Bohlin Visco 88BV viscometer instrument. (a) illustrates viscometer with rotor, (b) illustrates viscometer with rotor sealed by the outer cylinder.

3.5.2 Viscometer Apparatus and Design

The coaxial cylinder viscometer is a widely used and acknowledged device for measuring rheological properties of various materials (Major & Pierson, 1992). It consists of two coaxially cylinders, which a sample fluid is sheared. The outer cylinder, R_0, is stationery and acts as cup for the test fluid, while the inner cylinder, R_i, works as a rotor, applying an angular velocity, Ω, on the material. The cylinder rotation establishes a couette flow, which induces shear in the fluid sample. This generates a drag force on the inner cylinder, which in a rate-controlled test, forms a moment of the force (torque) (Wazer, 1963). This is then measured for different values of Ω imposed on the inner cylinder. The resistance, also known as viscosity, varies not only with speed but also with material properties. In total, the rotational viscometer measures torque, $M(mNm)$, frequence $, f, (Hz)$ and temperature, $T\ (°C)$. Figure 3. 5 (a) shows an illustration of the coaxial cylinder seen from the side, and Figure 3. 5 (b) illustrates the cylinder from above.

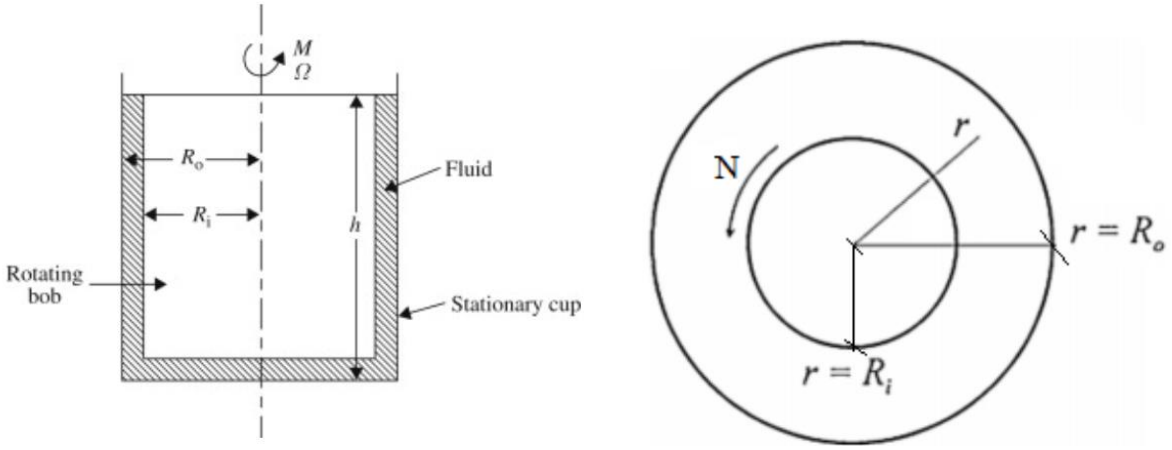

(a) Horizontal section of the coaxial cylinder viscometer (Takahashi, 1981).

(b) Vertical section of the coaxial cylinder viscometer

Figure 3. 5: Coaxial cylinder viscometer.

The viscometer tests were carried out on a Bohlin Visco 88 BV viscometer. The apparatus is illustrated in Figure 3. 4 (a-b) and consists of a coaxial cylinder geometry using the principle based on couette flow. It features eight rotational speed settings which induces a geometric progression between 20 to 1000 rpm. As the inner cylinder rotates according to specified speed, the resistance force is measured and given in torque.

From the measured torque and frequency, the viscosity, η $(Pa \cdot s)$, shear rate, $\dot{\gamma}$ $((1/s)$ and shear stress, τ (Pa), is calculated from apparatus. Note that the apparatus calculates viscosity and shear stress based on a Newtonian fluid. To be able to measure the material as a non-Newtonian fluid, point-wise measurements of the soil when it was sheared on a microscopic gap has been done. This could in retrospect present the non-Newtonian behavior of both soils.

The Bohlin Visco 88 BV viscometer was delivered with two different cylinders. In this study, only the smallest rotative cylinder with the smallest outer cylinder was used. By using the smaller cylinder, a lower torque was applied compared to the larger cylinder, and materials with higher viscosity could be measured. According to Wazer (1963), the annular gap between the cylinders must be at least10 times the diameter of the largest particle in the test sample. This is to retain a satisfying approximation of measuring continuum material. By using the smaller rotor and cup, a gap of 0.35 mm is retained. This permits testing of slurries with a maximum particle diameter of 0.035, which according to the grain size distribution, illustrated in Figure 5. 1, should be fine for kaolin, regarding BF clay, around 10% of the material is potentially too large. As later tests show, no large fluctuations occurred due to this. The cylinder dimensions are shown in Table 3. 2 and illustrated in Figure 3. 6 (a-c):

Table 3. 2: Cylinder Dimensions

$Measuring\ spindle(rotor)\ Radius, R_i\ [mm]$	$Outer\ cylinder\ (cup)\ Radius, R_0\ [mm]$	$Height, h\ [mm]$	R_0/R_i
7	7.7	21.1	1.1

Figure 3. 6: (a) rotor and outer cylinder, (b) diameter of rotor, (c) R_0/R_i, gap of 1.1

3.5.3 Measuring Constraints

Schramm (1994) presents six boundary conditions or basic assumptions for the measuring of viscosity.

- Laminar flow
- Steady State flow
- No slippage
- Homogenous sample
- No chemical or physical changes
- No elasticity

These assumptions are introduced to simplify the mathematical expression of fluid being deformed under the influence of shear force, which is vital for maintaining Newton's law of rheometry.

Laminar flow must be maintained when shear forces are applied. Maintaining a turbulent flow requires a significantly higher energy compared to laminar flow. The measured torque at a turbulent flow will no longer be proportional to the true viscosity, which could produce errors in the range of 50 to 100 % (Schramm, 1994).

Steady state flow Newton's law of rheometry is maintained through an applied shear stress, which is correlated with the shear rate. Only the shear stress that is sufficient to sustain a constant flow rate is applicable, all additional energy required to accelerate or deaccelerate the flow should not be accounted for in the mathematical expression (Schramm, 1994).

No slippage, this indicates that all shear stresses must be transmitted from the rotor across the liquid boundary into the liquid until the stationary boundary. Recordings are only made from the rotor, which means the velocity or resistance between the sample and the stationary boundary

won't be recorded. If slippage occurs between the stationary boundary and sample, the velocity profile will be unknown and the results meaningless (Schramm, 1994).

Homogenous sample is key to maintain uniformly shear throughout the specimen. The sample must stay homogenous during the whole test, which can be a challenge when higher shear forces are applied. Increased shearing can lead to phase separation, which implies that a dispersion separates into a thin liquid layer at the rotor or stationary boundary and the remaining sample becomes stagnant and solid within the rest of the gap (Schramm, 1994).

Chemical and physical changes such as hardening or physical transformations will act as secondary influences on viscosity. Soil conditions and properties are heavily affected by water content. Soils, which are tested for a long time will be affected by dehydration, which affects rheological properties.

Elasticity effects in the material is discussed by both Schramm (1994) and Major & Pierson (1992) in detail. For this study, the material established a centrifugal force, not a normal force which leaves that negligible amount of energy went into elastic energy.

3.5.4 Preparation, Calibration, and Steady State Conditions

The literature presents a variety of different ways to calibrate and ensure correctly measurements from the viscometer. Major & Pierson (1992) uses a special type of asphalt, which behaves as a homogenous single-phase Newtonian fluid, to ensure correct rheological properties. Bohlin88BV (2010) introduces on the other hand a more practical approach, not using a Newtonian fluid to calibrate it but readings from the torque effect on the rotor placed in an empty cylinder. For this study, (Bohlin88BV, 2010) method was applied.

The kaolin test samples were originally stored in 10 l bags in a cooling room, while BF clay was stored in cylinders. The needed sample size for viscometer tests is only supposed to fill the room between the outer and inner cylinder of the viscometer to ensure contact on both sides, illustrated in Figure 3. 7. The testing was carried out in the geotechnical laboratory, which had a temperature of approximately $23°C$. Before testing, sample clay was placed in the room and left to warm up. This was to ensure no temperature changes during the test. When desired temperature was attained, mixed samples could be placed in the cylinder and testing could start.

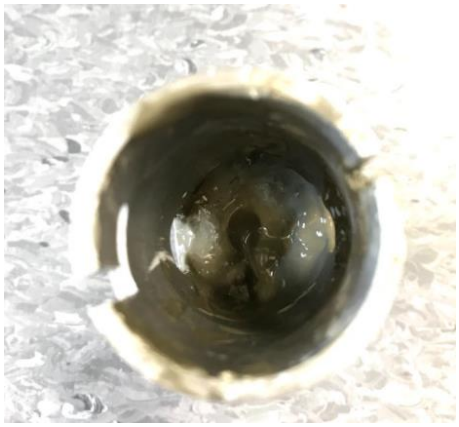

Figure 3. 7: Viscometer test sample represented by BF clay.

Steady state conditions were established by shearing the material until an equilibrium shear stress was obtained. This was done by applying rotational speeds between 20 rpm and 107 rpm, keeping it on each speed for several minutes. When the conditions stabilized, and the shear stress had a fluctuation below 3 pa for 30 seconds, steady state was assumed.

Tests were conducted, starting at the lowest speed, 20 rpm, before incrementally increasing the speed until every rotational speed was tested. Every test interval for each given speed lasted 120 seconds, where data after 5, 30, 60 and 120 second was sampled. One test consisted of 8 different velocities, resulting in 8 different shear stress – speed curves, consisting of 4 points each.

3.6 T-bar Penetrometer

The cylindrical T-bar was first used as an alternative to the conventional CPT tests for assessing the undrained strength profile on offshore soil investigations (Randolph et al. 1998). The T-bar penetrometer is commonly compared to the conventional cone penetrometer. However, the T-bar turns out to be advantageous due to flow mechanisms around the cylinder. These mechanisms can be interpreted using rigorous plasticity solution linking the bearing pressure to the soil strength (White et al., 2010).

T-bar tests were carried out on both unremolded and remolded soil samples of BF clay and kaolin clay at various strain rates. Cylindric containers with a height of 125mm and diameter of 72mm were used for both kaolin and BF clay. T-bar tests on BF-clay were conducted on samples from depths of 3.5m extracted from BH 13A. Both kaolin and BF samples were consolidated under dead weight for 24h before testing. The T-bar penetrometer is illustrated in Figure 3. 8. The probe contains a cylindrical bar attached perpendicular to a penetrometer rod/shaft, just below a load cell. The cylindrical bar is 0.5 mm diameter and 4mm long connected to a 250mm long shaft. In order to investigate sufficient strain rate intervals on soft clays, the T-bar was designed to velocities up to 50 mm/s holding a sufficient sampling frequency. However, a max load of 25N was set to ensure little bending and small deformations of the T-bar shaft and cylinder.

Figure 3. 8: T-bar cylinder dimensions and apparatus

Interpretation and theoretical assumptions for shallow T-bar

The undrained penetration resistance, q, is mainly governed by 2 elements, namely the undrained soil shear strength, Su, and the bearing factor, Nt. However, buoyance of the soil together with shaft friction can be introduced as additional components of the resistance. The effect of buoyance arises as a result of the higher soil density relative to the water, resulting in a higher work required to lift the soil displaced by the bar(White et al., 2010). This effect together with shaft friction is

dependent on the penetration depth and embedment which reflects the patterns of heave controlled by the changing soil flow mechanisms. White & Randolph (2008) distinguishes between shallow and deep embedment introducing a buoyancy factor, N_b. The undrained penetration resistance can then be expressed as:

$$q = N_T S_u + N_b \gamma' w \tag{3.2}$$

where N_b is the buoyancy factor, N_T is the bearing factor which can be distinguished into N_{T-deep} and $N_{T-shallow}$, γ' is the effective density and w is the datum for the depth. The mechanisms relating to deep and shallow embedment are illustrated by White et al. (2010) in Figure 3. 9.

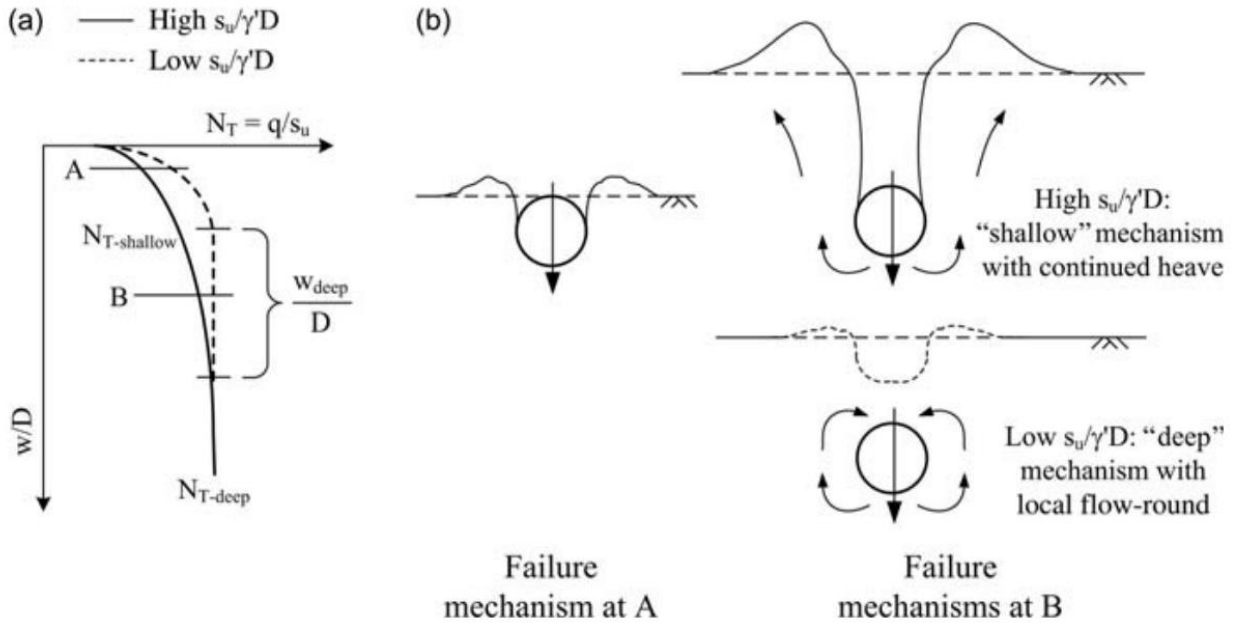

Figure 3. 9: Idealized behavior related to shallow and deep T-bar penetrations. (a) change in bearing factor with depth, (b) shallow and deep failure mechanisms (White et al., 2010).

When considering deep failure mechanisms, a simplification of Eq.3.2 can be made by adjusting for the buoyancy effects.

$$S_u = \frac{q}{N_{T-deep}} \tag{3.3}$$

Literature specifies that the N_{t-deep} factor is dependent on the buoyancy and roughness of the interface, which ranges from 9.14 for fully smooth interface to 11.94 for a rigid interface (Randolph & Houlsby, 1984). The T-bar is normally neither fully smooth nor fully rigid, therefore and based on experimental calibration, a $N_{T-deep} = 10.5$ is commonly adopted. However, these assumptions are based on an ideal rigid plastic soil. More recent literature (Einav & Randolph, 2005; Lunne et al., 2005) suggests that the bearing factor is dependent on the difference in operative undrained strength, the effect of strain softening and rate dependency.

Another important quantity is at which depth the transition between a shallow failure mechanism and deep failure mechanisms occurs. White et al. (2010) specifies that this transition is influenced by the undrained shear strength, effective soil density and bar diameter, and can be expressed as the dimensionless formulation: $S_u/\gamma' D$. This quantity describes the transition from $N_{T-shallow}$ to N_{T-deep}, affecting the relative resistance to a surface failure and flow around mechanism. Such mechanisms can be seen in Figure 3. 9 (b), illustrating a greater heave mechanism for shallow failure compared to deep failure.

White et al. (2010) suggested formulation of the variation in bearing factor with embedment considering both shallow and deep failure mechanisms. The influence of the soil buoyancy increases as the bar becomes more embedded. This is, as mentioned, due to the higher soil density relative to the water. When heave is ignored, this uplifting force can be expressed as $\gamma' A_s$ where A_s is the cross-sectional area below the soil surface. However, White & Randolph (2008) discovered that during shallow penetration this buoyancy is increased by the local heave. This enhancement can be expressed as a factor f_b, such that the buoyancy factor N_b from Eq. 3.2 can be expressed as:

$$N_b = f_b \frac{A_s}{Dw} \tag{3.4}$$

f_b was found to be ~1.5 for shallow penetrations with great effects of heave. To connect the shallow failure mechanisms with the flow around, White et al. (2010) defined a depth, w_{deep}, at which the failure mechanism changed. Hence, it is assumed that f_b decreases from 1.5 as a linear function before it reaches a minimum value of the unity at the critical depth, w_{deep}.

$$f_b = \max\left[1, 1 + 0.5\left(1 - \frac{w}{w_{deep}}\right)\right] \tag{3.5}$$

By introducing a measurement to the contributed resistance from buoyancy, a penetration resistance related to the penetration resistance alone can be established:

$$q_{soil} = q - N_b \gamma' w \tag{3.6}$$

And expressed through the bearing factor:

$$N_{T-shallow} = \frac{q_{soil}}{S_u} \tag{3.7}$$

$N_{T-shallow}$ can conveniently be expressed as a quantity of the deep factor N_{T-deep} that depends on the embedment relative to the transition depth of the failure mechanism, w_{deep}. Hossain et al. (2005) and later verified by White et al. (2010) argued that the same quantity is also dependent on the strength ratio $S_u/\gamma' D$, giving a general expression for correcting shallow T-bar data:

$$\left(\frac{N_{T-shallow}}{N_{T-deep}}\right) = f\left(\frac{w}{w_{deep}}, \frac{S_u}{\gamma' D}\right) \tag{3.8}$$

A formulation of w_{deep} is found by White et al. (2010) through numerical modelling based on the relationship of $S_u/\gamma' D$ and w_{deep}. This resulted in the following two term power function:

$$w_{deep} = 2.58\left(\frac{S_u}{\gamma' D}\right)^{0.46} + 0.24\left(\frac{S_u}{\gamma' D}\right)^{-0.63} \quad (3.9)$$

At depths under w_{deep}, a shallow bearing capacity is appropriate. Based on a series of large deformation finite element (LDFE) analysis conducted by White et al. (2010), a simple expression of $N_{T-shallow}$can be derived:

$$N_{T-shallow} = 2 + \left(N_{T-deep} - 2\right)\left(\frac{w}{w_{deep}}\right)^{p} \rightarrow p = 0.61\left(\frac{S_u}{\gamma' D}\right)^{-0.31} \quad (3.10)$$

The entire T-bar interpretation procedure is inspired by White et al. (2010) and illustrated in Figure 3. 10. This procedure is established through numerical modelling and experimental testing with kaolin. One of the assumptions made, is that the correlations of Eq. 3.9 and 3.10 are applicable to the conducted experiments.

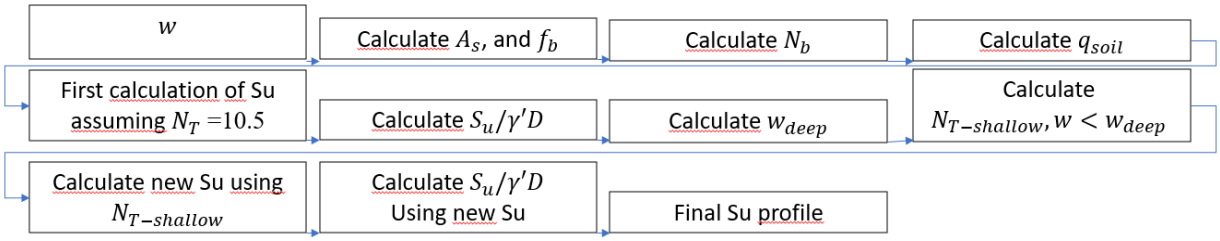

Figure 3. 10:T-bar interpretation procedure

Method

The T-bar penetrometer was carried out in the geotechnical lab at NTNU in the winter of 2021/2022 and build specific for this project. An actuator was used during testing to penetrate the T-bar to a depth of 100mm and then cycle the penetrations between 50 mm and 100mm until fully remolded sample. In total, rate effects on 4 kaolin samples and 2 BF samples were investigated. Initially each sample was performed using a pre-determined speed, which for kaolin was: 1mm/s, 3mm/s, 10mm/s and 30mm/s, and for BF clay, 3mm/s and 30mm/s. Following the initial penetration sequence and the remolding of the material, penetration rates of 0.3, 1, 3, 10, 30 and 50 mm/s containing 1 cycle were subjected on each sample. This ensured that a sufficient range of strain rates on the remolded samples could be investigated. The procedure for estimating the undrained shear strength is presented in "Interpretation and theoretical assumptions for shallow T-bar", and the converted strain rates are presented in chapter 5.1.3. Figure 3. 11and Figure 3. 12 shows the samples before, during and after cycling.

Figure 3. 11: Shows BF clay at 85% water content, from left: before cycling, middle: during cycling, right: after cycling (this sample is cut in half showing the middle of the sample).

Figure 3. 12: Shows Kaolin clay at 62% water content, from left: before cycling, middle: during cycling, right: after cycling.

3.7 Element Testing

For this study, element testing was carried out using cyclic triaxial and DSScy experiments. Triaxial tests were conducted in the geotechnical laboratory at NTNU, while DSScy tests were conducted at NGI's lab in Oslo. Triaxial tests and DSS tests represents both different ways of shearing the material. Where the triaxial test is exposed to a vertical deformation, the DSS tests are sheared horizontally. Testing is done using a sample enclosed in a membrane and consolidated under determined effective stresses. Applied strain rate can be determined based on the purpose of the experiment. Both static DSS and triaxial compression tests are typical in the order of 1-5%/h. However, when testing strain rate dependency for slurries related to earthquakes, submarine slides or impact forces from submarine slide, testing a large interval of axial strain rates are more interesting. Therefore, axial strain rates in the magnitude of 3%/h, 60%/h and 1200%/h were conducted on cyclic triaxial apparatus. For the DSS test, shear strain rates of ≈ 90%/h , 4320%/h and 216000%/h were conducted. This section will introduce method, equipment, preparations of materials, consolidation, and shearing phase. The preparations and procedures for the DSScy tests

were done following NGI routines and handbooks in contrary to the triaxial tests. The different procedures and assumptions will be highlighted in this section.

Test Conditions

Cyclic triaxial and DSScy tests are conducted to map cyclic behavior, mechanical properties, and strain rate effects of clays at Bjørnafjorden and the provided kaolin clay. The tests were completed in undrained conditions to simulate the initiating, slide conditions and impact forces of a submarine slide. This assured no volume change and an excess pore pressure development during shearing were produced. The testing program was designed to define and compare the soil response between BF and kaolin clay over a wide range of strain rates. The test conditions were identical for BF and kaolin regarding strain rates, cell pressure during shearing, effective stresses, consolidation time and consolidation conditions. If procedures deviate between the kaolin and BF tests, they are evaluated and found necessary, due to either practical implementation or soil behavior.

For this test program, the Triaxial and DSS tests uses different mechanisms and were conducted for different depths using independent procedures. The tests are therefore not directly comparable, but general soil behavior can be related between the two test types.

The cyclic triaxial methods and results are included in Appendix A, and not used to present the generalized behavior of kaolin and BF clay. This is due to several reasons, among these are: large uncertainties regarding implementation of extremely soft clay, the general results exhibiting unphysical behavior and the necessary data processing. However, a justified discussion for the triaxial tests is included in the Appendix A.

3.7.1 DSScy

In direct simple shear (DSS), conditions of applied shear strain are imposed to the specimen, as illustrated in Figure 2. 16. The horizontal and vertical shear forces are measured during shear, and the shear strain, γ_{xy}, can be derived from shear displacement for given height, u/h_0. Undrained are, for simplicity, simulated by holding the volume of the specimen constant. This implies a shear phase where the vertical stresses changes to maintain constant volume. This change in vertical stress can be defined as the change in pore pressure (excess pore pressure) what would have been measured in a truly undrained test with constant total axial stress.

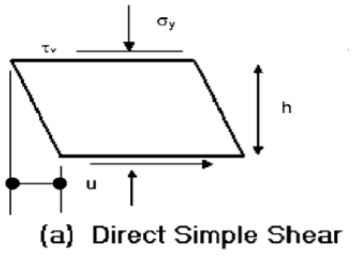

Figure 2. 16: conditions of a DSS test (Hanzawa et al., 2007)

Method

Using equipment and procedures from NGI, calibration of apparatus and equipment was done by lab technicians there. The specimens were 67 mm in diameter giving an area of 35.3cm^2, and target height of 16mm (one test ended up having 13.8mm height). This gives a height to diameter ratio of 0.24 at 16mm height. The sample area is kept constant while deformations can occur vertical.

This is ensured by a reinforced rubber membrane which restricts deformations in radial directions but allows strains in axial direction and simple shear.

However, the shear strain was set to 15% based on the assumption of an 16mm sample height, which is 2.4mm horizontal deformation. The shear strain is therefore approximately 15% for every test, where the deviation varies depending on the height.

Equipment

A total of 6 strain-controlled tests with 3 different strain rates were conducted for this study. These strain controlled DSScy tests were conducted on both BF and kaolin clay, with one test for each speed. For each test a minimum of 30 cycles were completed to ensure residual strength which captured the cyclic dependency towards shear strength.

A GDS Dynamic DSS Testing System was used to conduct the tests, designed for cyclic testing at high shear rates. This established opportunities to run all tests using the software, enabling shearing based on a sinus period (unlike the triaxial device).

Preparation Bjørnafjorden clay

The DSScy on BF clay were conducted from BH-13A 7.10-7.83m and carried out according to *NS-EN ISO 17892-8* (2018). To ensure a good sample quality soil between 7.35 and 7.65m were used for DSScy.

Preparation Kaolin clay

For DSScy tests, 22kg kaolin with a water content of 1.5LI was mixed for 1h using a kitchen machine. Trapped air was extracted with using a vacuum pump for 1h after mixing and finally the slurry was placed in a consolidation box. The kaolin slurry was pre-consolidated in a $27 \cdot 27\ cm^2$consolidation box, making it big enough for consolidating all tests simultaneously, which ensured identical conditions for all tests. Before pre-consolidation the kaolin slurry reached a height of 23cm. The double drained consolidation box (illustrated in Figure 2. 17) was cleaned and sealed with silicone grease before filter and the mixed kaolin was inserted.

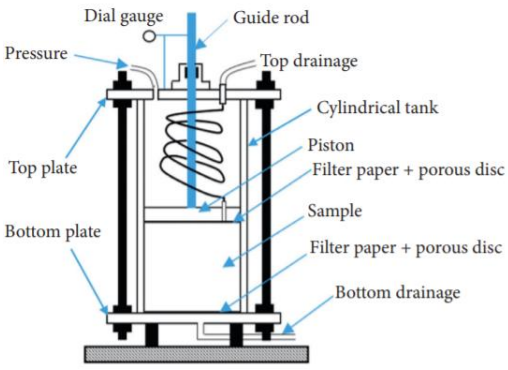

Figure 2. 17: consolidation box and set up for kaolin sample preparation

The aim of the pre-consolidation is practical implementation without disturbing the soil structure. Hence, the pre-consolidation was set to reach only 50% of the initial consolidation pressure, σ_c', which is also NGI procedure. This was accomplished by incrementally loading the soil until a desired stress of 19 kpa was reached. This was applied through 4 load steps, where the 3 firsts steps lasted 24-48h and the last step 5 days. The necessary time for each load step was determined

by time of primary consolidation, t_p. The remaining height after consolidation was 13.5cm, resulting in a 40% volume change.

Figure 2. 18 shows the pre-consolidated kaolin sample and its division. The sample was divided into 9 identical blocks, which was stored in approximately 1 month as a compensation for coercive stresses. Each sample was stored with double layer of plastic with a wet piece of paper inside, to maintain the humidity. Each block had an area of 9x9 cm^2 and a height of 13.5cm.

a) b) c)

Figure 2. 18: (a-c) Pre-consolidated kaolin clay from the NGI lab, consolidation stress is 19 kpa, area is 27^2 cm^2 and height is 13.5 cm

Sample preparation and Consolidation

For each DSScy test a new sample of BF clay (d=72mm and h = 70mm) or block of kaolin clay (area = 90x90mm^2) and h=135mm was used. The sample is pressed into a cutting cylinder, which is mounted on vertical guides. Excess clay is cut away by a wire saw, spatula, or finger in this operation. Bottom and top filter caps are carefully mounted, and the reinforced rubber membrane is gently pressed over the clay sample with the help of a suction cylinder. The specimen, holding the top and bottom caps and reinforced membrane, is the transferred to the DSS apparatus. Figure 2. 19 illustrates the process from intact specimen to a ready DSS sample. Figure 2. 19 e and f illustrate the effect of patching, a convenient and widely accepted procedure for disturbed samples.

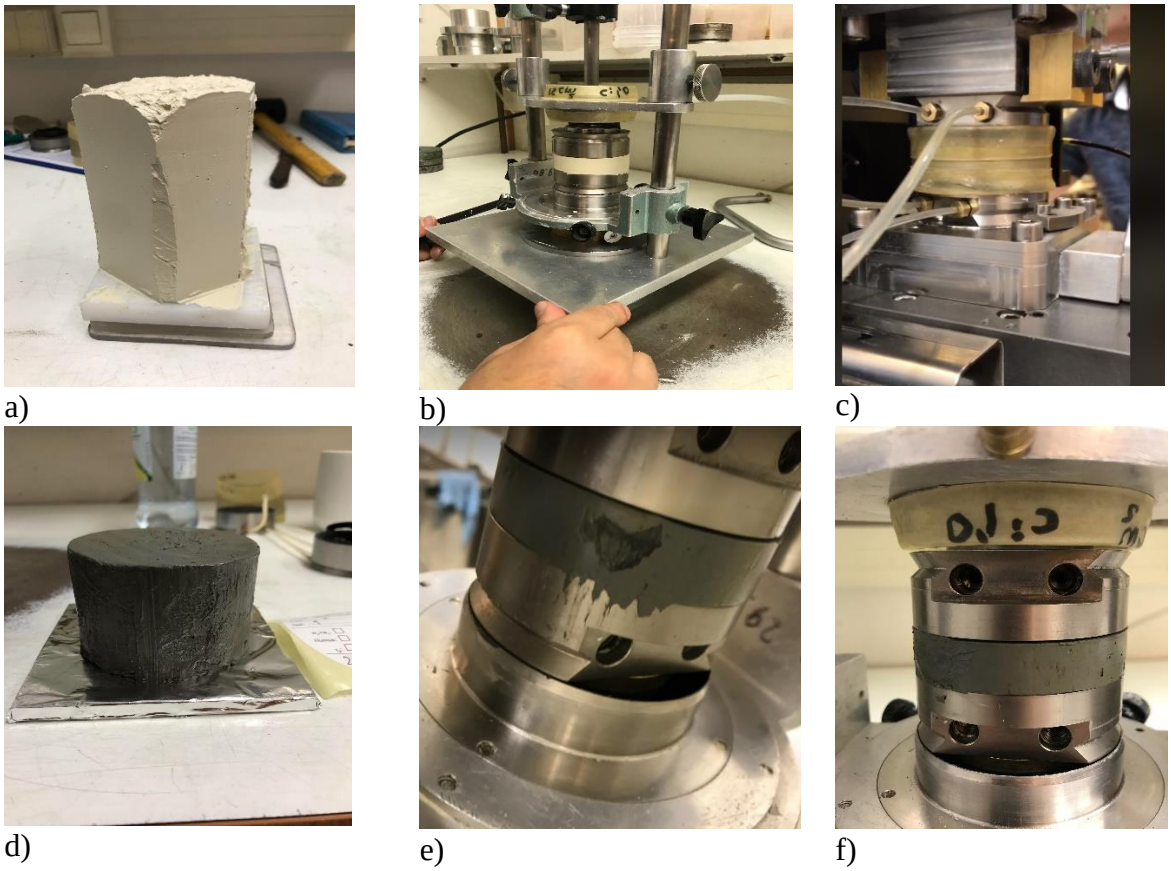

a) b) c)

d) e) f)

Figure 2. 19: Pictures of sample preparations for DSS tests. (a) illustrates a kaolin block used for one DSS test, (b) is one DSS sample before membrane is placed on, (c) illustrated build in sample, (d) is an initial BF-clay sample, (e) is an illustration of disturbed BF sample, (f) shows the effect of patching.

All 6 DSS tests were consolidated according to the estimated consolidation stress, σ_c', found in (NGI, 2019c). To ensure identical conditions during testing, a final reference consolidation stress was chosen. This was based on a depth of 7.5 m, which estimated an $\sigma_c' = 37.5\ kpa$ (approximately 2x the pre-consolidation stress of the manufactured kaolin). Consolidation, according to NGI procedures, is done in a 4-step load sequence. Each load step increases the stresses incrementally in a K_0 situation and is hold for a minimum of 30 minutes (depending on t_{90}). The last load phase is then left for 17h before shearing. This 4-step load sequence is important for evaluating and correcting for membrane effects, which is implemented during a calibration step before shearing.

Shearing

The specimen is sheared at a constant rate of strain in an undrained environment. During shearing, the volume is kept constant from the consolidation stage while cyclic horizontal shearing is applied. The tests have been performed with a symmetric strain period, having a 2.4mm (~15%) amplitude in both directions, giving each cycle a total deformation of 9.6mm. Due to variations in sample heights, some specimens ended up with a higher and lower shear strain than 15%. The

large spectrum of shear rates implied large time variations for the shearing stage. See Table 3. 3 for more information.

Table 3. 3: Tests conditions for DSScy where used strain rate represents strain rates presented in Results and discussion

Parameter	*Kaolin Clay*			*BF Clay*		
Test id	$DSS_{K1.1.1}$	$DSS_{K2.2.2}$	$DSS_{K3.3.3}$	$DSS_{BF1.1.1}$	$DSS_{BF2.2.2}$	$DSS_{BF3.3.3}$
Water content (%)	59.2	52.1	50.8	48.9	48.8	48.7
Consolidation stress, σ_c (kPa)	37.5	37.5	37.5	37.5	37.5	37.5
Velocity (mm/s)	9.6	0.192	0.00385	9.6	0.192	0.00385
Frequency (Hz)	1	0.02	0.0004	1	0.02	0.0004
Height (mm)	16.1	16.2	15.8	16.0	16.0	13.8
Amplitude (mm)	2.4	2.4	2.4	2.4	2.4	2.4
Disp. each cycle(mm)	9.6	9.6	9.6	9.6	9.6	9.6
Calculated Strain rate(s^{-1})	0.59	0.0118	$2.44 \cdot 10^{-4}$	0.6	0.012	$2.79 \cdot 10^{-4}$
Used Strain rate (s^{-1})	0.6	0.012	$2.5 \cdot 10^{-4}$	0.6	0.012	$2.5 \cdot 10^{-4}$
Number of cycles (N)	200	50	30	200	50	101

3.7.2 Membrane Effects

It is widely accepted that rubber membranes enclosing test specimens in both triaxial and DSS tests give rise to an apparent increase in strength Henkel & Gilbert (1952). In a triaxial test, the specimen is sealed against each end piece, while a DSS test it is reinforced with steel rings, both affecting the shear strength.

As the poisons ratio of clay is identical with that of the rubber for an undrained triaxial test, no circumstantial tensions will occur in the rubber provided full contact and identical deformations. However, as Henkel & Gilbert (1952) pointed out, for any small deviations in contact between membrane and clay sample, a buckling effect due to hoop tension, which is associated with the circumferential strains of the specimen, will occur during deformation. This, together with the assumption that it may act as a reinforcing compression shell outside the sample, one could argue that the actual mode of the rubber will be a complex combination these two effects. *NS-EN ISO 17892-9* (2018) suggests a correction estimation for elastic membrane on triaxial tests, which is given as follows:

Total vertical stress:

$$(\Delta\sigma_v)_m = \frac{4 \cdot t_m \cdot E_m}{D_m} \cdot \left((\epsilon_v)_m + \frac{(\epsilon_{vol})_m}{3} \right) \tag{3.11}$$

Total horizontal stress:

$$(\Delta\sigma_h)_m = \frac{4 \cdot t_m \cdot E_m}{D_m} \cdot \frac{(\epsilon_{vol})_m}{3} \tag{3.12}$$

where $(\sigma_h)_m$ is the correction in horizontal direction and $(\sigma_v)_m$ is the correction in vertical direction. t_m represents the initial thickness of unstressed membrane and E_m is the elastic modulus. D_m is the internal diameter of confining membrane, while $(\epsilon_v)_m$ is the vertical strain and $(\epsilon_{vol})_m$ is the volumetric strain of the membrane.

These formulas assume no slippage between the specimen and membrane, implying that the membrane deforms as the specimen. They are also not valid after the formation of shear planes (*NS-EN ISO 17892-9*, 2018). For soft soil these effects can be great and result in overshadowing the true material properties.

Test mechanisms related to undrained DSScy tests are only influenced in the horizontal shear direction. The influence of membrane effects will as a consequence be narrowed down to influences in only lateral direction.

Conversations with Rune Dyvik (Technical expert at NGI) further revealed that DSScy tests are more suited than cyclic triaxial tests for testing cyclic rate dependency on very soft clay. This has to do with sample size, volume and area changes which happens during consolidation and shearing of the specimen. For this study membrane corrections were established by NGI and slightly modified to describe related effective stress path and hysteresis loops. This is further discussed in chapter 5.1.4.

4. Flume Model and Testing Procedures

4.1 Introduction

Small scale model tests of submarine slides supplemented with laboratory experiments can be considered as the main basis of this study. Investigating debris flow behavior and flow impact force based on material properties has been conducted through a flume model with changing inclination. Figure 4. 1 presents the model flume used for the conducted model experiments.

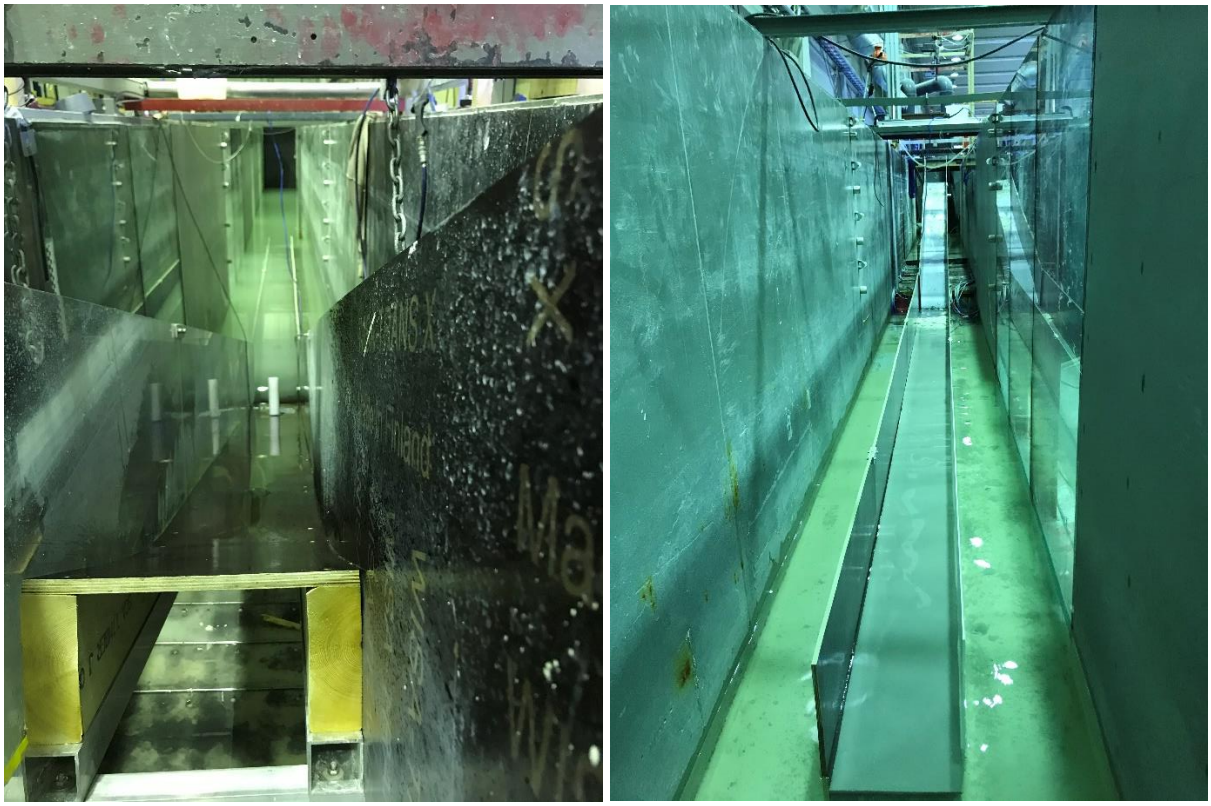

Figure 4. 1: Empty model flume at NTNU Hydrolab. Left picture shows the impact pile placed in the middle of the flume, approximately 2.75m from the slide initiating area.

This chapter will give a detailed description of the NTNU flume model, the performed experiments, and the experimental set up following such tests. The model tests were conducted on both 12° and 18° inclination in the summer of 2021. Due to a unique test setup, procedures and routines had to be established before testing. Such procedures were discovered by using sand as test material. In total 4 model tests with sand were conducted, but these tests will not be described in this thesis. During this period 21 conducted model tests involving kaolin clay were conducted. Kaolin slurries were mixed based on the same methods described in 3.3.3, and tested with various water contents and degree of consolidation in the flume model. In the end, 3 run out simulations

and 18 impacts tests were considered. A full list of conducted tests including model and material parameters is found in Table 4. 1.

While conducting the model tests, several boundary conditions, limitations, and assumptions were investigated and made. Conducted tests were simulated assuming homogenous soil conditions before initiation. During sliding, well developed debris flow conditions were simulated in a controlled environment. This meant a pre-determined slide path surrounded with a defined run-out channel, slope, and deposition area. Initiation was triggered mechanically providing some uncertainty regarding initiating force. However, this seems to be negligible considering the results. The flow bed and sidewall contain a low roughness providing the same conditions for the whole slide path. Effects and theory of slide initiation in relations to dynamics of tidal waves and tsunamis will not be discussed in this thesis. However, physical observations regarding these effects will be pointed out in presented results. Also, water entrainment and resistance to flow from the surface of the model was not investigated due to practical challenges. The rheological characteristics of the debris material were therefore assumed to be uniform and similar from the slide initiation. Assuming small amounts of water entrainment is supported by Yin & Rui (2018), based on their laboratory studies on kaolin debris flows.

4.2 Test Plan

For the issues and challenges related to Bjørnafjorden, an understanding of the slide behavior related to impact forces and slide run out were important. The motivation behind the performed model tests is to capture the slide and impact behavior based on material and rheological properties, strain rate dependency and flow behavior.

Based on viscometer and fall cone tests, and literature study, using kaolin with a water content between 80 and 110% seemed appropriate. Aiming for different water contents change in material and rheological properties can be investigated and evaluated against flow behavior and impact forces. To extend this research further, effects of consolidation are measured by testing remolded material vs 24 hours consolidated material. By investigating this using two different slopes (12° and 18°), slide behavior and impact forces related to both material/rheological properties and flow properties can be examined and compared.

Physical challenges regarding measurements and implementation of the run-out tests determined the amount conducted run-out tests. These were significantly more time and resource consuming compared to impact tests. This led to consistently more impact testing compared to run-out testing, which resulted in (as mentioned) 3 run-out tests and 18 impact-tests. All the run-out tests were conducted on a slope with 18° inclination. In the end 12 impact tests had been performed on slopes of 18° inclination with water contents between 82-113%, and 6 impact tests on 12° inclination having a water content between 89-110%, as presented in Table 4. 1.

Table 4. 1: Executed model tests

Test [−]	***Objective*** [−]	***Tilt*** [***degrees***]	***State*** [−]	***wc*** [%]
1	*Run − out*	18	*Remoulded*	105
4	*Impact*	18	*Remoulded*	82
5	*Impact*	18	*Remoulded*	85
6	*Impact*	18	*Remoulded*	86
7	*Impact*	18	*Remoulded*	110
2	*Run − out*	18	1*d consolidated*	94
3	*Run − out*	18	1*d consolidated*	100
8	*Impact*	18	1*d consolidated*	81
9	*Impact*	18	1*d consolidated*	85
10	*Impact*	18	1*d consolidated*	86
11	*Impact*	18	1*d consolidated*	91
12	*Impact*	18	1*d consolidated*	96
13	*Impact*	18	1*d consolidated*	103
14	*Impact*	18	1*d consolidated*	107
15	*Impact*	18	1*d consolidated*	113
16	*Impact*	12	*Remoulded*	89
17	*Impact*	12	*Remoulded*	95
18	*Impact*	12	*Remoulded*	110
19	*Impact*	12	1*d consolidated*	99
20	*Impact*	12	1*d consolidated*	100
21	*Impact*	12	1*d consolidated*	109

4.3 Flume Model and Instrumental Set-up

The flume model consists of two parts designed to capture the various flow regimes. The first part (part A) simulates slide initiation, acceleration and run-out of the slide material. To accommodate a realistic Bjørnafjorden situation, this section of the slope was set to 12° and 18°. In total this acceleration section was set to 4m long. The second part (part B) can be considered the deposition area with an 2° inclination and length of 6m. The cross section of the flume is 30cm width and 30 cm high for both parts. Figure 4. 2 provides a schematic representation of the full flume model at 18°, this model is identical for the 12°.

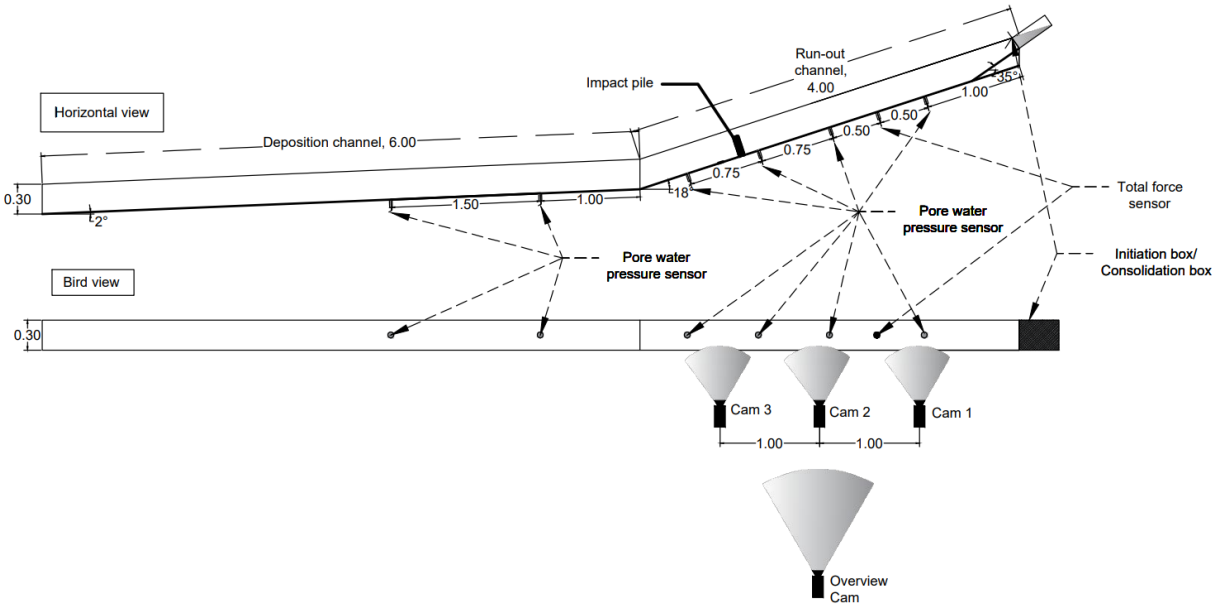

Figure 4. 2: Schematic representation of the experimental set up at inclination of 18°. *Above is a horizontal profile of the flume model, below is the flume model seen from above. Both illustrations are aligned and represents identical models. All dimensions are given in meters.*

A metallic consolidation box was used for measuring, holding, consolidation and triggering/realizing tested material. The box was contained following dimensions: $60X30X10cm^3$ and weighing 8kg. All conducted tests contained identical volume: $40X30X10\ cm^3$, which translated to 16 kg kaolin. The sampled were either remolded or 1 day consolidated. 16 kg kaolin samples were remolded with a paint mixer before placed in the consolidation box. Remolded tests were conducted directly after filling the box, while consolidated tests consolidated for 24h before released. A more detailed description is found in Appendix C.

The model was instrumented with 6 spring-controlled pore-water pressure sensors (illustrated in Figure 4. 2) providing pore pressure data for the whole slide process. All pressure sensors were placed in the model bed and recorded data with a frequency of 1000Hz, securing detailed measurements and the capability of data-processing. In total 4 video cameras were placed to capture the flow behavior in the run-out channel (illustrated in Figure 4. 2). 3 cameras (Cam1, Cam2, Cam3) were placed close to the water tank, giving detailed observations of the slide. And 1 (overview cam) camera observed the whole slide process in the run-out channel. All cameras observed the model tests through plexiglass, due to lack of transparent glass in the deposition channel, no cameras were placed here. 1 total force sensor was placed 1.5m from the slide initiation to record the resulting slide pressure. For tests where impact forces were measure, an impact pile was installed 2.75m from the slide initiation just behind pore pressure sensor 3).

The total water tank which was used had an approximately capacity of 65 cubic meters, stretching over 20m long, 1.5m width and 2m high.

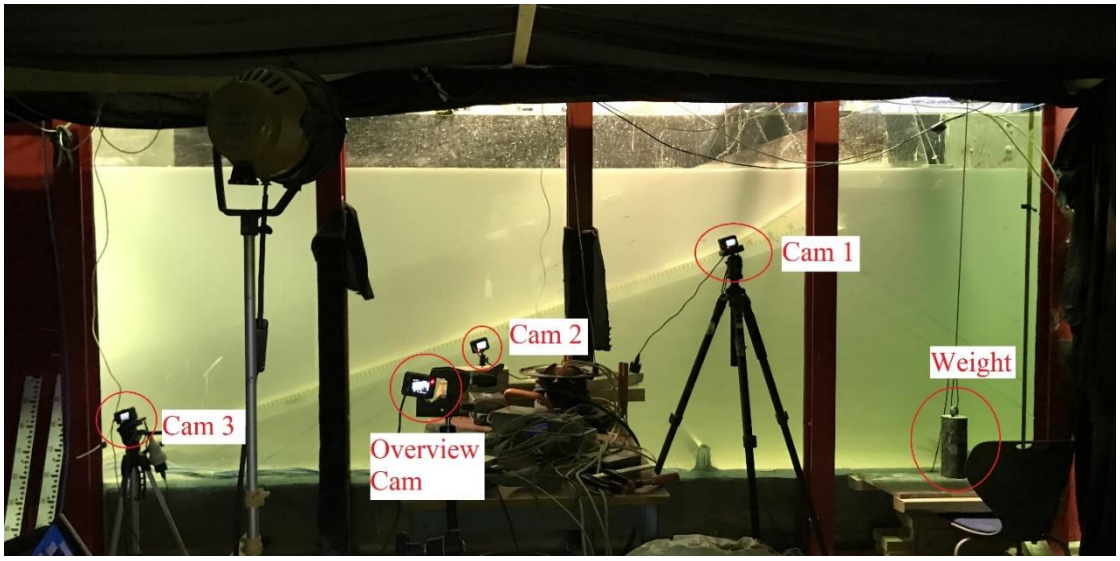

Figure 4. 3: illustration of the run-out part including camera set-up. Here the cameras are tilted to establish a flat camera surface for the video recordings. However, during testing these were placed horizontally, to capture the slope of the flume, as can be seen in Figure 4. 1.

a) 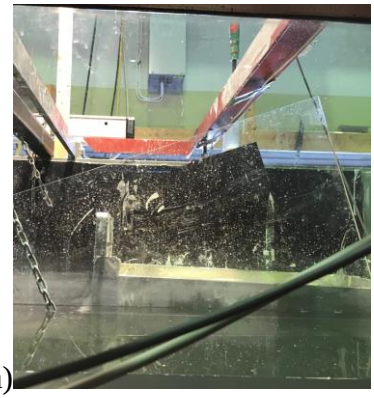
b) 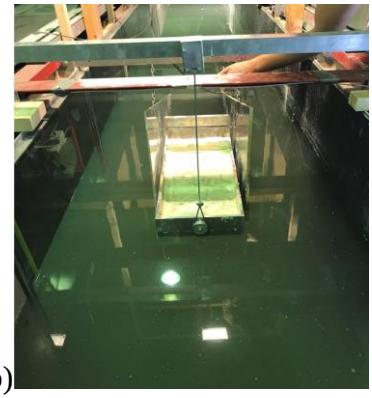
c) 
d) 
e) 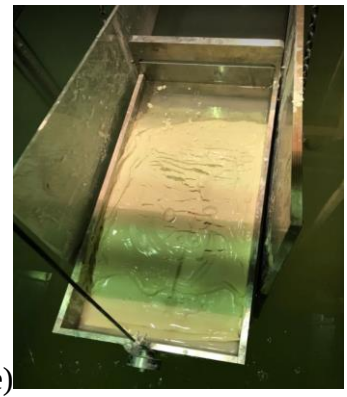
f) 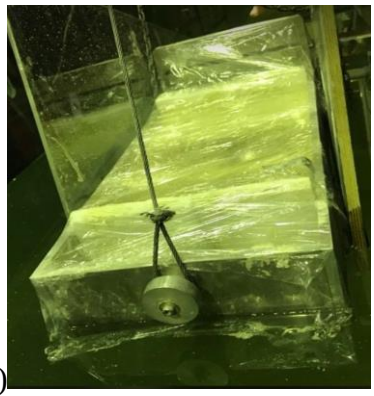

Figure 4. 4(a-f): (a, b, d, e, and f) illustrates the trigger box and position before initiation. (f) illustrates how the samples were wrapped in foil during consolidation. (c) illustrates the box after triggering, here the angle of the box is 35°.

4.4 Testing Procedure

In total, 2 different types of tests were conducted: run-out tests and impact tests. Both tests were conducted for remolded and 1day consolidated kaolin clay. This gives 4 different (but quite similar) testing procedures. This section will introduce the procedures and routines established for the model tests. This will be explained by describing the general procedure and point out the differences between the different tests. Due to the amount of instrumentation and preparation general preparations for the experiments, such model tests required two people working hands on.

Preparation and Initiation part

A measured amount of kaolin clay with pre-determined water content was mixed and remolded using a paint mixer. After establishing homogenous conditions, the slurry was placed in the consolidation/triggering box. For every test, water content was determined based on procedures from (*NS 8013*, 1982). For experiments with *consolidated clay*, two layers of plastic foil was wrapped around the box, ensuring minimal effects of dehydration. After wrapping, the box was placed into position as illustrated in Figure 4. 4 (f) and remained there for 24h (pre-determined consolidation time). This plastic was afterwards removed when consolidation was finished (before slide initiation). For remolded experiments, no plastic foil was used. After filling the box with desired amount of clay it was placed in to position ready for slide initiation, as illustrated in Figure 4. 4 (e). After placing the triggering box in position, desired water level in the water tank had to be established. This was determined to be on the same level as highest point of the clay, meaning that the whole sample was submerged by the water (see Figure 4. 4e). To establish desired water level, huge water pumps was used. These were turned off again after desired water level was reached. Due to change in water level, pore pressure sensor was recalibrated while total force and impact pile (if it was used) checked for instrumental noise. Afterwards, cameras were turned on and set to recording speed of 100 fps, pore pressure sensors, total force and impact pile (if used) were set to record at 1000Hz. Before initiation a slip surface was established by sliding a thin metal wire between soil and box surface. The gate, holding the kaolin clay in place, was opened as the last check point before initiation. Initiation was performed by releasing a weight a pre-determined distance, tilting the triggering box 35 degrees, and releasing the clay.

The only difference between the various test-procedures regarding preparation and initiation is if the soil must consolidate, and if an impact pile is installed.

Post slide preparation and documenting

After conducting specific experiment, the cameras and data acquisition programs were stopped. The triggering box was weighed, and residual material determined. For run-out tests the water tank was emptied, and necessary documentation was conducted, such as run-out length, dispersal of the mass, and water content (to decide water intrusion and remolding). After documentation, the slide masses were collected in buckets, and the flume was washed and prepared for a new test. Filling and emptying the water tank took up to 8 hours and required large amounts of water which set a limit on the number of trials that could be conducted. For the impact force tests, water was not extracted from the water tank. This was not considered necessary, as only the area

between the slide initiation and impact pile was assessed. The run-out channel was cleaned by using a broom, pushing the remaining slide masses past the impact pile. Necessary documentation was provided by the cameras or pictures taken after the slide event. This procedure proved to be much more time and water efficient.

4.5 Data Processing

This section outlines and describes the processing of the raw data collected from pore pressure sensor, total force sensors, video cameras, and impact pile. Assessing single impacts and short duration pore pressure measurements, a high sampling frequency sufficient to capture a true peak force is necessary. This study investigates both short single impacts and longer bulk impacts in order to characterize the true velocity and impact forces from the model slide. High and consistent sampling rate can be considered as necessary to reconstruct the slide behavior providing a better basis to evaluate and establish proper engineering design judgements. Nyquist & Shannon (1949) presented a theorem stating the required sample frequency to ensure no loss of information. This theorem states the necessity to sample twice or more the signal frequency to maintain no loss of information:

$$f_{scan} \geq 2f_{max} \tag{4.1}$$

Considering the refined dataset with a maximum frequency (f_{max}), Eq. 4.1 demands a scan frequency (f_{scan}) two times the maximum sample frequency. How the sample frequency should be estimated depends on the area of investigation and will be discussed for each parameter.

4.5.1 Video Analysis

The video recordings were primarily used for observations related to slide and flow behavior, and to calculate flow front velocities. Tracker, a video analysis and modelling tool for video recordings, proved to be a sufficient software for this purpose. By assigning an object a certain position according to a selected coordinates system, velocity and acceleration can be calculated based on given position in a 2D space. Figure 4. 5 illustrates the interface and modelling in Tracker.

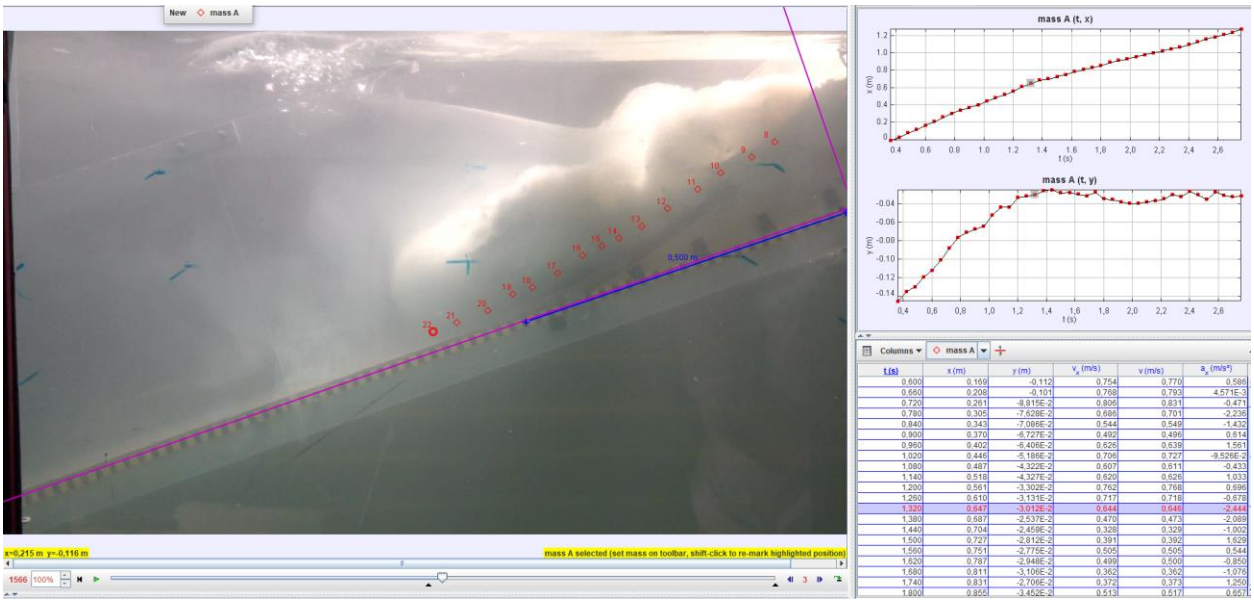

Figure 4. 5: Tracker interface and modelling tool. Model slide Test 11 can be seen here.

The blue 0.5m line marks the calibration line, which relates the recorded tracking to the real experiment. The pink lines going parallel and perpendicular to the slide path represents the coordinate system, while the red dots indicate the established tracking points represented relative to the coordinate system. The amount of tracking points is user defined but limited to the specific frame rate set by the camera. The cameras were initially set to record in 100 frames per second (fps), and for the video-processing, every third frame was used to track the slide, initially giving a tracking frequency of 33.3Hz.

Using image modelling to determine velocity profiles provides certain limitations. The first, and probably most influential one is the human factor. The positioning of each tracking points is placed by hand. This can cause inconsistency in the gathered data, which ultimately increases the uncertainties and lowers quality of each data point. This factor is however, heavily influenced by the remaining limitations: camera-technology and image distortion factors. The maximum amount of data points is equivalent with the fps. The necessary fps depends on the velocity and change in form of the object. To low fps will result in a blurred picture, making it difficult to distinguish the object (the flow front) from the surroundings. This can be solved by increasing fps. However, by increasing fps you will reduce the amount of light the camera can capture in a single frame. This results in a darker representation.

Image distortion can be a result of barrel distortion. Barrel distortion occurs when the travelling object don't follow a perpendicular path to the observing camera. This results in straight lines which curves inwards leading to an increased inaccuracy. This has been resolved by always placing the camera perpendicular to the slide path and only consider velocity in horizontal direction, which can be seen in Figure 4. 5.

4.5.2 Measurements by Sensors

The measurement sensors include pore water pressure, total force, and impact sensors. All sensors were tuned on a sampling rate of 1000Hz ensuring enough mobility to capture true peak and bulk measurements. The full pore pressure dataset including processed data for pore sensor 3 is illustrated in Figure 4. 6.

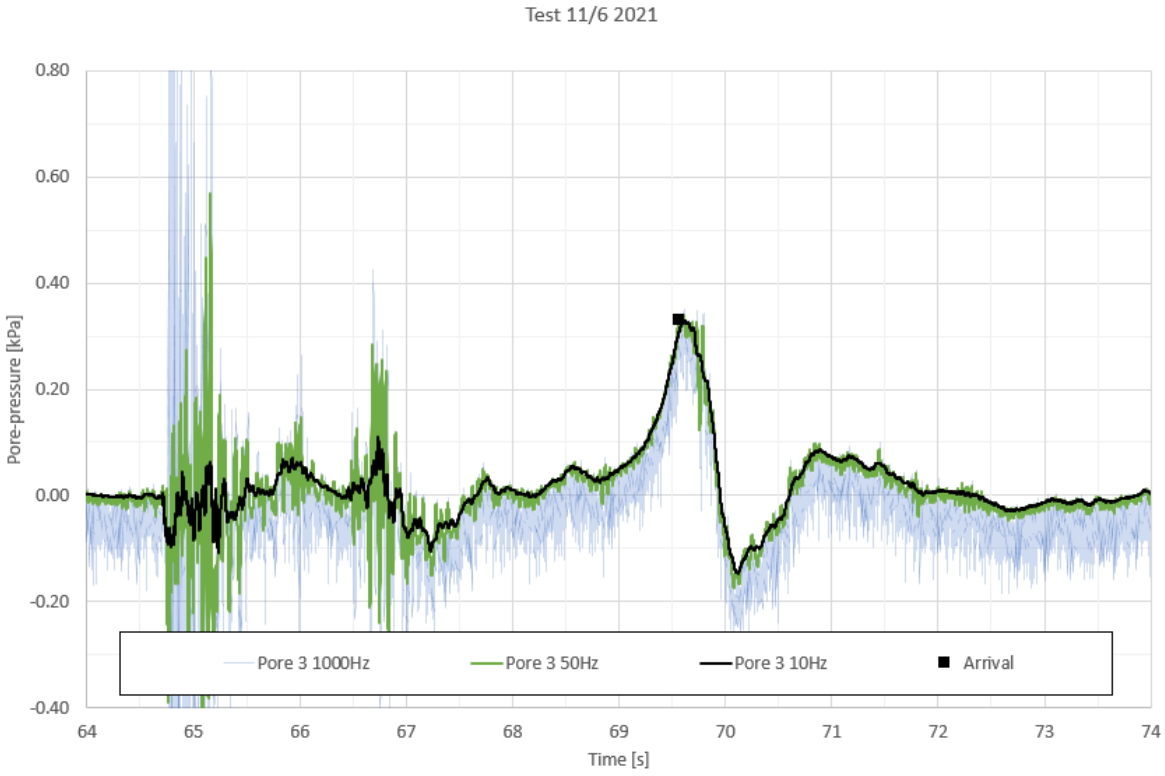

Figure 4. 6: Pore pressure measurements for entire data set (1000Hz), as well as averaged 20 times (50Hz) and 100 times (10Hz). This test represents test 15 in Table 4. 1.

Pore 3 1000Hz is referred to as the full data set including all sampled signals, while *pore 3 50Hz* can be considered as an averaged sampled sequence averaged over 20 data points, finally *Pore 3 10Hz* represents the interpreted dataset based on a running average over 100 data points. The window size data points presented in *Pore 3 10Hz* (black line) represents an upper average which is considered as a best fit parameter to eliminate random effects and maintaining the true peak measurements. The random effects seemed to be based on the resonance frequency and movement of the water tubes. This inference appears in all three graphs (1000Hz, 50 Hz and 10 Hz), but is significantly more dominating for higher frequency ranges, substantiating 10 Hz as the best-fit estimation.

Similar random effects are also found for the total force and Impact force measurements. Figure 4. 7 illustrates the impact force measurements at sampling rate (1000 Hz) and processed data at (50 Hz). A running average over 20 data points seems to neglect these effects and supports the steady state criterion related to 0 force before slide initiation.

Figure 4. 7: Impact force measurements, 1000Hz represents the entire sampling domain and 50Hz represents data processed results. This test represents test 15 in Table 4. 1.

A related threshold frequency can be estimated based on the average slide front velocity and sample size. This can be formulated as:

$$f_{max} > \frac{v_{steady}}{d_{size}} \tag{4.2}$$

where v_{steady} represents the steady state speed at measured location and d_{size} represents the sample length. This assumption is based on a full contact between slide and sensor. Video observations support this assumption. If we consider the slide as a mono-phase flux, then a low pass frequency f_{max} based on the steady state front velocity can be established. Considering model test 15, which has been illustrated in Figure 4. 6 and Figure 4. 7, steady state velocity measure to be $0.64 m/s$. If a d_{size} of 10 cm is considered, a signal of 6.4Hz is measured and a sampling rate of 12.8Hz is necessary according to Nyquist and Shannon. Considering the sampling rate of 1000Hz and post processed rate of 50 Hz and 10 Hz, this could be regarded as appropriate.

5. Results and Discussion

This chapter presents and discusses the results from the conducted model slide tests and supplementary laboratory experiments. To present the results in an orderly manner, the laboratory experiments are addressed first. This includes a presentation and comparison of the investigated soil properties, providing an assessment of the link between kaolin and BF clay. The discussion related to conducted laboratory tests includes Index tests, Viscometer, T-bar and DSScy results, covering the results, limitations, and experimental challenges for each test. The cyclic triaxial tests are presented in Appendix A, as the results are subject with uncertainty and thereby not used in this soil investigation.

The model slide tests constitute the second half of this chapter. This part discusses the different slide events conducted and relating slide behavior observed. The results are quantified through dimensionless numbers, analytical and empirical relations where slide and impact observations are described on the basis of laboratory test results. The instrumentation used to investigate these model slides are presented in chapter 4.3 and consists of pore water pressure sensors, total stress sensors and impact force measurements, and video recordings.

5.1 Laboratory Experiments

5.1.1 Index Tests

Geotechnical parameters established from index tests are summarized in Table 5. 1. The conducted tests are made up by fall cone, water content, Atterberg limit, pycnometer and hydrometer tests. All tests serve a distinct purpose of displaying important material properties which affects both geotechnical and rheological attributes. In total 27 fall cone tests were conducted where 15 of the tests are conducted on unique material states of kaolin and BF clay.

All fall cone tests were completed on the same sample used for either T-bar tests or viscometer tests, resulting in 17 (8 unique) tests on kaolin and 10 (7unique) of BF clay. This procedure provides the opportunity to directly evaluate T-bar and viscometer results in correlation to fall cone tests. Water content was measured only after both fall cone and T-bar/viscometer test. This was considered sufficient according to Adamson (2017) and Grue (2015) studies on viscometer tests, where a deviation of 1.3% was found between water contents before and after testing.

The plastic and liquid limit is assumed identical to related material for all tests conducted in this study. The soil property investigation has been conducted in two separate test programs, where Atterberg limits, grain density, specific gravity and 9 out of 27 fall cone experiments are associated with studies conducted in the preliminary studies related to Hartnik (2021), while remaining fall cone experiments are conducted in relation to the T-bar tests.

Table 5. 1: Summary of index test results of kaolin and BF clay at various water content.

Material	C_{ur}fc [Pa]	w [%]	w_L [%]	w_P [%]	I_P [%]	LI [$-$]	w/w_L [$-$]	ρ_s [g/cm^3]
Kaolin	1701	56	59	31	28	0.89	0.95	2.73
	830	62	59	31	28	1.10	1.05	2.73
	706	65	59	31	28	1.21	1.10	2.73
	151	90	59	31	28	2.1	1.52	2.73
	141	93	59	31	28	2.21	1.58	2.73
	110	100	59	31	28	2.46	1.69	2.73
	106	110	59	31	28	2.82	1.19	2.73
	70	117	59	31	28	3.07	1.98	2.73
BF	2850	85	101	35	66	0.74	0.83	2.74
	2502	91	101	35	66	0.84	0.9	2.74
	1432	100	101	35	66	0.98	0.99	2.74
	814	105	101	35	66	1.06	1.04	2.74
	522	118	101	35	66	1.26	1.16	2.74
	490	119	101	35	66	1.27	1.18	2.74
	223	142	101	35	66	1.62	1.40	2.74

To get an understanding of the strength evolution during different slide phases, an investigation of the soil strength deterioration related to increased water content is considered important. Hence, both kaolin and BF clay were investigated over a sufficient range of water content spanning from water contents of 56%-117% (LI:0.89-3.07) for kaolin and 85%-142% (LI:0.74-1.62) for BF clay.

The added water was de-ionized for all laboratory experiments, ensuring no changes in the properties of the clay. By using de-ionized water, a pH of 7 is maintained resulting in negatively charged faces and positively charged edges for kaolin grains. However, these effects are considered neglectable for most tests, and will have a greater effect on flocculation of the material. Effects of quickness and salinity were not investigated, but studies from Adamson (2017 and Grue (2015) confirms a certain dependency between salinity/quickness and strength deterioration of Tiller and Perniö clay. Such studies would also be appropriate for kaolin and BF clay but are not investigated due to time limitations.

The grain size distribution is presented in Figure 5. 1 and described in chapter 3.4. The distribution of BF clay is extracted from (NGI, 2019a) and presented through 4 points (illustrated in orange). This analysis is based on the falling drop method unlike the kaolin analysis which was found through a hydrometer analysis. Both methods are based on stokes law using the relation between frictional forces of spheres moving in a liquid and the relating diameter and velocity, making both results directly comparable. Figure 5. 1 shows a clay content of 44% for kaolin and 60% for BF clay, defining both materials as clays. According to NGI (2019a) it is observed small variation in grain size for the upper parts of the seabed in Bjørnafjorden. Hence, samples taken and investigated from nearby bore holes can be considered to have similar attributes.

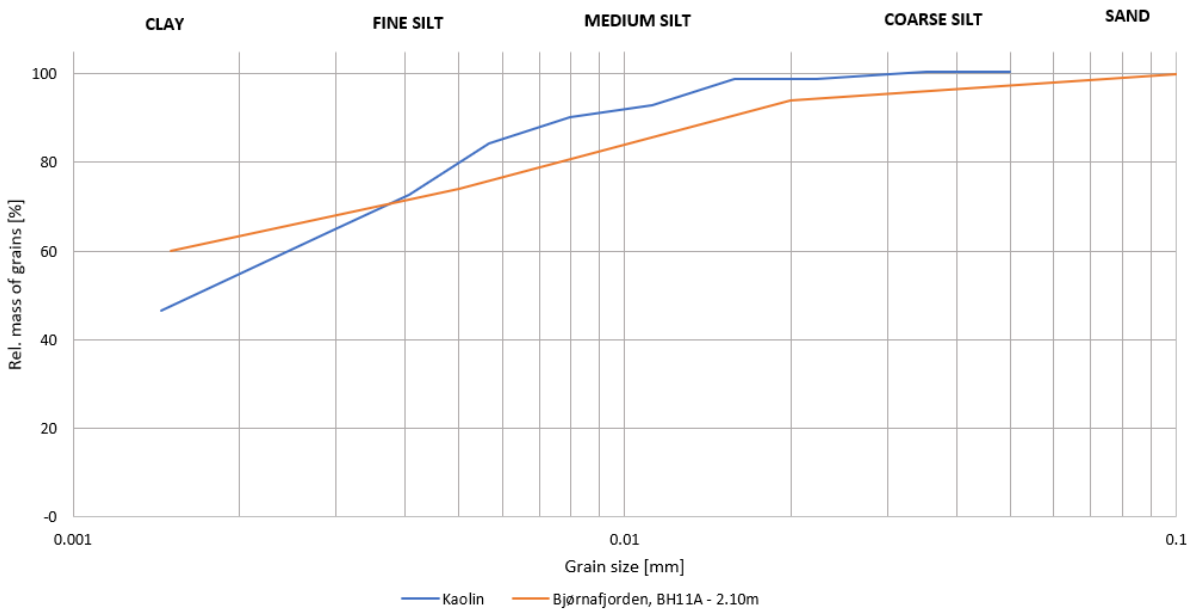

Figure 5. 1: Grain size distribution for kaolin and Bjørnafjorden clay

The remolded fall cone results presented in Table 5. 1 are illustrated in Figure 5. 2. The remolded shear strength from fall cone is presented in relation to water content (a), normalized water content (b) and liquidity index, LI (c). The normalized water content represents a normalization on liquid limit on the form w/w_L, and liquidity index, which is considered as a normalization of the water content in relation to the plastic and liquid limit, makes a good tool for comparing materials with various properties based on change in water content. Normalizing the strength-water content relation on the basis of plastic and liquid properties of clay is commonly accepted (Shimobe & Spagnoli, 2020), where the liquidity index exhibits a strong correlation with fine grained materials such as clay. Based on Figure 5. 2 both normalizations display a good fit for the kaolin clay to BF clay, however for further investigations and comparisons the liquidity index is preferred.

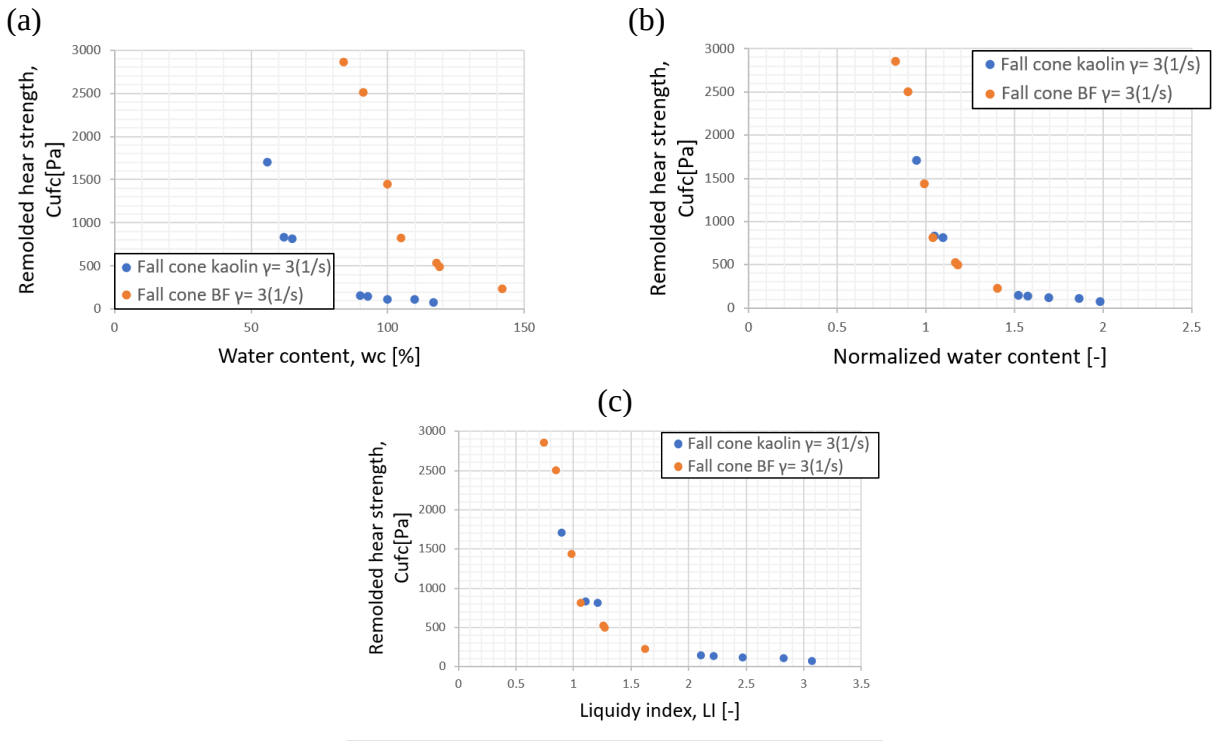

Figure 5. 2: Figure 4. 8 (a-c): Presentation of water content at various remolded shear strengths using different normalizations. Results are based on fall cone tests. (a) relationship between water content and remolded shear strength. (b) relationship between normalized water content and remolded shear strength. Where normalized water (c) relationship between liquidity index and remolded shear strength.

As expected, the strength deterioration related to increased water content proves to be substantial for both kaolin and BF clay. Following Figure 5. 2 (a), both materials tend to follow a similar behavior where BF clay is 40% shifted based on w_c. This shift makes sense when considering the plastic and liquid properties, and through the normalizations both materials seem to exhibit similar behavior.

Limitations of Index tests

Fall cone tests determines the shear strength for small volumes of the soil. This uncertainty is minimized by following *NS 8015* (1988) requiring the deviation of two penetration to be less than 0.5mm. This test further demands homogenous sample assuming correct correlations between penetration, cone, and shear strength. This relationship increases in uncertainty for materials with low shear strengths. For highly viscous materials, such as kaolin and BF clay with LI over 1, similar uncertainties are generated, making it harder to interpreted the true shear strength. The fall cone test should be, due to its simplicity and high uncertainty for viscous materials, considered in context with other tests.

5.1.2 Viscometer Test Results and Limitations

In total 9 viscometer tests were conducted during preliminary studies. Out of these were 4 conducted on BF clay and 5 on kaolin showcasing the rheological behavior for various shear rates. The full capacity of the viscometer apparatus stretched from shear rates between 24 to 1234s^{-1}. However, only 5 out of 9 tests could be measured through this range, the remaining 4 tests induced to high shear stresses. Out of the 5 tests conducted on kaolin, only the 3 most liquid samples could be measured through the full shear rate range. Considering viscometer tests from BF clay, only 2 out of 4 tests were sheared through the full range. The reasons concerning such limitations related to viscometer testing will be considered and discussed in chapter 5.1.5. The viscometer tests will alongside T-bar tests and DSScy form the foundation for evaluating the strain rate dependency of both materials.

Dynamic response

The dynamic response test introduced as a tool to interpret viscometer data, represents an important understanding of the soil behavior and characteristics. The viscometer apparatus measures the rotation speed and relating torque to maintain this speed. This data is further processed and presented as shear stress and shear rate. This conversion is however only applicable when a continuum material behavior over small test dimensions can be presumed. By using this assumption, flow curves can be established from the processed shear strengths at given shear rate. The practicalities and procedure regarding calibration and reaching steady state conditions are described in chapter 3.5. Each test had a measured shear stage lasting 120 second where measurement was conducted after 5, 30, 60 and 120 seconds. Figure 5. 3 gives an illustration of the flow behavior at various rotations speed for kaolin 108% w_c sample, showing only small fluctuations through the whole test-regime.

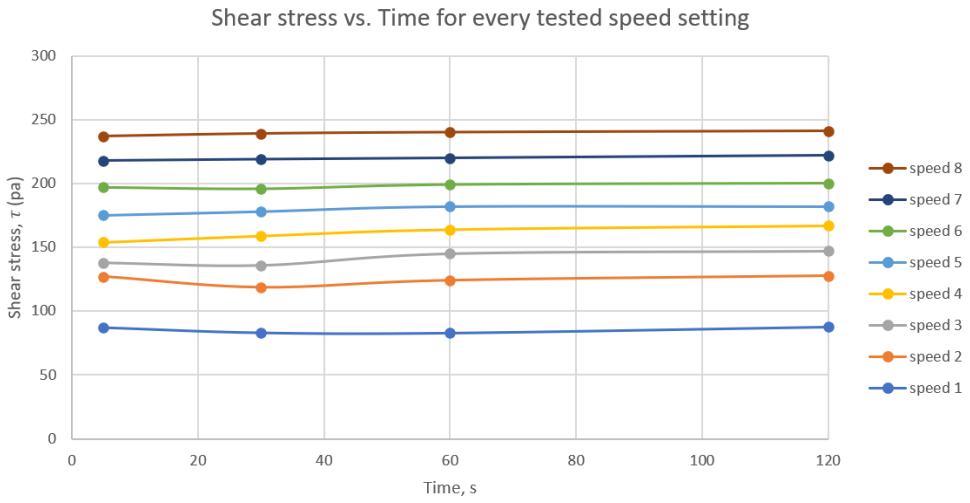

Figure 5. 3: Shear stress measurements at 5, 30, 60 and 120 seconds at various speeds for kaolin with 108% water content.

Figure 5. 4 presents the dynamic response test for the conducted viscometer tests. This data represents 9 different viscometer tests of kaolin and BF clay at various water contents. Measured

data is presented as shear strain rate vs remolded shear strength in (a) and (c), while (b) and (d) illustrates normalizations of (a) and (c). These normalizations are based the initial shear stress, τ_0, measured at lowest shear strain rate, $\dot{\gamma} = 24\ s^{-1}$. The apparatus has a capability to measure stresses up to 1500 Pa, which leaves a limitation on firmer samples. These limitations causes deficient measurements resulting in 4 tests with fewer than 8 measurement points: LI 0.86 kaolin has 3 data points and LI 1.21 kaolin has 7 data points, while BF at 0.83 LI has 1 data point and BF 0.98 LI has 7 data points. The presented data shows shear stresses measurements after 30 seconds for every viscometer test.

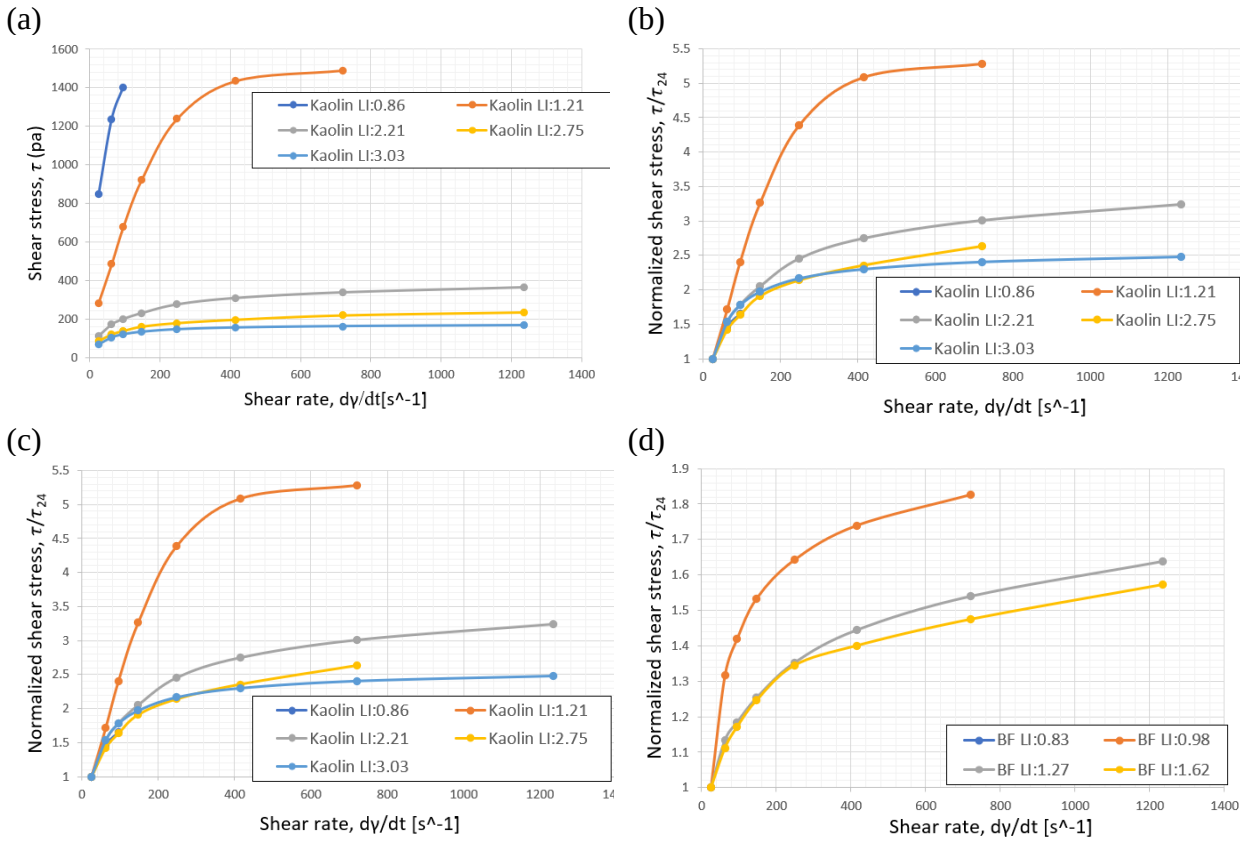

Figure 5. 4 (a-d): Comparison of viscometer flow curves for kaolin and BF clay. (a) *Shear rate vs measured shear stress for kaolin clay. (b) Shear rate vs measured normalized shear stress for kaolin clay. (c) shear strain vs measured shear stress for BF clay. Note that LI 0.83 test consists of only one point. (d) Shear stress vs measured normalized shear stress for BF clay. Note that LI 0.83 test is represented as one point, located at 1.*

Considering Figure 5. 3 two striking patterns can be observed. Firstly, the flow curves related to firmer material states exhibits a more sensitive behavior towards strain rate dependency, compared to more viscous material state. This is particularly evident for kaolin at LI 1.21, and BF clay at LI:0.98. As BF clay at LI:0.83 has one measurement and kaolin at LI:0.86 measures 3 points a lack of measured data can be observed and considered as insufficient to maintain a full understanding of the flow curve and is consequently disregarded when evaluating the soil behavior

based on viscometer tests. Secondly, a change in rate dependency seems to occur around liquid limit for both materials. For samples with water contents exceeding the liquid limit, a decrease in shear rate dependency can be observed. This change in behavior is better captured by the normalization of shear stress, presented in Figure 5. 4 (b) and (d). This normalization captures the rate development based on initial strain rate at given water content, providing a convenient tool for comparing rate development at changing water content. The decrease in flow curve inclination for higher shear rates suggests a shear thinning behavior for both materials, supporting the assumption that fine grained materials exhibit non-Newtonian behavior.

5.1.3 T-bar Test Results

The prime intention of using T-bar experiments was to study the rate effects and strength deterioration of kaolin and BF clay from liquid limit to highly viscous state. 18 testes were carried out, 12 for kaolin and 6 for BF clay, where various strain rates were investigated in both remolded and un-remolded material state. The un-remolded strength (Su) investigation was carried out at the penetration rates of 1mm/s, 3mm/s, 10mm/s, and 30mm/s for kaolin at an approximately LI of 1.1, 2 and 2.5 (wc:60%, 90% and 100%), and penetrations rates of 3 and 30mm/s were carried out on BF clay at LI: 0.75, 1.1 and 1.25 (wc:85%, 110% and 120%). For remolded strength (s_{ur}) investigations, penetration rates of 0.3mm/s and 50mm/s were additionally tested resulting in 6 data points.

The conversion of penetration rate to shear rate, $\dot{\gamma}$, can be established through Finite Element (FE) analysis. By simulating plastic deformation and viscous flow of a fully engulfed cylinder, the flow around mechanism representing a deep failure can be investigated. Figure 5. 5 shows the failure mechanism illustrated as 2 Rankine zones in top and bottom divided by one Prandtl zone in between. These simulations are conducted for very low velocities making the viscous component of soil strength neglectable, and recovering the classical plasticity solution(Martin & Randolph, 2006). By expressing the failure mechanism through a bearing capacity formulation, a constant bearing factor, N_H, can be expressed together with a nominal shear strength based on certain strain rate. The relationship between shear rate and flow velocity of the cylinder can be obtained as follow:

$$\dot{\gamma} \approx f \cdot \frac{v}{D} \tag{5.1}$$

where f represents a conversion factor, determined from Figure 5. 5, v is the penetration velocity and D is the T-bar cylinder diameter which in this case is 4mm.

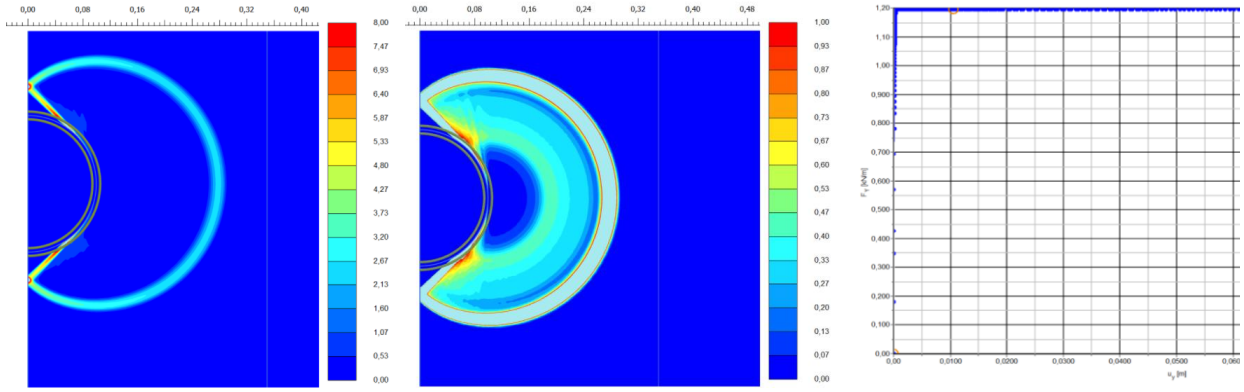

Figure 5. 5 – Deep failure mechanism using Plaxis 2D; D=0.2m, v=0.1m/s, t_{ref}=1s, contours γ_{rate}. The middle figure represents a 8 times inflated version of the left figure. The right hand figure portrays the vertical force for vertical displacement.

From Figure 5. 5 this adjustment factor, f, can be estimated to $f = \frac{\dot{\gamma} \cdot D}{v} = \frac{0.75/s * 0.2m}{0.1m/s}$ =1.5. By assuming rigid strength and perfectly rough pile together with preserving the classical plasticity solution, this approximation correlates well with theoretical upper bound solution by Randolph & Houlsby (1984) for a pile, see Figure 5. 5 (c) where a bearing factor N_H=11.95 is obtained. This approach makes it sufficient to evaluate the impact force by adopting a velocity independent constant bearing factor, which is based on the rigid plasticity solution and operative shear strength at corresponding strain rate established in Eq. 5.1. This conversion results in strain rates equivalent to $\dot{\gamma}(s^{-1})$ = 0.1125 (0.3mm/s), 0.375(1mm/s), 1.1125 (3mm/s), 3.75 (10mm/s), 11.25 (30mm/s) and 18.75 (50mm/s).

Figure 5. 6 (a-d) presents the full T-bar investigation of kaolin sample at LI: 2. This sample was firstly cycled 20 times at a strain rate of 10 mm/s, until remolded state was ensured. Afterwards cycles between 0.3mm/s and 30mm/s were sampled, which is presented later in this section. Figure 5. 6 (a) illustrates the measured penetration force and the corrected penetration resistance, Q_{net}, adjusted for buoyance and shaft friction. (b) illustrates the corrected cyclic shear stress development, with the virgin penetration showed in orange, and the cyclic development as blue. This correction takes the changing bearing factor into account adjusting for the shallow and deep failure effects described in chapter 5.1.5. The shallow failure effects contribute to the initial penetration (in orange), where N_T increases from 3 until it reaches 10.5 and deep failure effects, also known as flow mechanisms, dominates. However, for the remaining cycles, illustrated in blue, the operating depth is below the transition depth, w_{deep}(which is 33.7mm for kaolin LI:2), and a constant bearing factor of 10.5 is appropriate.

Considering (a) it is hard to distinguish the buoyancy effects from the shaft friction, and it is notably how the friction effect increases with depth. The friction is further dependent on the material and material state, which in combination with buoyancy requires a good understanding of the material when measuring and estimating the material strength.

(c) illustrates the shear cycles between 0.3mm/s and 50 mm/s capturing the behavior and stress development for increased penetration rates. For lower penetration rates between 0.3mm/s and 3mm/s we can observe a strange behavior where increased rate causes lower strengths. This can be explained by partial pore water dissipation accelerating consolidation effects increasing the soil strength and penetration resistance, further discussed in chapter 5.1.5.

(d) presents the normalized shear stress for each cycle. This illustrates the strength deterioration or strain softening through each cycle and by using a normalization based on initial τ/τ_{rem}, sensitivity can be found through each cycle. The presented shear stress is extracted from depths between 75mm and 85mm as an average from each cycle. This procedure prevents the influence of conditions at the extreme of the cyclic zone and boundary effects(Lunne, Berre, et al., 2011).

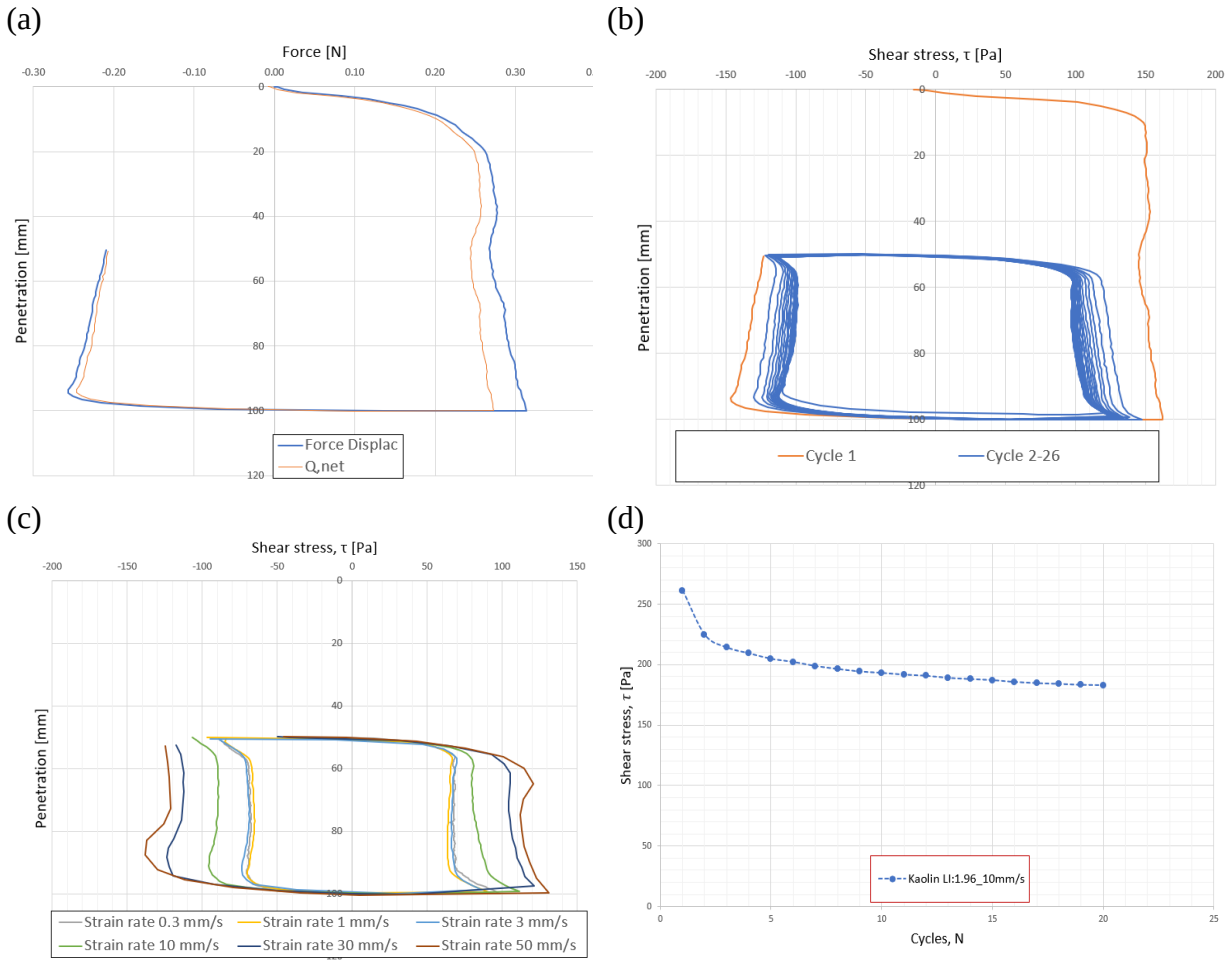

Figure 5. 6(a-d): (a) Shaft friciton and buoyance corrections for the first cycle in force, (b) Cyclic development at 10mm/s penetration rate including the virgin cycle presented in orange. (c) Remolded cycles between 0.3mm/s and 50 mm/s which was conducted for every test after initial penetration rate. (d) Cyclic degradation for each curve based on initial penetration rate. All figures are based on the data processing from T-bar tests for kaolin at LI2 and a remolding penetration rate of 10mm/s.

Strain rate dependency

The remolded strength measurements at strain rates between 0.1125 and 18.75 s^{-1} for kaolin and BF samples at various water contents are presented in Figure 5. 7. The presented tests in (a) are BF clay at 3 different water contents pre-sheared at a penetration rate of 3mm/s, similarly (b) illustrates kaolin tests at 3 water contents pre-sheared at 1mm/s. Figure (c) and (d) compares both kaolin (dashed line) and BF clay at LI~1.1, illustrating the strain rate development. The figures are differentiated based on the pre-shearing velocity and small changes in water content, except this the conditions are identical.

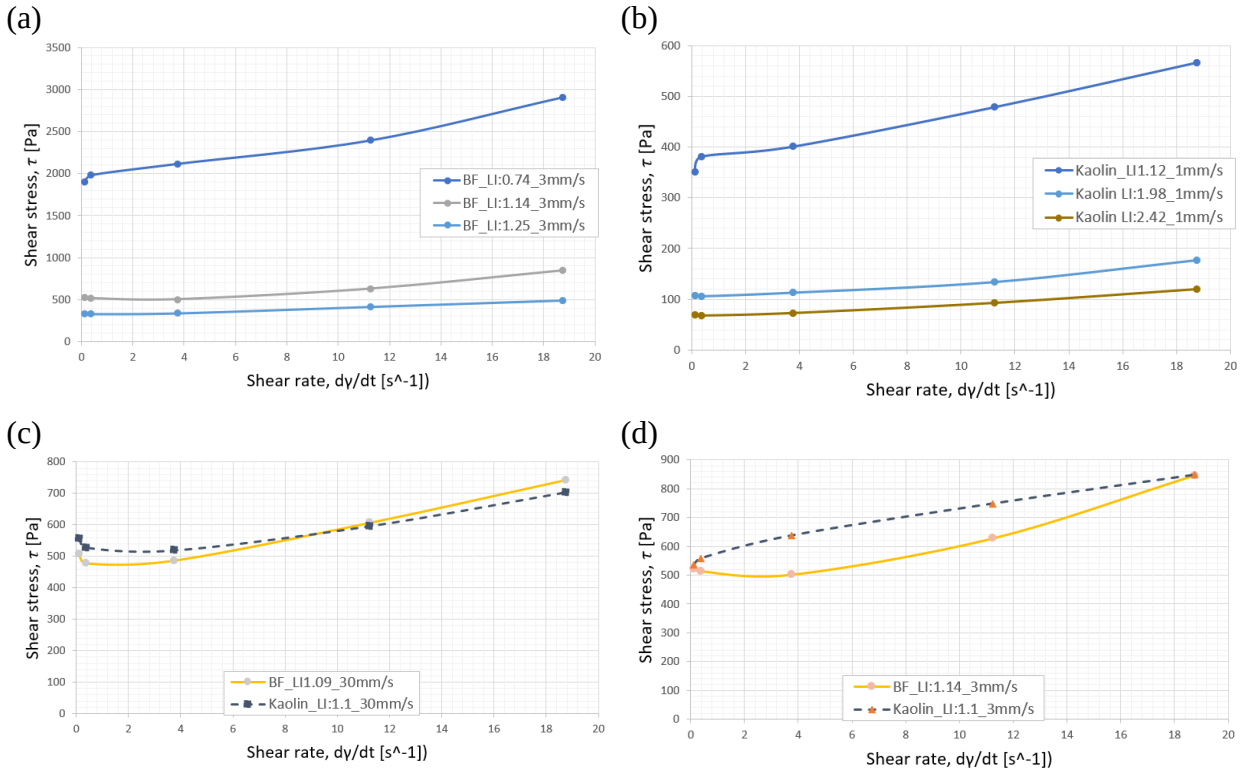

Figure 5. 7(a-d): (a) and (b) shows the strain rate dependency of BF and kaolin clay for strain rates between 0.375-18.75s^{-1} (penetration rates between 0.3 and 50 mm/s). (c) and (d) presents and compares the strain rate dependency for kaolin and BF clay at LI≈1.1 when pre-sheared at 30 and 3 mm/s.

As can be observed from Figure 5. 7 (a) and (b), the data from kaolin and BF clay expresses similar strain rate behavior for the various LI. Note that BF clay is studied for reasonably lower LI than kaolin, and only one of the tests seems directly comparable regarding LI despite containing a notable higher water content (BF LI:1.1=110% vs kaolin LI:1.1 = 62%). This comparison is shown in (c) and (d), with a striking similarity for (c) and some variations in (d). The decrease in shear strength at increasing strain rates below 3.75s^{-1} can partially be justified by drainage effects.

Similarly, the strength deterioration and material sensitivity can be investigated through various strain rates and water contents. Such studies were conducted for strain rates of 0.375, 1.125, 3.75 and 11.25 s^{-1}on kaolin clay, and strain rates of 1.125 and 11.25 s^{-1} were investigated for BF clay.

Figure 5. 8 (a-d) presents the normalized un-remolded and remolded shear strength at the investigated strain rates. This normalization is based on the shear strength at $\dot{\gamma} = 1.125 \rightarrow \tau/\tau_{1.125}$. (a) and (b) shows s_u in black and s_{ur} in red. Only 2 data points is presented for BF clay due to material shortage. For (c) and (d) the $s_u$and s_{ur} for both materials are compared based on the same normalization. Flow curves with similar LI are highlighted by dashed lines, while tests with unconventional behavior is highlighted with a continuous curve.

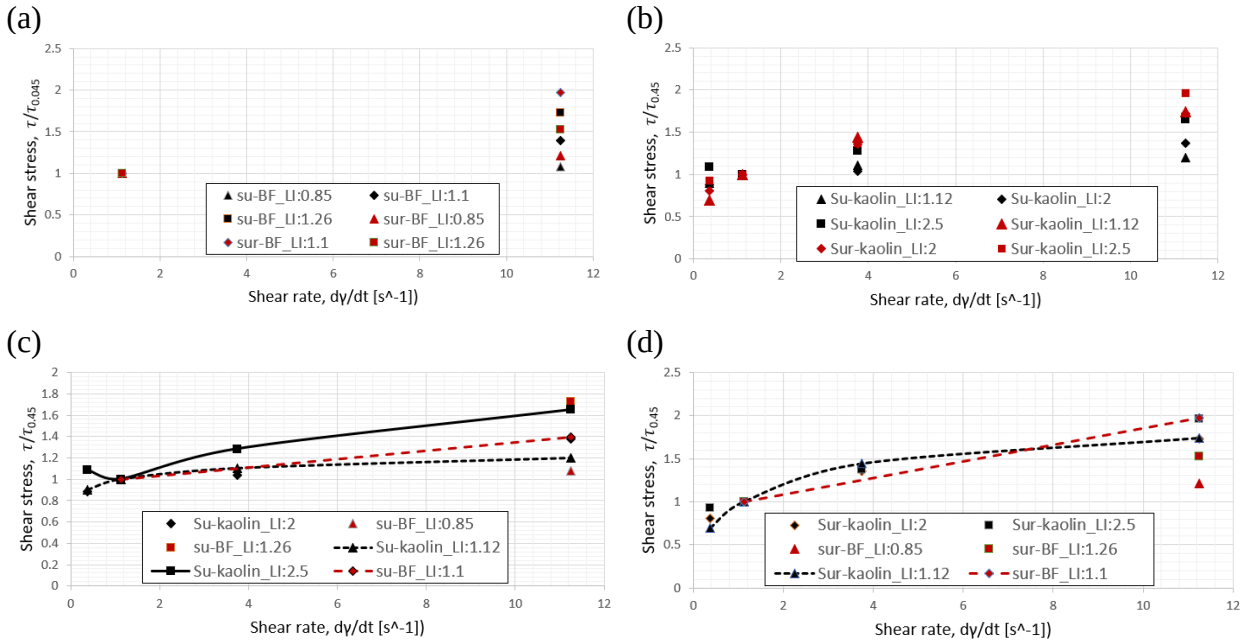

Figure 5. 8 (a-d): The strain rate dependency of unremolded and remolded clay normalized on shear stress at $\dot{\gamma} = 1.125s^{-1}$.(a) and (b) presents and compares the strain rate dependency of Su and Sur for BF in (a) and kaolin in (b). (c) compares the unremolded shear strength related to strain rates, (d) compared the remolded shear strength related to strain rate.

The strain rate dependency in (a) related to s_u vs s_{ur} displays a changing behavior for BF clay. For LI at 0.85 and 1.1, the rate dependency for remolded samples is greater compared to un-remolded samples. For LI 1.25 this behavior is reversed, exhibiting a greater rate dependency for un-remolded samples. This behavior is also captured in (c), showing BF clay with LI 1.25 as the most rate-dependent material. The kaolin clay presented in (b) displays however a changing behavior with increased shear rate. At low shear rates s_u, illustrated in black, tends to exhibit a remarkably high shear stresses at given shear rates below $0.375s^{-1}$, sometimes providing a negative tangent. This is further captured in (c), where this behavior is especially prominent for kaolin LI:2.5.

Considering the drainage effects during low shear rates and the high LI, a greater consolidation effect can contribute towards such a behavior at low rates. At higher shear strains a more prominent behavior seems to be established, highlighting remolded state as more rate dependent than un-remolded. By observing (c) and (d) several patterns can be noticed. Firstly, BF clay tends to exhibit

a greater rate dependency for both remolded and un-remolded state compared to kaolin, illustrated by the dashed lines. Secondly, the rate dependency for increased LI seems generally to be greater for BF clay, especially if the LI range is considered for the two materials.

Cyclic degradation and sensitivity

When considering cyclic T-bar tests, the material degradation during cycling can be considered as important for understanding material behavior through constant remolding. Figure 5. 9 (a) and (b) presents the development of shear strength and sensitivity through each cycle for all conducted kaolin and BF tests. The soil sensitivity is related to the change in penetration resistance at initial penetration and penetration resistance at remolded state. Remolded state is assumed when the change in penetration resistance is 0, which according to Yafrate et al. (2009) can be assessed after 10 cycles.

Considering Figure 5. 9 (d) and Figure 5. 8 (a-d), remolded state is assumed at last cycle for each conducted test. To compare test results from both materials a normalization based on τ/τ_{rem} is introduced, illustrated in Figure 5. 9(c). The normalized cyclic degradation curve displays inherently information related to the soil sensitivity and the rate at which the soil strength decreases (strain softening). Both strain softening and sensitivity are products of geo-mechanical behavior and can be expected to change drastically based on change in LI.

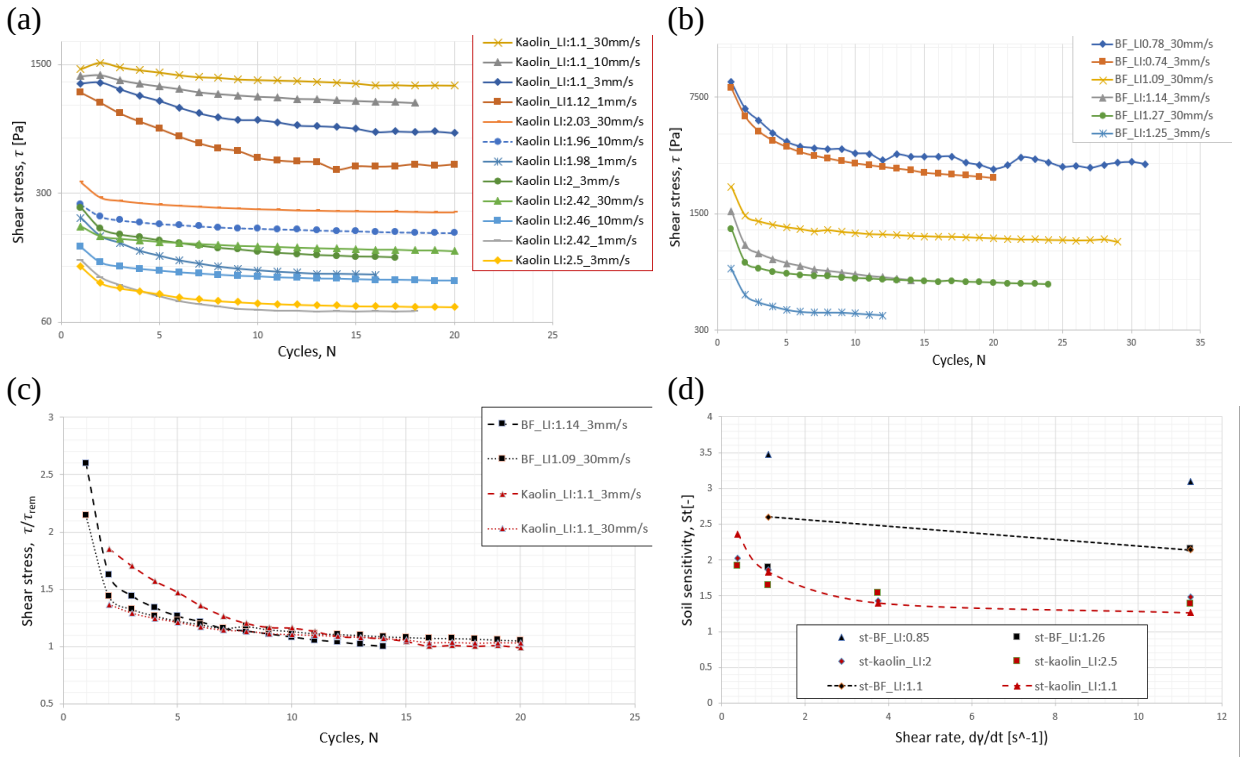

Figure 5. 9 (a-d): Cyclic strength degradation of kaolin (a) and BF clay (b) for in total 12 kaolin and 6 BF T-bar tests. (c) compares the cyclic strength degradation for for LI 1.1 at strain rates of 3 and 30mm/s ($\dot{\gamma} = 1.125$ and 11.25) normalized by the remolded shear strength (τ/τ_{rem}) . (d) presents and compare the resulting soil sensitivity.

The cyclic degradation presented for kaolin in Figure 5. 9(a) and BF clay in (b) exhibits a quite inconsistent behavior for samples with lower LI. Considering kaolin clay, the shear strength for higher penetration rates increases between the first and second cycle before it decreases and follows an expected behavior. One could argue that this is due to the change in bearing factor, however all presented strengths are extracted from depths between 75 and 85mm as an average shear stress ensuring deep failure mechanisms and avoiding extreme values. Although, when handling clay around its liquid limit, the firmness is still considerable. This leaves 2 assumptions. Firstly, handling firm soil complicates the process of ensuring homogenous samples without air pockets. These air pockets can during cycling collapse and be filled with material, increasing the shear strength. For higher water content, the material behaves more viscous making it easier to maintain homogeneity and avoid air pockets. Secondly, for firm clay at a low liquidity state, a full flow between T-bar cylinder and surrounding clay is unlikely to be established due to high velocities and lower viscosity. These effects will first consummate after the first cycle due to remolding.

Considering kaolin samples with LI around 2 or 2.5, an expected strength degradation is displayed. A fully remolded state seems to occur after approximately 10 cycles for most tests, where the cyclic change seems to follow a certain trend for samples with LI 2 and 2.5. The measured strength degradation for BF clay in (b) shows a consistent behavior through all tests. This material seems to be more affected by cyclic degradation insinuating a greater sensitivity towards early cycles. For materials tested with "in situ" water content (LI: 0.78 and 0.74), a fluctuation during remolding occurs. This can be observed for cycle 11-31 for BF_LI:0.78_30mm/s. This behavior can be characterized by inhomogeneity, which might be due to large grains or even gravel, which was also observed in DSScy tests.

Normalized cyclic degradation curve, τ/τ_{rem}, for kaolin and BF clay at LI $\approx$ 1.1 is presented in Figure 5. 9 (c) and highlighted with dashed lines in (d). Notice that the normalized kaolin data in (c) is presented from cycle number 2 due to the inconsistency mentioned earlier. From (c) it is evident that the strength degradation between cycle 1 and 2 for BF clay stands for 60-70% of the total strength degradation. For kaolin it is hard to conclude the behavior of an initial penetration. However, by studying (a) and (b) for higher LI, a similar strength degradation from cycle 1 to 2 between kaolin and BF clay can be observed.

The soil sensitivity is presented as a direct result from (c) in (d) as data points. This illustrates how the sensitivity varies with changing strain rate. BF clay is here represented through only 2 data points: $\dot{\gamma} = 1.125\ and\ 11.25$ due to causes discussed before, while kaolin is presented through 4 data points: $\dot{\gamma} = 0.375, 1.125, 3.75\ and\ 11.25$. Considering the rate behavior through the whole test interval, both materials exhibit similar behavior. It is evident that the sensitivity decreases with increased strain rate. The dependency seems to be greater at lower strain rates for kaolin, especially below $1.25s^{-1}$. For this shear interval no data points are retrieved for BF clay.

5.1.4 Cyclic DSS Results

In total 6 strain controlled undrained DSScy tests were performed on consolidated kaolin and BF samples (see Table 5. 2). Each specimen was subjected to at least 30 cycle of sinusoidal strain cycles. Figure 5. 10 (a-d) illustrates some of the investigated material behavior for $DSS_{BF3.3.3}$. (a) shows the cyclic peak axial strain of 18% applied at $f = 4 \cdot 10^{-4}\ Hz$, while (b) presents the exponential decay of shear stress or strength degradation with increasing N. This can, like the strength degradation from T-bar, capture the soil deformation until remolded state is acquired. As the strength degradation and remolding increases, the excess pore water pressure (PWP) increases. (c) portrays this development as it approaches the consolidation stress, σ_c, or the excess PWP ratio (r_u) as it approaches 1 ($r_u = u_p/\sigma_c$), during cyclic loading. (d) illustrates the effective stress path (ESP) defined by the Critical state lines (CSL). As the pore water pressure accumulates with each cycle, the ESP decays and follows the CSL lines. The ESP for this sample exhibits a more dilatant behavior on negative horizontal strain compared to positive strains. This seems however to be within reasonable range. Remaining ESP results are presented in Appendix B. These exhibit highly questionable behavior with dilatant and contracting reactions dominating the σ_v-τ space, not necessarily relatable to the CSL lines. Hence, the ESP is not considered in further analysis.

Table 5. 2: DSScy properties summarized

Parameter	*Kaolin Clay*			*BF Clay*		
Test id	$DSS_{K1.1.1}$	$DSS_{K2.2.2}$	$DSS_{K3.3.3}$	$DSS_{BF1.1.1}$	$DSS_{BF2.2.2}$	$DSS_{BF3.3.3}$
Water content (%)	59.2	52.1	50.8	48.9	48.8	48.7
Liquidity Index, LI $(-)$	1.0	0.75	0.7	0.21	0.21	0.21
Strain rate (s^{-1})	0.6	0.012	$2.5 \cdot 10^{-4}$	0.6	0.012	$2.5 \cdot 10^{-4}$
Unremolded shear strength, S_u (kPa)	9.52	7.86	7.84	19.61	15.32	9.76
Remolded shear strength, S_{ur} (kPa)	2.2	1.13	1.1	3.02	1.82	1.17
Sensitivity, S_t (kPa)	4.3	6.9	7.1	6.5	8.4	8.4
Excess PWP first cycle, r_u $(-)$	0.63	0.71	0.83	0.7	0.78	0.78
Excess PWP last cycle, r_u $(-)$	0.87	0.95	0.92	0.87	0.96	0.94

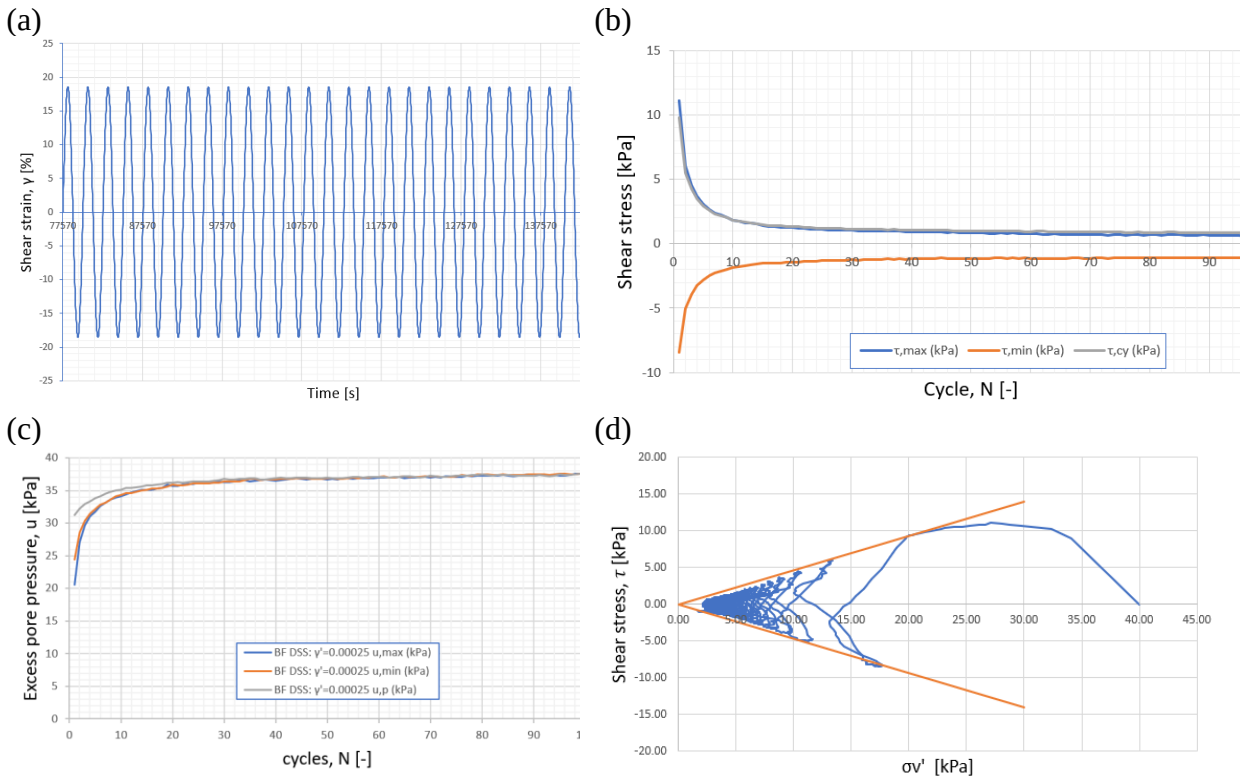

Figure 5. 10(a-d): presentations of typical plots from$DSS_{BF3.3.3}$. (a) presents the cyclic shear strain vs time, (b) presents the cyclic degradation of shear strength, (c) show the resulting cyclic pore pressure accumulation. (d) shows the effective stress path in a critical state format.

The cyclic variation of deviator (shear) stress with shear strain is illustrated in Figure 5. 11 for $DSS_{BF3.3.3}$. Here, (a) presents the unprocessed data affected by membrane stiffness, while (b) presents membrane corrected results. The corrected results are processed on the assumption of a fully remolded sample when 30 cycles are reached. Hence, there is an anticipation that the tangent stiffness approaches 0. Such corrections are conducted on all tests based on the same assumption, which can be found in Appendix B.

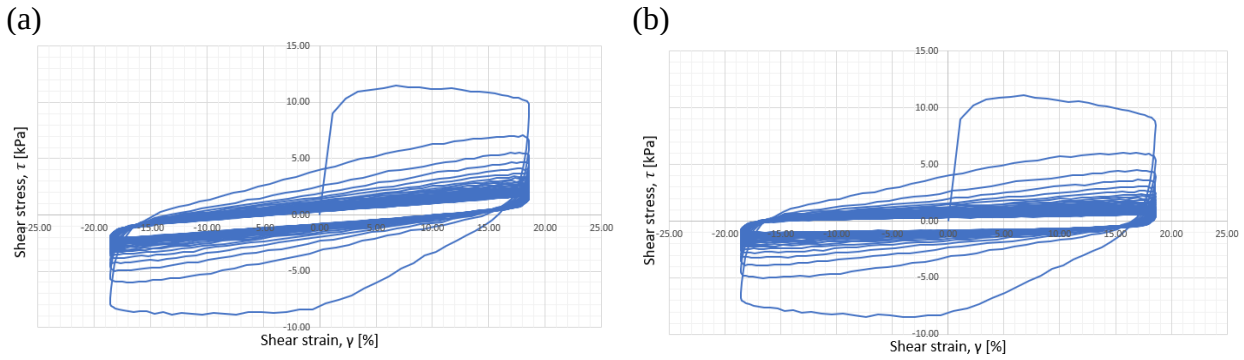

Figure 5. 11(a-b): presents unprocessed and processed hystersis loops of $DSS_{BF3.3.3}$.

The shear stress – shear strain response from Figure 5. 11 exhibits the typical hysteresis loops. The repeated cyclic shearing imposed on the sample generates excess pore pressure resulting in a decrease in effective stress, as can be seen in both Figure 5. 10 (c) and (d). This is accompanied by a loss in stiffness when the soil structure is sheared, which further leads to a progressive development of shear strains.

The cyclic shear stress degradation and relating pore pressure accumulation is presented in Figure 5. 12. Kaolin is presented in red and BF clay in black, while the various strain rates are identified through different dashed lines. Note that the cyclic shear stress is presented through a logarithmic scale unlike the excess PWP. By categorizing samples into defined strain rates, a clear trend can be identified between the evolution of cyclic shear strength and excess pore pressure. As the soil approaches remolded state, the excess PWP approaches the consolidation stress. This can be observed for both materials, where they for all strain rates exhibit relating behavior with the approximately 30 cycles to a fully remolded state in (a). Note that a logarithmic scale will highlight small changes at lower values.

Like the T-bar tests, we see a rapid change for the first cycles before it stabilizes and approaches a remolded stage. However, due to the low strengths and rapid shearing, it is hard to determine if a residual stress was established. Åhnberg & Larsson (2012) studied such behavior and differentiated between highly sensitive clay which approached a residual rather rapidly and more silty clay following a gradual decay of strength degradation which could continue over 100-1000 cycles. The cyclic degradation curves of $DSS_{K1.1.1}, DSS_{K3.3.3}, DSS_{BF1.1.1}$ and $DSS_{BF3.3.3}$ follow each other closely compared to $DSS_{K2.2.2}$ and $DSS_{BF2.2.2}$, where BF clay exhibits 1.5 times the remolded shear strength compared to kaolin. Considering the excess PWP, all tests show a pore accumulation approaching $r_u = 1$ where the lowest is measured for $DSS_{K1.1.1}$ and the highest is for $DSS_{BF2.2.2}$

(a)

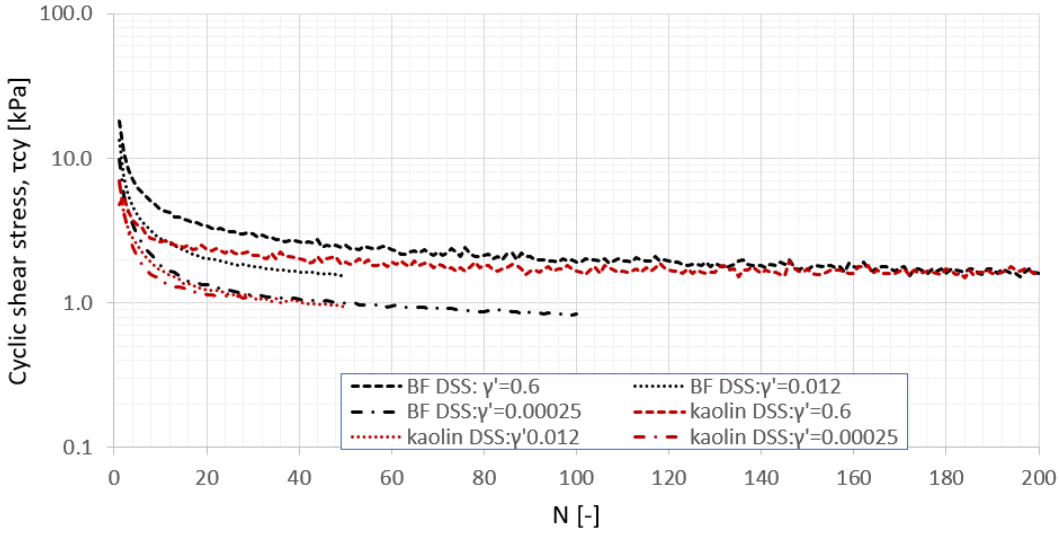

(b)

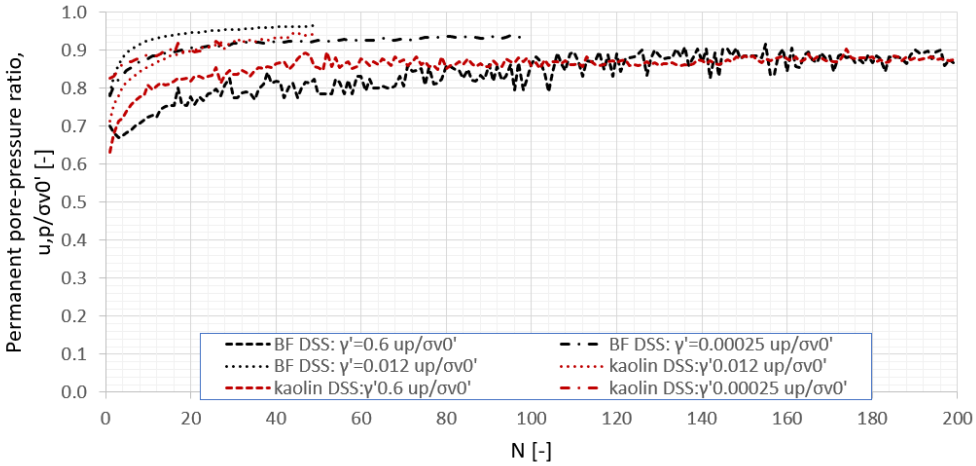

Figure 5. 12(a-b): (a) shows a schematic illustration of the cyclic strength degradatiom from DSScy results, (b) illustrates the corrosponding pore water pressure accumulation for each cycle.

Figure 5. 13 (a) and (b) sums up, together with Figure 5. 12 (a) and (b), the DSScy investigation related to strain rate dependency. The shear strength and remolded shear strength related to strain rate is presented in Figure 5. 13 (a) and (b), while the resulting sensitivity is presented in (c) (also found in Table 5. 2). The cyclic periods conducted in this study stretches from 1s, 50s and 2500s, ensuring a great span for the investigated rate effects. Kaolin, represented in red (Figure 5. 13), exhibits a low rate-dependency with an approximately 0 change between the two lowest shear rates, and a close to 2 kPa change from strain rates between $DSS_{K1.1.1}$ and $DSS_{K2.2.2}$ for un-remolded state. The BF clay on the other hand, illustrated in black (Figure 5. 13), follows a linear trend doubling the initial shear strength of the slowest sample. This high rate-dependency can also be observed for the remolded shear strength, where the strength triples for the BF clay. Kaolin on the other hand exhibits a change in behavior, where it for strain rates below $0.012s^{-1}$ stays constant before the two slowest tests and increases drastically for fastest test. This behavior from kaolin is

expected and widely discussed in literature (Quinn & Brown, 2011; Wichtmann & Triantafyllidis, 2018), however, it is noteworthy to consider the effects of the large variation in water content for kaolin.

Considering the strain rate dependency results from T-bar test, presented in Figure 5. 8 (b), it is prominent that kaolin radiates a larger relative rate dependency for increased LI (when drainage effects are eliminated). However, with increased water content the remolded shear strength also reduces. Hence, it is important to acknowledge the uncertainties related to the large difference in water content in kaolin at lowest shear rates. (c) can be illustrated as a response of (a) and (b), presenting the soil sensitivity based on the DSScy tests. This requires a fully remolded state, which can be assumed based on Figure 5. 12 (a). The sensitivity based on increased strain rate exhibits similar behavior for both materials. For lower shear rates, the sensitivity is approximate 8 and 7 for Bf and kaolin clay, classifying both as low sensitive clays(*NS-EN ISO 17892-4*, 2016).

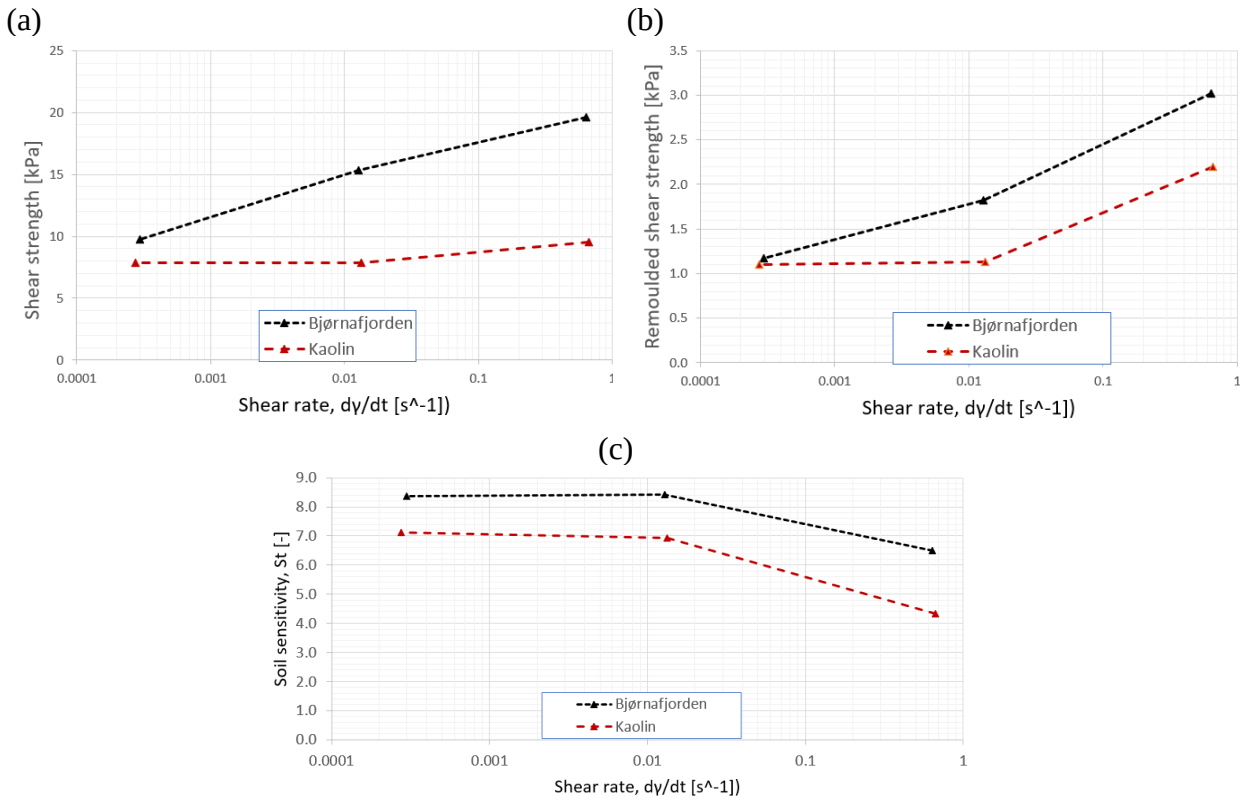

Figure 5. 13(a-c): (a) and (b) illustrates the unremolded and remolded shear strength related to shear rate for conducted DSScy tests. (c) shows the corresponding sensitivity for kaolin and BF clay.

5.1.5 Limitations and Observed Errors of Laboratory Tests

When studying the material behavior over a wide range of material states using different test equipment, recognizing the limitations and testing mechanisms related to each test procedure is crucial. For this study, extremely soft clay with very low shear strengths has been investigated. Such fine measurements require very precises apparatuses. However, the strengths measured are often below what the apparatus can measure with low uncertainties. Hence, data processing and data quality assessment has been important in current laboratory study. In total, results from 9 viscometer, 27 fall cone, 18 T-bar, 6 DSScy and 6 cyclic triaxial tests composes the basis of the understanding of the material behavior related to the strength evolution of a material in a submarine environment.

Figure 5. 14 illustrates the change in material response measured in the T-bar, viscometer and fall cone for kaolin with $w_c \approx 88\ and$ 93% or LI≈2 and 2.2. The operative strain rate for fall cone tests is typically $3s^{-1}$(Boukpeti et al., 2012; Koumoto & Houlsby, 2001) which in this study is used to represent a link between the various tests. Considering the material response from conducted T-bar, viscometer and fall cone, a difference between T-bar and viscometer can be observed. The T-bar exhibits a change in behavior after $\dot{\gamma} = 2.5s^{-1}$ unlike the viscometer results, which displays a continuous behavior with increasing shear rates. Judging the results based on fall cone tests, it seems that the viscometer continuously measures lower strengths with increasing shear rates, while the strength evolution of T-bar seems to display an unrelated strain rate dependency at strain rates below $1s^{-1}$. Such behavior from T-bar and viscometer can be partially influenced by the test setup, however, it is likely that other effects related to measurements restraints and material states also contributes.

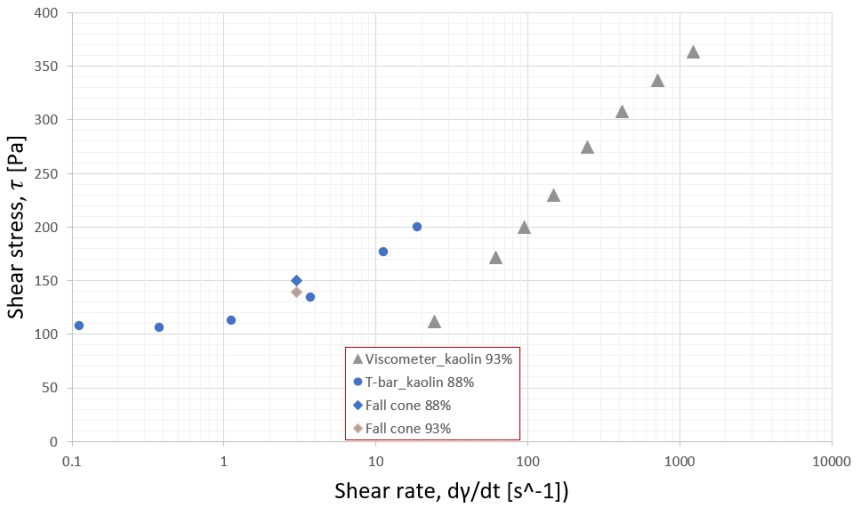

Figure 5. 14: shear stress vs shear rate for Cyclic T-bar, viscometer and corresponding fall cone results for kaolin at LI 2(88% wc) and 2.2(93% wc).

T-bar

Investigating strain rate dependency through the T-bar test can, according to Nanda et al. (2017), be studied under 2 phases. Namely through partial drainage and fully undrained conditions. Lunne et al. (2011) focused on theoretical and empirical studies interpretation of offshore in-situ testing, which included T-bar tests. He reported a variation of penetration resistance in soils exposed to changing shear rates. Figure 5. 15 illustrates his findings and shows that during slow penetration rates, a partial pore water dissipation occurs, leading to a subsequent consolidation resulting in an increased soil strength and penetration resistance. By increasing the penetration rate from a slow rate, a moderate decrease in penetration resistance can be observed as it approaches fully undrained conditions. When increasing the penetration rate further, a change in penetration resistances is caused due to strain rate effects (Nanda et al., 2017). To overcome the drainage effects, a dimensionless speed parameter V is introduced. This constant relates to the penetration velocity, v, the penetrometer diameter, d, and coefficient of consolidation, c_v, related to investigated soil.

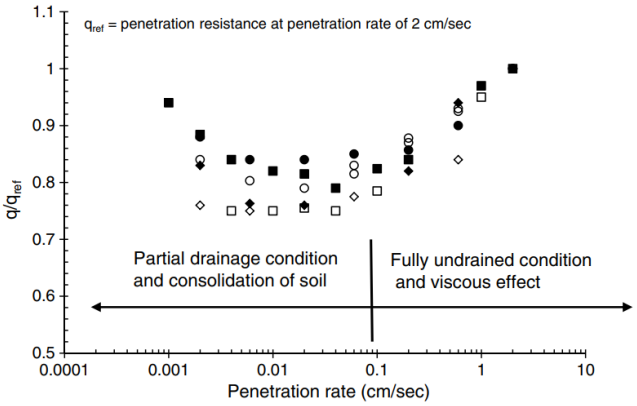

Figure 5. 15: Effect of T-bar penetration rates and relating penetration resistance (Lunne et al., 2011).

$$V = \frac{vd}{c_v} \tag{5.2}$$

Nanda et al. (2017) reports that for a V greater than 20, fully undrained conditions can be assumed. The c_v can be approximated to be $30m^2/year$ for kaolin (Thanh Duong & Van Hao, 2020), and with a penetrometer diameter of 4mm, a penetration velocity of approximately 5mm/s ($\dot{\gamma} \approx 1.8s^{-1}$) is necessary to overcome effects of drainage. This agrees well with the findings presented in Figure 5. 14.

Viscometer

The viscometer is a highly sensitive apparatus able to measure very high strain rates on highly viscous materials. Measuring the plastic deformation and rate dependency of viscous materials requires certain assumptions where limitations and potential sources of error can follow. By evaluating results and challenges regarding implementation alongside literature, several factors stand out. These factors were investigated in preliminary studies and can be summarized in to following contributing elements.

Unstable measurements at higher remolded shear strength and decreasing water content

A key assumption when using viscometer is the premise of a decreasing velocity gradient in the viscometer cylinder, which has its maximum at its rotating spindle and zero at the stationary boundary, as illustrated in Figure 2. 3. Shear banding is a phenomenon that inflicts a significantly lower shear stress or torque, due to counteractions from this principle. This phenomenon is illustrated in Figure 5. 16, and causes only parts of the test sample to shear. This is typical for materials with higher shear stresses and low liquidity indices. Due to the small gap between rotor and outer cylinder, this effect is likely to have minor influence.

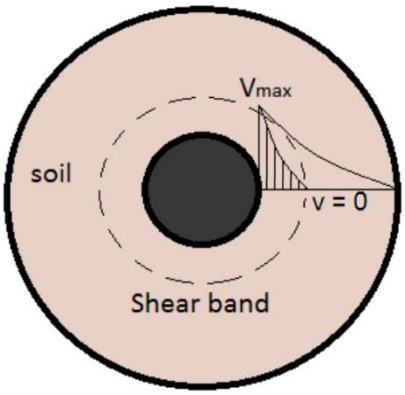

Figure 5. 16 Shear banding, represented by slippage in the clay.

Establishing steady state conditions

Establishing steady state conditions requires reaching the residual stress-point of the material. This can be achieved by cycling the clay through available speed levels of the viscometer, a procedure which exposes the sample for temperature changes and dehydration. Having two processes affecting the viscosity in opposite ways complicates things further. The sample size represents an important indicator for dehydration, and by using small samples this element can be highly influential. Regarding temperature, this element can be monitored on the apparatus making it possible to find which effect this has when determining steady state conditions. For tests with high water contents ($I_L > 1$) the risk of establishing a water membrane between the soil and boundary increases. This will provide an artificially low torque for given shear rate and defy the principle of *no slippage* and *strain rate dependency*. This phenomenon can be especially prominent for tests which are conducted over a longer period. As a consequence, the procedure for estimating steady state conditions becomes also a time dependent procedure. To prevent this, one could fit an isolating fitting for the cylinder. This will avoid dehydration and make temperature control somewhat achievable, which can contribute to counteracting these effects.

Slippage

Slippage can be seen as a central challenge which can occur depending on several factors (water membrane, inhomogeneous materials, too firm material etc.). The effect this event can have varies with shear rate, material properties and even surface roughness in the rotor and cylinder. However, regarding conducted tests, the largest margin of errors occurs probably for lower shear rate, especially for kaolin and BF with high shear strengths. These tests exhibit a different material behavior, which can be highly influenced by slippage often caused by shear banding or no

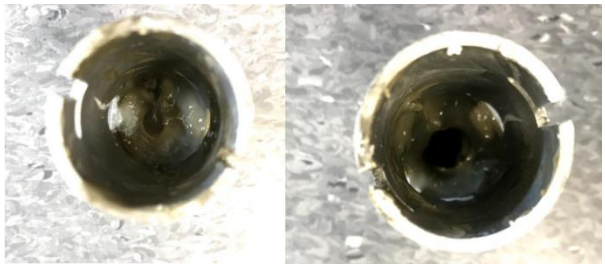

Figure 5. 17: Situation after conducted test. The lefside represents high water content (142%), the right side consists of lower water content (91%) represented by BF clay.

friction between rotor and soil sample. This kind of behavior can often be recognized by large variations in the collected data, Figure 5. 17 gives a physical observation of this. This may also have contributed give the apparatus artificially low readings.

Instrument limitations

Instrument limitations of viscometer tests considers several aspects of the rheological behavior. Primarily, the maximum torque range of 10 mNm (1500 pa) puts an upper limit for the tested material strength. This can be seen for several of the "strongest" materials in Figure 5. 4. When operating at the limit of what the apparatus can perform, some of the data can fluctuate. This may be due to a combination of a material which is in the distinction of remolded and fluid phase (water content close to liquid limit), or by slippage. Further, complications regarding grain size can occur for small gap tests. For small gaps, which concerns presented tests, small grain diameters are required. This is to maintain a homogenous behavior of the sample and preserve the principle of decreasing velocity gradient. This problem can occur at any liquidy index and by considering the grain size distribution in Figure 5. 1, it can be seen to be more severe regarding BF clay. Both materials contain large amount of very small grains (clay), but BF seem to also hold a small amount of coarser grains. Evaluating the results and observations during implementations, this problem seems to be neglectable.

Temperature

The viscosity of fine grained soils are according to literature and studies performed by Adamson (2017), highly temperature dependent (illustrated in Figure 5. 18). As a result of friction between grains on a micro level, the temperature changed depending on the velocity. Higher velocities exhibited higher temperature and vice versa. This phenomenon seemed to amplify for tests with high water content, especially for BF clay, where the margins changed from fluctuations of $\pm$ 1 $C°$ to $\pm$ 3 $C°$. However, it can be assumed some margin of error on the temperature measurements taken from the apparatus, due to material consistency.

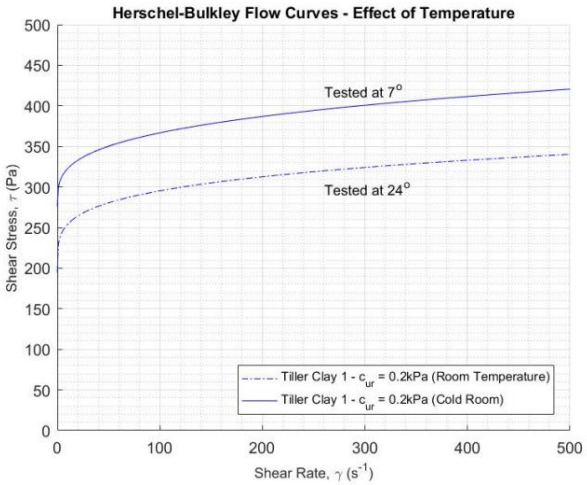

Figure 5. 18: Effect of temperature on Herschel-Bulkley flow curves from studies performed by Adamson (2017).

DSScy and cyclic triaxial tests

Figure 5. 19: Picture of conducted membrane stiffness in extension.

DSScy and cyclic triaxial tests can be considered as advanced soil tests. Such devices have existed since the early 1950s and used to measure the shear strength characteristics of a soil. In order to investigate soil samples in "in-situ" environment, a rubber membrane encloses the sample from the surroundings, ensuring no change in surface area for DSScy and for triaxial tests it isolates the sample from the triaxial cell. As elaborated in chapter 3.7.2, by applicating a rubber membrane to the soil sample, a substantial increase in apparent strength due to the inherent membrane stiffness can be measured. When evaluating the soil strength of extremely soft clays with an LI around 1 and an undrained shear strength of 7 kPa and remolded shear strength of 1 kPa, such membrane effects can become dominant.

Figure 5. 20 illustrates the results of the membrane stiffness in extension established through the T-bar test. The test set up in extension is presented in Figure 5. 19, and is based on a 0.3mm triaxial membrane. This investigation should only be considered as a way of quantifying the membrane stiffness, and not as a result relating to the membrane stiffness. This can be explained by evaluating the subjected strain area at the T-bar which is not uniform and representative for a triaxial test.

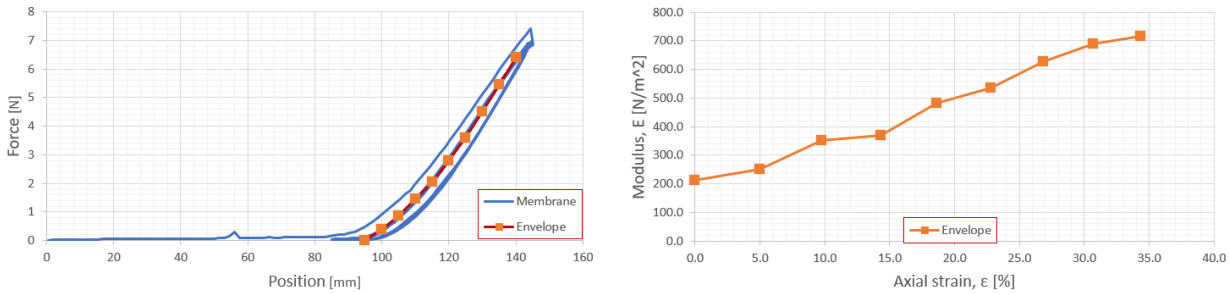

Figure 5. 20: The measure force and resulting membrane stiffness as illustrated in Figure 5. 19.

Through implementation of Eq. 3.2 and 3.3 from chapter 3.7.2 will according to *NS-EN ISO 17892-9* (2018) correct for the induced membrane strength in triaxial tests. However, as the membrane stiffness becomes a significantly part of the measured strength, increases the uncertainties and the non-linear effects of the membrane.

Regarding DSScy tests, there are no conventional method to do membrane corrections. Hence, the data has been adapted based on corrections made by NGI and engineering judgement, as presented in Figure 5. 11. Any buckling effects due to hoop tension or effects from the membrane behaving as a reinforced compression shell has not been observed.

5.1.6 Best Fit Herschel-Bulkley Parameters and Data Processing

The best fit Herschel Bulkley model represents a curve fitting model for non-Newtonian fluids which can be used as a framework for comparing certain soil characteristics independent of test

method. The Herschel Bulkley model is identified through 3 parameters resembling the soil behavior for shear thinning fluids. These parameters were introduced in 2.5.3 and formulates the expression:

$$\tau = \tau_y + K\dot{\gamma}^n \tag{5.3}$$

The yield stress, τ_y, consistency parameter, K, and the Herschel Bulkley exponent, n, constitutes the 3 model parameters describing the approximated rheological behavior of a soil related to strain rate.

Yield stress, τ_y

The yield stress defines the minimum shear stress applied to a material in order to create plastic deformations or flow. This means that for applied shear stresses below yield stress, the material will ideally be considered as a solid. The reality or existence of yield stress as a material parameter has long been discussed, leading to the famous quote: "*whether yield stress is or is not an engineering reality depends on what problem we are considering, not on how long a ball appears to stand still"*(Astarita, 1990). The reality of yield stress as a strength property in soil dynamics is, however, widely acknowledged(Mayne, 2013). Regarding fine grained fluids, stresses induced below the apparent yield stress will only inflict elastic deformations without forcing the material to flow or deform plastic. Hence, the yield stress can, for applications of fluids and fine-grained materials, be understood as a material property describing the change from elastic to plastic behavior or startup flow for complex materials. These inherent material properties of flow was by Saasen & Ytrehus (2019) examined by studying the correlation and application of Herschel Bulkley model towards drilling fluids. He reported a yield stress dependency towards material composition parameters such as solid fractions, grain size and surface-active chemicals, Rehman et al. (2018) identified further a dependency towards plasticity and water content of soils. Such discoveries fit well with the observed data from viscometer, T-bar and DSScy tests. Summarized, one could argue that the yield stress depends on the material composition related to water content, solid fractions, cohesive properties, and material structure regarding surface active minerals of clay.

Determining the yield stress of fine-grained soils can be achieved several ways. The Herschel Berkley yield stress found through extrapolated flow curves is defined based on an algebraic function. This can in some cases display negative values for the yield stress exhibiting non-physical behavior due to its mathematical approach. To establish a predictable procedure to capture the estimated yield stress, presenting the yield stress as a function of shear strength measured by fall cone or T-bar can be used as an alternative. Based on retrieved results and the formulation of shear strength based on T-bar, following formulation can be expressed:

$$\tau_{y,T-bar} = Su_{T-bar} \cdot \frac{1}{5} \tag{5.4}$$

where T-bar is used to represent the yield stress obtained from un-remolded experiments. For fall cone only remolded material is considered which can be expressed as:

$$\tau_{y,fall\ cone} = s_{ur,fall\ cone} \cdot \frac{1}{5} = \frac{KQ}{h^2} \cdot \frac{1}{5} \tag{5.5}$$

where h is the penetration depth, Q is the cone force (N) and K is the correlation factor, $K = 0.27$ based on empirical correlations (Koumoto & Houlsby, 2001). Notice that this serves as an estimation with the intention of capturing the evolution of yield stress with increased water content.

Consistency factor, K, and Herschel Bulkley curvature exponent, n

The relation between the consistency factor, K, and the curvature exponent, n, proves to be highly dependent due to the algebraic form of the Herschel Bulkley expression. Figure 5. 21 illustrates how variations of K and n can result in nearly identical flow curves. Thus, one could argue that these expressions could be expressed as functions of each other, for instance $K = K(n)$. This dependency makes the consistency parameter impossible to determine solely through direct material measurements, making them curve fitting parameters identified through algebraic operations. Consequently, both parameters are required to describe the physical dependencies of a material, making an evaluation of K without assessing n pointless.

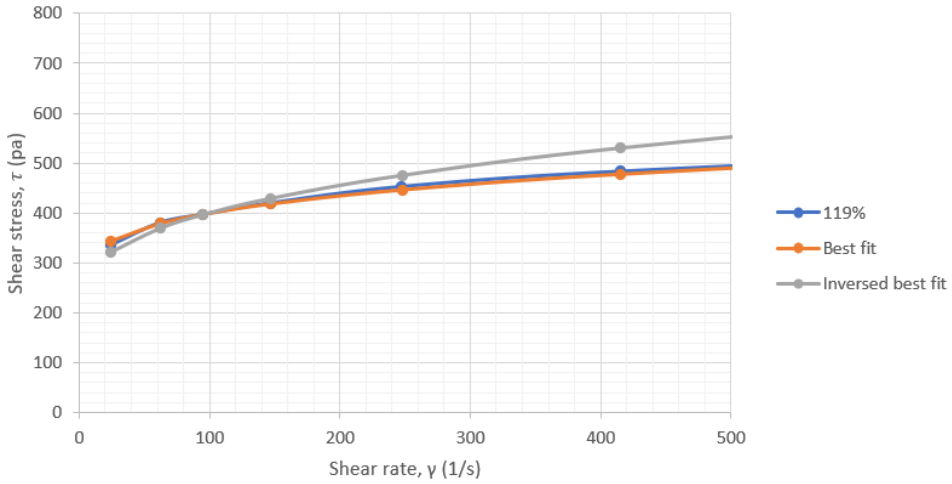

Figure 5. 21: The viscosity flow curve of BF clay at 119% water content presented with two best fit curves expressed with identical yield stress but different K and n values. These curves illustrate how different combinations of K and n can exhibit similar Herschel-Bulkley flow curves for certain ranges. Values are presented in Table 5. 3.

Table 5. 3: Herschel-Bulkley parameters used in Figure 5. 21 including correlation value.

Shear rate range	$\tau_y\ (Pa)$	$k\ (Pa \cdot s^{-1})$	$n\ (-)$	$R^2(-)$
$24 - 1235$	115.8	69.40	0.229	0.996
$24 - 247$	115.8	40.82	0.355	0.995

The Herschel Bulkley parameters are modeled based on the calibrated data points retrieved from laboratory testing. The amount of data points used in a model determines the range and uncertainties of the scope. Hence, the data points introduced to the model should be located in the area of scope. However, to get the best representation of the material behavior, a critical evaluation of the integrity of each data point is necessary, neglecting measurements affected by material properties outside the scope of interest. In this study, flow curves between 24 and 247 s^{-1} from viscometer are considered to sufficient for representing various phases of a submarine slide, for T-bar, flow curves between 1.125 and 18.75 s^{-1} are considered appropriate for assuming undrained conditions, while DSScy are represented of flow curves between 0.00025 and 0.6s^{-1}. Hence, a great span of shear rates is covered, especially towards the lower regions below 20s^{-1}. However, as mentioned in chapter 5.1.5, due to the limitations and measuring mechanisms of each test, a certain uncertainty still remains which should be taken into consideration.

Figure 5. 22 gives an illustration of the algebraic approximation from the Herschel Bulkley model and its relevant scope from viscometer data. The figure illustrates 4 different flow curves based on different amounts of data points. Representing the flow curve with the 5 first data points (yellow curve), a great mismatch between the flow curve and the remaining data points can be observed. Hence, a perception of its extent and limitations is important to establish a representative flow curve.

Table 5. 4: Herschel-Bulkley parameters used in Figure 5. 22 including correlation value.

Curve fitted to	τ_y $[pa]$	k $[Pa \cdot s^{-1}]$	n $[-]$	$R^2[-]$
8 $(all\ points)$	24.2	27.44	0.3037	0.955
7$first\ points$	24.2	32.57	0.275	0.969
6 $middle\ points$	24.2	32.57	0.275	0.978
5 $first\ points$	24.2	18.70	0.387	0.983

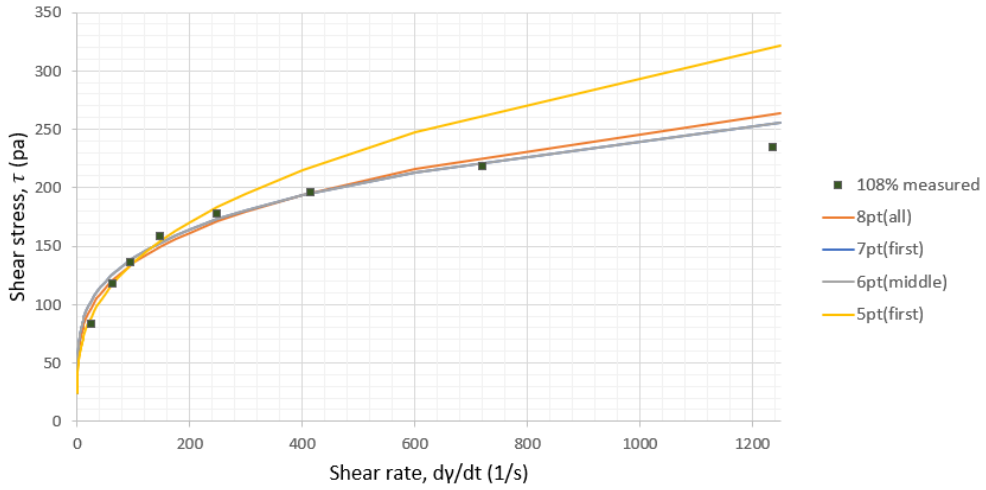

Figure 5. 22: The viscosity flow curve of Kaolin clay at 108% water content presented with 4 best fit curves based on different amount of calibration points. Orange (8pt) curve represents implemented Herschel-Bulkley function for all data points, Blue (7pt), grey(6 middle pt) and yellow (5pt) describes the Herschel-Bulkley function based mentioned points.

Representation of evaluated Herschel Bulkley parameters

The fitted Herschel Bulkley flow curves including measured data points are illustrated in Figure 5. 24 (Viscometer), Figure 5. 25 (T-bar) and Figure 5. 27 (DSScy). The model captures the shear stress evolution for investigated shear strains. The findings from the Herschel Bulkley investigation can be summed up as established flow curves which seems to amplify the observable trends from laboratory results. The retrieved Herschel Bulkley parameters are presented in Table 5. 5 including yield stress, remolded shear strength from fall cone, liquidity index and the correlation coefficient. Notice that the fall cone shear strength, S_{urfc}, is missing for DSScy and T-bar (Su). This is due to lack of fall cone measurements. The T-bar (Su) is based on the Su measurements from T-bar, while the DSScy yield stress is a result of the Herschel Bulkley approximations.

Table 5. 5: Best fit Herschel-Bulkley parameters for Viscometer, T-bar and DSScy tests evaluated on kaolin and BF clay. The % behind the material type indicates water content.

Material	S_{urfc} *[pa]*	*LI [-]*	*Included points [-]*	*Yield stress [pa]*	*Consistensy index, K* $[Pa \cdot s^{-1}]$	*Curvature exponent,n [-]*	*Correlation coefficient,*R^2 *[-]*
Viscometer test							
Kaolin (56%)	1701	0.89	3 first	340.2	85.30	0.551	0.987
Kaolin (65%)	830	1.21	5 first	166	7.45	0.899	0.987
Kaolin (93%)	140	2.21	5 first	28	22.70	0.434	0.989
$Kaolin$ (108%)	106	2.75	5 first	21.2	18.70	0.387	0.983
Kaolin(116%)	69	3.03	5 first	13.8	20.05	0.347	0.950
BF (91%)	2502	0.83	-	-	-	-	-
BF (100%)	1432	0.98	5 first	286	222.10	0.280	0.956
BF (119%)	481	1.27	5 first	96.2	122.82	0.182	0.998
BF (142%	223	1.62	5 first	44.6	98.56	0.160	0.998
T-bar test							
$Kaolin$(62%)	835	1.1	4 *last*	167	286.5	0.22	0.99
$Kaolin$ (87%)	150	2	4 *last*	30	98	0.27	1
$Kaolin$(99%)	100	2.3	4 *last*	20	66	0.271	0.99
$Kaolin(Su$ 62%)	–	1.1	3 *last*	282.6	971	0.10	0.99
$Kaolin(Su$ 87%)	–	2	3 *last*	69	202	0.18	0.90
$Kaolin(Su$ 99%)	–	2.5	3 *last*	39.6	102	0.29	0.99
BF(84%)	2851	0.74	4 *last*	570	1746	0.2	0.98
BF(107%)	820	1.12	4 *last*	164	425	0.28	0.98
BF(119%)	470	1.27	4 *last*	94	293	0.20	0.99
DSScy							
$Kaolin(Su$ 54%)	–	0.82	3	7841	2762	1.22	1
$Kaolin(Sur$ 54%)	–	0.82	3	1100	1584	0.89	1
$BF(Su$ 48%)	–	0.21	3	3509	17276	0.11	0.96
$BF(Sur$ 48%)	–	0.21	3	288	2918	0.15	1

The estimated Herschel Bulkley viscometer flow curves are presented and compared with measured data in Figure 5. 24, Figure 5. 25, Figure 5. 26 and Figure 5. 27. These approximations are a result of the algebraic approach to capture the rheologic behavior of kaolin and BF clay at different material states. Figure 5. 23 (a) illustrates the evolution of the consistency index towards increased LI for T-bar and viscometer experiments. This behavior is further captured through 5 power functions.

Figure 5. 23(b) illustrates the relation between the consistency index, K, and curvature exponent, *n*. The LI ranges between 0.82-3.03 (wc:54-116%) for kaolin and 0.21-1.62 (wc:48-142%) for BF clay. Considering the Herschel Bulkley customization of kaolin clay illustrated in Figure 5. 23 (a) and documented in Table 5. 5, a distinct relation between the Herschel Bulkley parameters can be observed. For increased LI a decrease in yield stress and the consistency index K can be observed for all tests. However, the behavior of *n* is consistent in its response for each test, but changes between experiments. For viscometer tests, the curvature exponent, *n*, seems to decrease with increasing LI, while for T-bar and DSScy an increase in *n* can be observed for increased LI.

The development of the parameters is a result of the change in soil behavior caused by the material transitions from plastic to flow behavior and measuring method. However, this relationship excludes viscometer results from LI: 0.89 and 1.21, due to inconsistent measurements and limitations related to the apparatus. This may also be observed by the number of data points retrieved for kaolin at LI:0.89. The flow curves are, as mentioned, established based on the measured data points. By increasing the amount of such calibration points, the flow curve will change and try to express all the measured data best way possible. Hence, one should question at what shear rate range these flow curves are applicable.

By examining the BF clay, a good correspondence between the numerical Herschel Bulkley predictions and rheological data from the viscometer and DSScy tests can be observed. For both tests we can see similar trends as for kaolin. Both yield stress and the curvature exponent decrease with increased LI, and the curvature exponent decreases for viscometer experiments while it increases for DSScy tests. However, for the T-bar tests, these trends are less prominent for the curvature exponent, *n*. Both the consistency index and yield stress decreases for increased LI, whereas the curvature exponent changes more arbitrary.

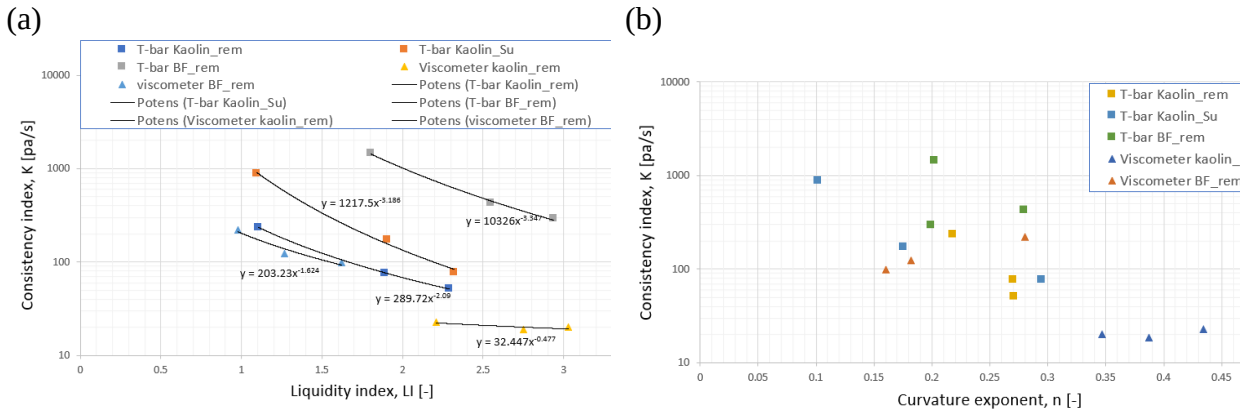

Figure 5. 23: (a) Schematic illustration of the consistency index, K, from T-bar and viscometer results and its relation to LI. (b) Shows the relation between the consistency index, K, and curvature exponent, n, from T-bar and viscometer.

The consistency index has, traditionally, been tabulated in the scientific literature. However, as Figure 5. 22 illustrates and (Saasen & Ytrehus, 2019) reports, these tabulated parameters are not usable for comparing materials outside their experimental scope. This claim is further supported

when we consider the resulting flow curves for kaolin at LI ≈ 2 from T-bar and viscometer (Figure 5. 25 and Figure 5. 24). Both curves represent the approximated strength evolution of kaolin at roughly same LI. However, these flow curves are correlated for two different strain rate intervals.

The viscometer Herschel Bulkley parameters predicts the material behavior for rates between 24 and $247s^{-1}$, while for the T-bar, the same parameters predict the behavior for the rates between 1.125 and $18.75s^{-1}$. This results in two significantly different parameter sets despite using nearly the same yield stress. The quality of using Herschel Bulkley flow curves seems to culminate into whether this model manages to approximate the data sufficiently. This depends ultimately on the data quality and type of material which is investigated.

Finally, it seems that the model manages to capture the shear thinning behavior for both materials at various LI as it develops into a Bingham fluid like behavior. The discussed strain rate dependency seems to be captured by the model, where it can be considered extra prominent for DSScy, illustrated in Figure 5. 27. However, if the material behavior can be compromised and presented as a function based on the Herschel-Bulkley model to be implemented in a numerical model is yet uncertain and not a part of the scope in this study.

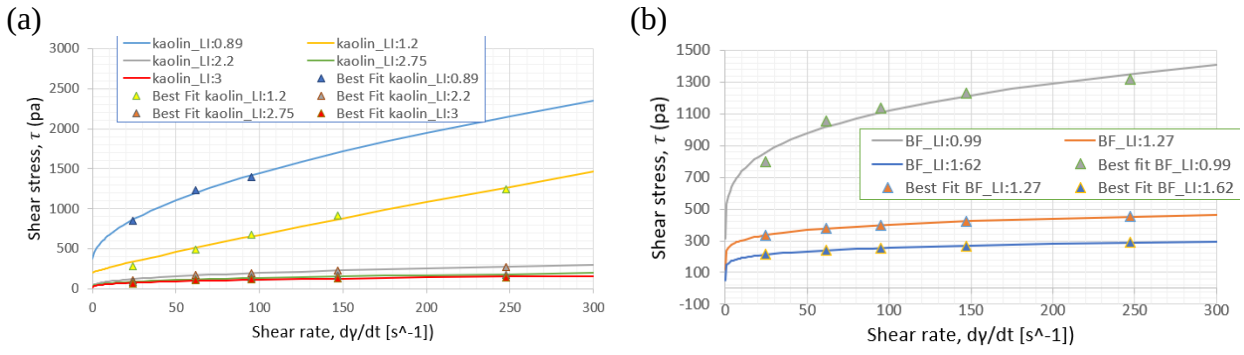

Figure 5. 24: Viscometer shear stress evolution of kaolin (a) and BF clay (b). Herschel-Bulkley best fit approximation (solid lines) and measured shear stress (dots). Presented Herschel-Bulkley parameters are found in Table 5. 5.

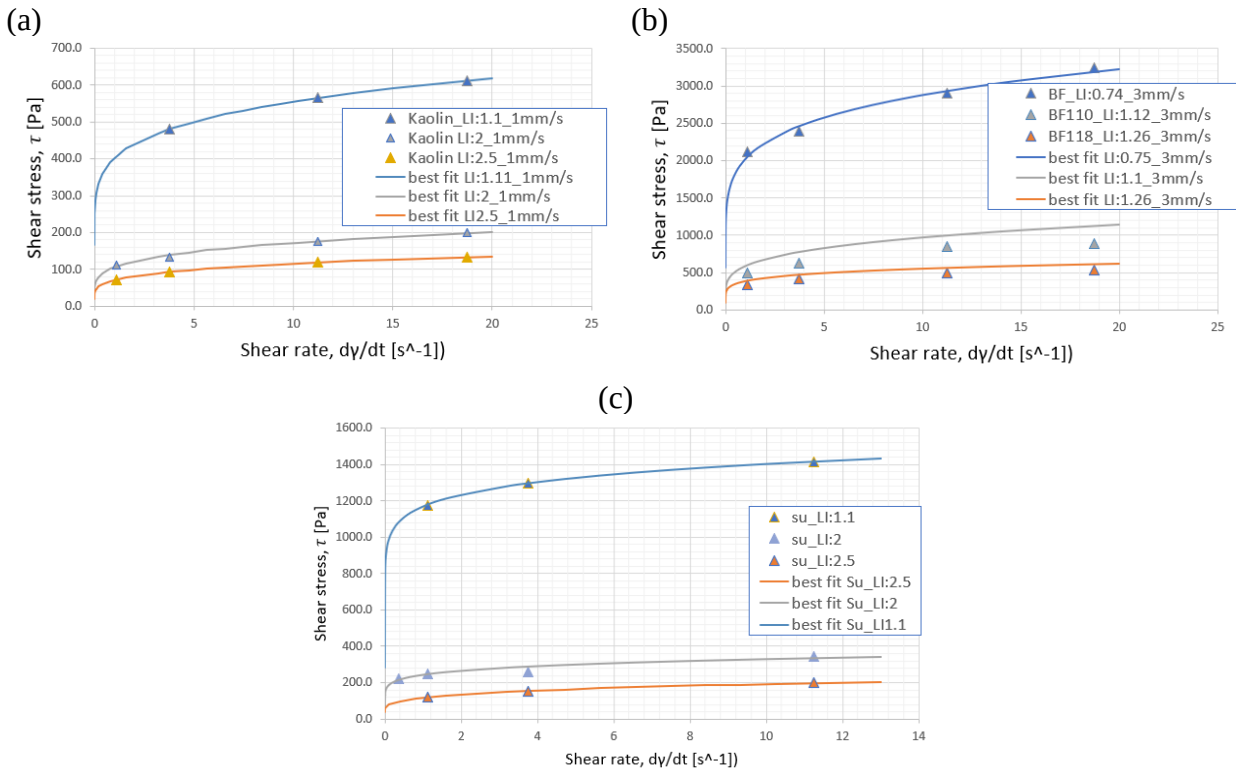

Figure 5. 25: Presentation of the remolded T-bar shear stress evolution of kaolin in (a) and BF clay in (b). (c) presents the un-remolded T-bar shear stress for kaolin. Herschel-Bulkley best fit approximation are presented as lines and measured shear stress are represented as dots. Presented Herschel-Bulkley parameters are found in Table 5. 5.

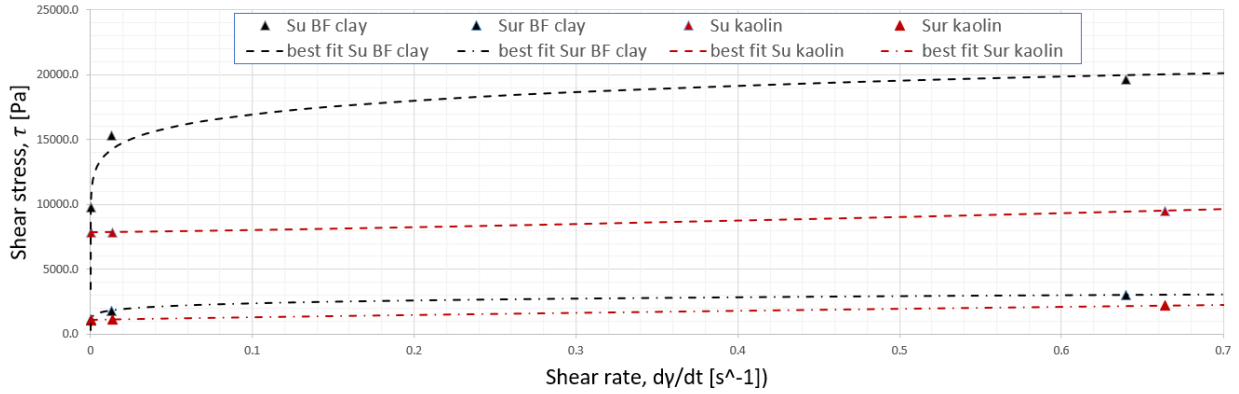

Figure 5. 26: Presentation of the un-remolded and remolded DSScy shear stress evolution of kaolin in and BF clay in. Herschel-Bulkley best fit approximation are presented as dashed lines and measured shear stress are represented as dots. Presented Herschel-Bulkley parameters are found in Table 5. 5. The yield stress is for DSScy also a product of the Herscel Bulkley algebraic approximation, and not the fall cone shear strength.

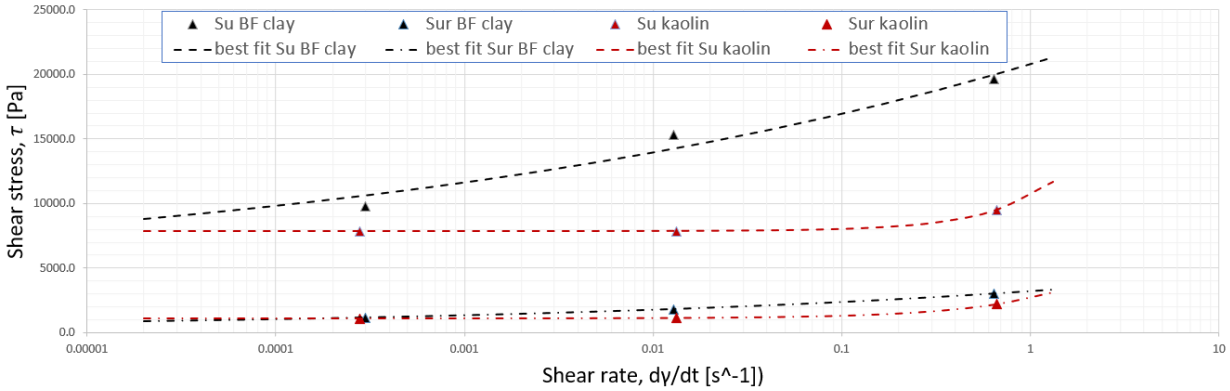

Figure 5. 27: Semi-logaritmic presentation of the un-remolded and remolded DSScy shear stress evolution of kaolin in and BF clay in. Herschel-Bulkley best fit approximation are presented as dashed lines and measured shear stress are represented as dots. Presented Herschel-Bulkley parameters are found in Table 5. 5

5.1.7 Material Shear Strength and Strength Degradation

The established fall cone, viscometer, T-bar and DSScy results are combined and presented based on LI and strain rate in Figure 5. 29. The evaluated remolded shear stress relationship extends over LI: 0.75-3 complimented with trendlines. However, the presented DSScy tests represents all conducted experiments containing shear stresses extracted from $\dot{\gamma} = 0.0001, 0.03\ and \approx 0.65\ s^{-1}$. For this study, only water contents close to LI 0.82 for kaolin and 0.21 for BF clay were investigated. Hence, no material strength development related to change in LI can be established for DSScy. The established shear stresses in Figure 5. 28 are based on, $\dot{\gamma} = 247 s^{-1}$ for viscometer tests, $\dot{\gamma} = 11.25\ s^{-1}$ for T-bar tests, $\dot{\gamma} = 3 s^{-1}$ for fall cone in addition to the DSScy tests. Thus, the shear rate for displayed tests captures a substantial strain rate interval.

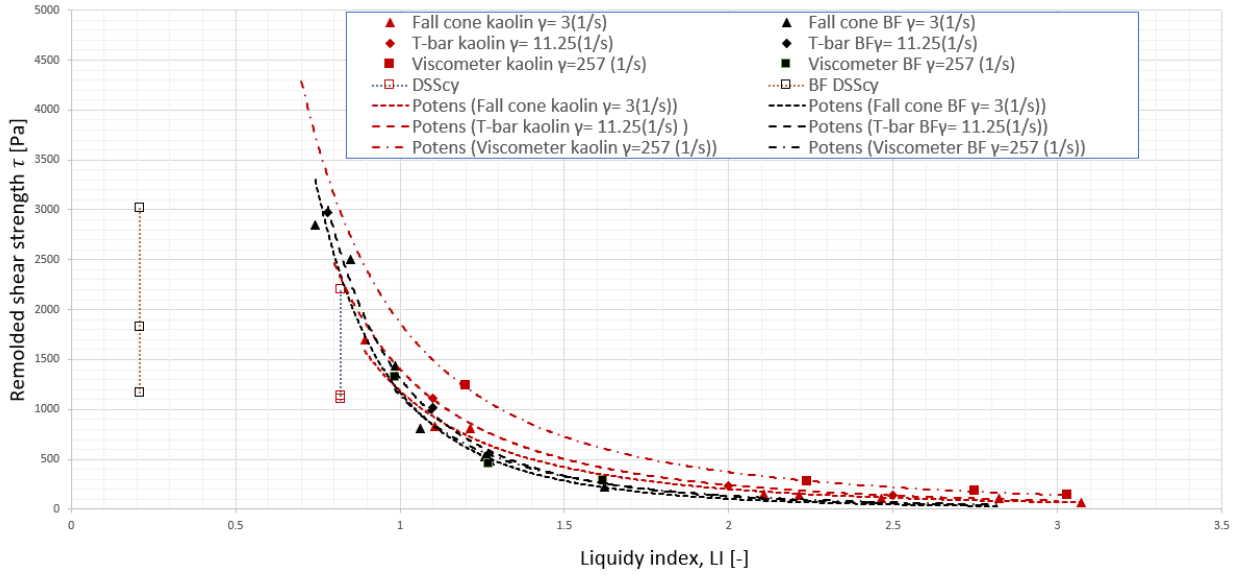

Figure 5. 28: Schematic presentation of the remolded strength evolution with increased liquidity index, LI, from all laboratory tests compiled. Kaolin is represented in red and BF clay in black. Each lab-test is represented with its own type of dashed line. The strain rate at each strength measurement is presented, and for DSScy all conducted strain rates are presented ($\dot{\gamma} = 0.0001, 0.013$ *and* $\approx 0.65\ s^{-1}$).

The observable trends in Figure 5. 28 displays a continuous strength degradation with increased LI for both materials. Note that the shear strength development is influenced by both the strain rate and the change in water content, making the strength evolution dependent on two parameters. One observable behavior is that the strain rate dependency increases with lower LI. Considering the rate dependency through viscometer, T-bar and fall cone, acknowledging the uncertainties this brings, this behavior appears to be more prominent for kaolin compared to BF clay.

The DSScy tests investigates much firmer material states compared to other tests. This reveals a substantially higher rate dependency for both materials at firmer states. This remarkable trend, as the rate dependency changes with water content, can be explained on a molecular level. At lower water content, grains will fill available voids, packing the material more densely. When applied shear forces exceeds the yield stress, flow will occur in the material. Due to its density, this flow will exhibit dilatant behavior, increasing the viscosity for increased shear rates. However, considering the two effects, rate dependency and water content, the water – strength relation becomes quickly dramatic.

The strain rate influence through remolding can, by observing Figure 5. 28, be considered neglectable for any strength evaluation above LI:1. The remolded shear strength reduces by an order of 2 as LI is increased from 1 to 3. As the water content increases, the decrease in shear strength seems to converge until it reacehes liquid state. A phase which is dominated by flow behavior and low grain to grain contact. Hence, the strength dependency is heavily dependent on the water flow between the particles as the rearrange. However, any distinct transition in the governing strength performance regarding the phase transformations, introduced in chapter 2.3, is not observed. The shear strength evolution associated with increased water content can, as a

contradiction to what Jeong et al. (2015) presents in Figure 2. 2, be presented by a power function on the form:

$$\tau = a_1 LI^{-b_1} \tag{5.6}$$

where a_1 and $b_1$are components describing the strength evolution for given LI. Boukpeti et al. (2012) reported a similar finding for describing the remolded shear strength as a function of liquidity index for kaolin and Burswood clay.

Figure 5. 29 represents a semi logarithmic presentation of Figure 5. 28. By also magnifying the rate dependency for lower shear strength, the variations between kaolin and BF clay can also be investigated for higher LI. Here, the same trends are observed, as kaolin behaves more sensitive to strain rates than BF clay for higher LI. This behavior can be further expressed through the power functions represented in Table 5. 6. Power functions for fall cone are represented with an approximated operative strain rate of $\approx 3\ s^{-1}$, while viscometer functions are based on strain rates at $247 s^{-1}$, and T-bar data is based on rates at $11.25 s^{-1}$. However, rheological tests such as viscometer, penetration tests such as T-bar penetrometer or fall cone constitutes the material strength in different ways. This relates measuring mechanisms and limitations related to each test and has been further reviewed in chapter 5.1.5.

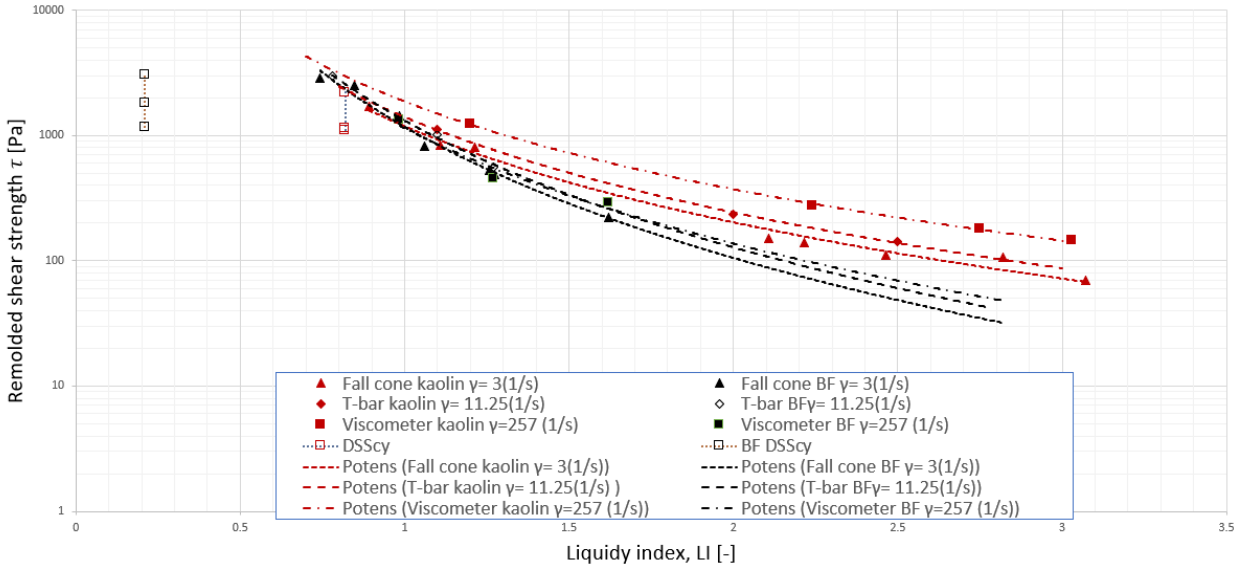

Figure 5. 29: Semi-logarithmic presentation of Figure 5. 28. This includes a schematic presentation of the remolded strength evolution with increased liquidity index, LI, from all laboratory tests compiled. Kaolin is represented in red and BF clay in black. Each lab-test is represented with its own type of dashed line. The strain rate at each strength measurement is presented, and for DSScy all conducted strain rates are presented ($\dot{\gamma} = 0.0001, 0.013$ and $\approx 0.65\ s^{-1}$).

Table 5. 6: Presented power functions and corresponding correlation from Figure 5. 28 and Figure 5. 29.

Test	*Relationship*	R^2
$Fall\ cone_{Kaolin,\dot{\gamma}=3}$	$\tau = 1187 \cdot LI^{-2.55}$	0.99
$Fall\ Cone_{BF,\dot{\gamma}=3}$	$\tau = 1173 \cdot LI^{-3.475}$	0.94
$Viscometer_{Kaolin,\dot{\gamma}=247}$	$\tau = 1869 \cdot LI^{-2.327}$	0.99
$Viscometer_{BF,\dot{\gamma}=247}$	$\tau = 1143 \cdot LI^{-3.057}$	0.98
$T\ bar_{kaolin.\dot{\gamma}=11.25}$	$\tau = 1404 \cdot LI^{-2.428}$	0.99
$T\ bar_{BF,\dot{\gamma}=11.25}$	$\tau = 1315 \cdot LI^{-3.361}$	0.99

Cyclic strength degradation

Figure 5. 30 and Figure 5. 31 illustrates the cyclic strength degradation based on a τ/τ_{rem} normalization for DSScy and T-bar tests. This shows how the evolution of cyclic degradation for cycle 1, 4 and remolded state (cycle 18) at different strain rates and can represent the remolding of an early phase submarine landslide. Kaolin, presented in Figure 5. 30**,** exhibits a distinct behavior for un-remolded material, where the rate dependency increases for lower strain rates. As the material degrades, this dependency decreases, which also can be noticed for the T-bar tests. For both DSScy and T-bar, this effects nearly doubles when lowest and highest strain rate is considered for cycle 1. The rate dependency shows further correlations with LI, displaying a higher dependency for firmer material (lower LI). However, these effects reduce for increased cycling, but they seem to decrease in the same order for kaolin clay.

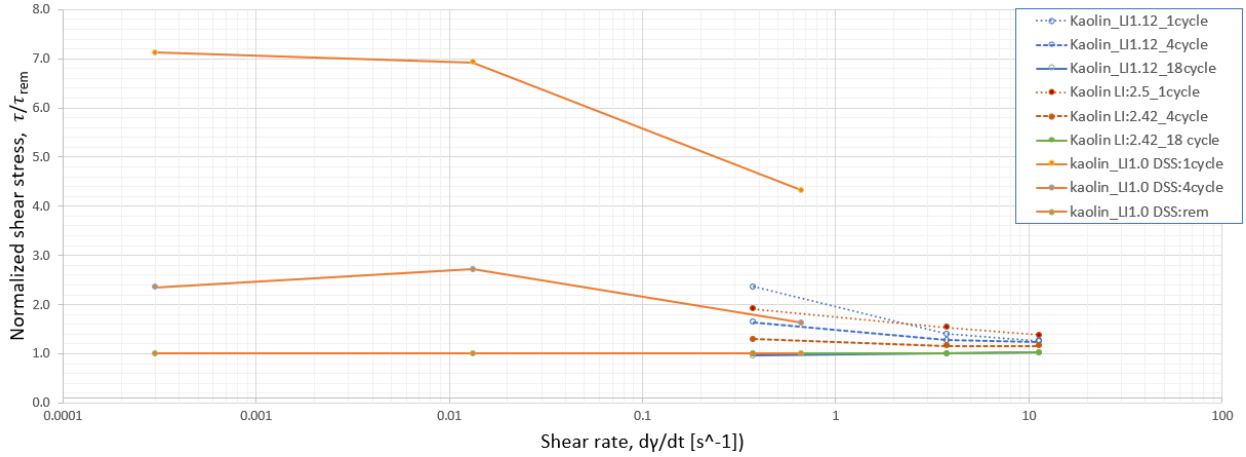

Figure 5. 30: The cyclic degradation of kaolin clay related to strain rate dependency for T-bar and DSScy. Here, cycle 1, 4 and 18 is presented for T-bar, while cycle 1, 4 and remolded state (last cycle) is presented for DSScy.

The rate dependency of BF clay (Figure 5. 31) exhibits similar but more modest cyclic strain rate tendencies than kaolin. Considering lower shear rates, the strength variations seem to be smaller. Only for DSScy $\dot{\gamma} = 0.6$ at cycle 1, a distinct variation can be observed. For the remaining data, this behavior seems to disappear as the soil structure gets remolded. The cyclic degradation related to BF at LI:0.74 proves to be sufficiently sensitive towards remolding. However, this test resembles a much firmer material state than for presented kaolin test, making a comparison

difficult. The observed T-bar results correlates well with the observable trends from Figure 5. 28, where BF exhibits a greater sensitivity towards firmer material states. The general observations fit well with the statement that clays exhibits more pronounced rate dependency regarding initial loading and becomes less significant at increased cycling.

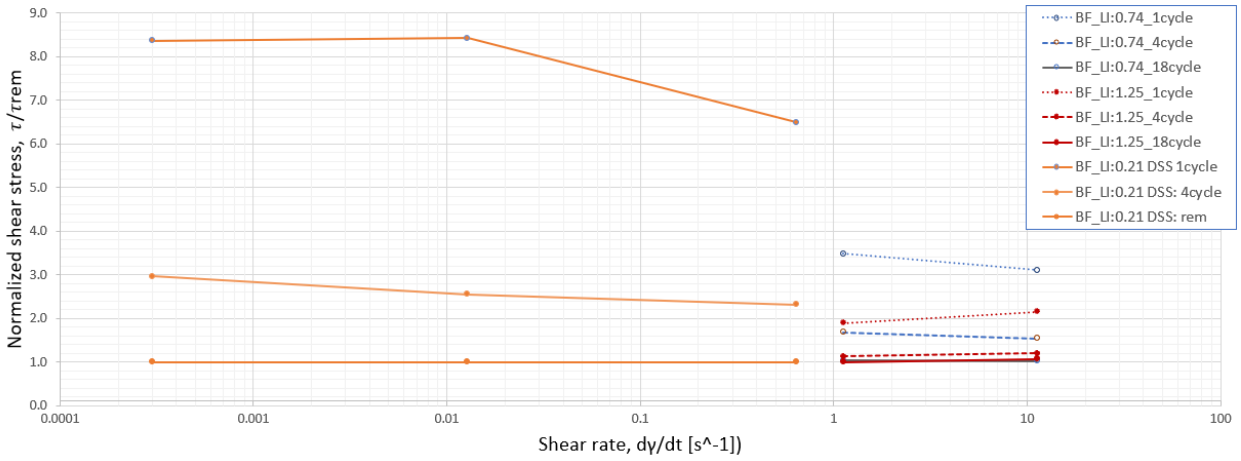

Figure 5. 31: The cyclic degradation of BF clay related to strain rate dependency for T-bar and DSScy. Here, cycle 1, 4 and 18 is presented for T-bar, while cycle 1, 4 and remolded state (last cycle) is presented for DSScy.

Yield stress

Figure 5. 32 presents the development of yield stress in relation to increased LI. The initial yield stress was established through fall cone experiments for remolded tests and T-bar for un-remolded kaolin tests. The stress range extended from 14-340 pa for kaolin, and 45 to 570 pa for BF clay. The empiric evaluations used to describe the approximated yield stress are described in 5.1.6. Both soils exhibit similar patterns which can be expressed through power functions on the form as Eq.5.6 or in Table 5. 6. This way of expressing the yield stress behavior can be supported by Jeong (2013), who reported similar relations for rheological behavior of sediments from Saguenay fjord.

The yield stress exhibits a great dependency on the interactions between grains and flow. It seems that material state and flow development compose det governing behavior of the yield stress outshining material properties. Observations from Figure 5. 32 displays similarities between kaolin and BF clay despite holding a different LI. The un-remolded yield stress from T-bar and the remolded yield stress from fall cone show close relations where the curvature exponent is nearly identical. However, as the yield stress is a function of the T-bar strength and fall cone strength, we can observe identical curvature exponents for yield stress and shear strength.

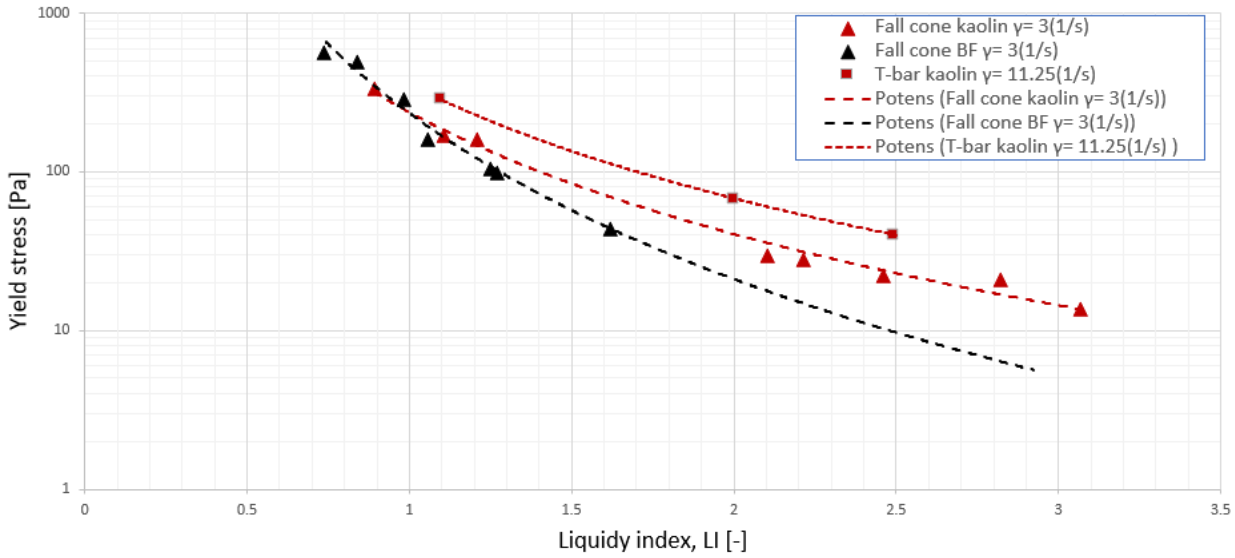

Figure 5. 32: Liquidity index vs. Yield stress for kaolin and BF clay. The yield stress for remolded clay is determined through fall cone, while yield stress from un-remolded kaolin clay is established through T-bar tests.

Table 5. 7: Presented power functions and corresponding correlation for the estimated yield stress

$Test$	$Relationship$	R^2
$C_{urfc,kaolin}$	$\tau = 237 \cdot LI^{-2.55}$	0.99
$C_{urfc,BF}$	$\tau = 234 \cdot LI^{-3.475}$	0.93
$T\ bar_{kaolin}$	$\tau = 356 \cdot LI^{-2.428}$	1

5.1.8 Flow Behavior of Fine-grained Soils in the Transition from Solid to Liquid

Recent theory and conducted soil investigation have displayed the shear strength development in relation to remolding, water infiltration and lubrication. Current discoveries reveal a strength behavior which is largely dominated by the water content rather than geological and molecular properties. Further investigations reveal a substantial strain rate dependency for plastic state, where both BF and kaolin clay exhibits a stronger rate dependency for lower LI, while the rate dependency decreases for both materials with increased LI. This decrease seems to be more significant for BF clay than kaolin clay. However, both materials display similar properties and behavior at related LI implying that the decisive elements appear to be outside factors such as water infiltration.

Strength reduction due to water infiltration leads to progressive reduction of shear strength, which can simulate the shear layer in a submarine slide. This is key in explaining the increased mobility, high velocities and long travel distances of submarine debris flows. Kvalstad et al. (2005) examined the decay of shear strength and relating stress and strain development for the marine sediments in conjunction with the Storegga slide. The relating discoveries showed a strain softening due to increased remolding during the slide initiation, which turned out to be important

for understanding the flow transformation and associated slide dynamics. This has been supported by various authors (Blasio et al., 2006; S. W. Jeong et al., 2015; Kvalstad et al., 2005) as describing the strength evolution of yield strength with associated shear strain through the transition phase of solid to liquid state.

Studying and predicting the flow behavior of a submarine debris flow requires that rheological parameters, used in a in a compatible model, must be representative for the real field conditions. The runout characteristics and mobility of the moving mass are, through constant remolding and water infiltration, influenced by rheological and material properties(Jeong et al., 2010). The compiled results of kaolin and BF clay show a resemblance between inspected materials. The material behavior presented through rheological properties and strain rate dependency at increased LI seems to gravitate towards a liquid phase, more affected by the water intrusion than the soil properties. This phase transition transpires at similar LI and further captured by already mentioned power functions. Both materials exhibit Bingham-like fluid behavior which can be studied through the Herschel-Bulkley approximations at various strain rates. The resulting yield stress and plastic viscosity can according to Imran et al. (2001) affect the front velocity of debris flows. High yield stresses cause typically relatively short run-out distances. Ultimately, making flow transformations related to strength parameters as an important preliminary study to help understand and describe the debris flow mobility in flume experiments and mathematical modelling.

5.2 Flume Model Experiments

The flume model results are presented and discussed through 3 sub-chapters. Firstly, flow types and flow regimes will be addressed, secondly, the run-out experiments will be investigated and lastly, the impact force response. Table 5. 8 summarizes characteristics for the conducted flume model experiments and presents important parameters defining the flow characteristics. By using dimensionless parameters, the flow regimes of various experiments can be scaled up and compared with field conditions.

Table 5. 8: Model Flume experimental results summarized. Wr/w0 represents the flow discharge, and V steady is established from pore pressure measurements. Flow height, drag coefficient and Froude number are established for slide conditions at impact pile. Su-rem is established based on correlations with T-bar experiments.

Test	Objective	Slope	State	Wc	Wr/w0	Flow height	V steady	Q or L	Su-rem	Drag Coeff.	Froude Num.	Re-num.
[-]	[-]	[°]	[-]	[%]	[%]	[mm]	[m/s]	[N]or [cm]	[pa]	[-]	[-]	[-]
1	Run-out	18	Remoulded	105	94		0.65	168	62	-	-	9.84
2	Impact	18	Remoulded	82	87	141	0.78	9.57	171.7	3.8	1.12	5.45
3	Impact	18	Remoulded	85	89	160	0.66	10.72	147.9	6.06	0.90	4.48
4	Impact	18	Remoulded	86	97	139	0.66	9.89	140.9	5.74	0.97	4.69
5	Impact	18	Remoulded	110	94	187	0.71	4.22	51.5	1.98	0.99	14.06
6	Run-out	18	1d consolidated	94	68	104	0.61	80	97.6	-	1.07	5.65
7	Run-out	18	1d consolidated	100	68	145	0.59	80	75.7	-	0.90	6.71
8	Impact	18	1d consolidated	81	54	114	0.58	5.98	176.4	2.86	0.92	2.87
9	Impact	18	1d consolidated	85	68	154	0.61	8.67	144.7	6.37	0.85	3.83
10	Impact	18	1d consolidated	86	75	120	0.58	6.52	137.6	3.91	0.92	3.62
11	Impact	18	1d consolidated	91	76	113	0.64	6.65	109.6	4.1	1.07	5.48
12	Impact	18	1d consolidated	96	79	118	0.68	5.76	88.3	3.35	1.13	7.61
13	Impact	18	1d consolidated	103	88	113	0.64	5.27	65.8	2.89	1.12	8.85
14	Impact	18	1d consolidated	107	75	140	0.49	3.99	57.4	-	0.78	6.01
15	Impact	18	1d consolidated	113	88	187	0.70	4.22	17.75	2.18	0.98	15.16
16	Impact	12	Remoulded	89	85	116	0.60	7.70	122.4	5.37	0.87	4.42
17	Impact	12	Remoulded	95	93	122	0.56	4.86	91.6	3.96	0.81	4.96
18	Impact	12	Remoulded	110	93	136	0.55	2.90	52	2.44	0.79	8.43
19	Impact	12	1d consolidated	99	85	98	0.54	3.51	79.4	3.08	0.88	5.41
20	Impact	12	1d consolidated	100	84	99	0.55	4.99	76.2	4.25	0.90	5.83
21	Impact	12	1d consolidated	109	80	80	0.50	4.30	53.2	4.45	0.94	6.73

5.2.1 Flow Types and Flow Regimes

The flow regimes can be investigated through visual observations, velocity measurements from video recordings and PWP measurements, and general instrumentation in the laboratory. Measuring the slide velocity using video recordings and PWP measurements, two velocity profiles can be established. For video recordings this presents a dynamic profile, sampling the position and time through many data points. For PWP measurements, the position and time is established through 4 to 6 measuring points with an excellent accuracy. Hence, the profiles are used differently depending on the purpose. However, all dimensionless parameters are established through PWP measurements.

Velocity profile and related flow behavior

Through the model slide investigation, it became clear that subaqueous flows were highly transitional, as flow regimes with relating flow mechanisms changes with changing composition and slurry disintegration. Based on video observation and PWP measurements, we can characterize the flow behavior into 3 phases: 1) A de-acceleration phase after initiation due to increased dynamic pressure, 2) hydro planning and steady flow phase, and 3) impact or deacceleration due to slope angle decrease. However, flow regimes related to slide impacts or deacceleration in the deposition flume could not be measured due practicalities and uncertainties.

Figure 5. 33 presents the position of the slide front as a function of time based on all video recordings distinguished by the slope angle, where (a) presents 18° and (b) 12°. No large deviation or trends can be observed related to changing water content. It seems that most experiments followed similar slide paths, but that the variations between experiments increased for a slope degree of 18°. By converting this, a function of velocity can be established, showing the evolution of velocity through the full slide event.

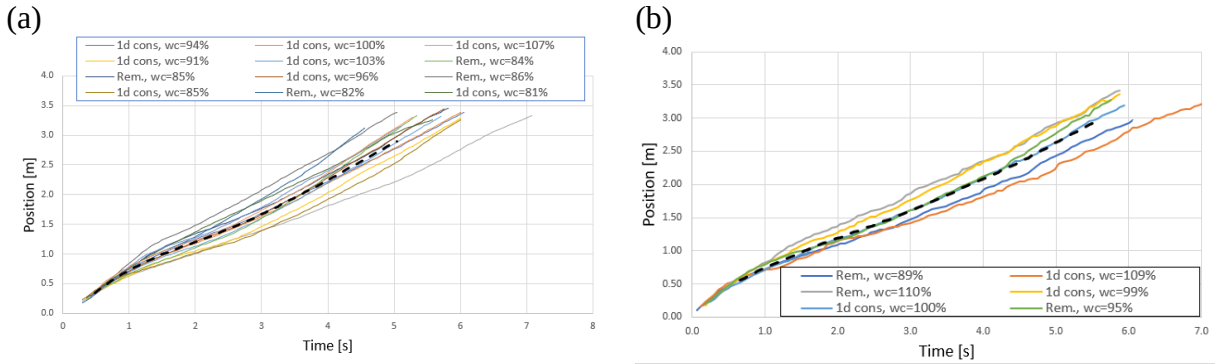

Figure 5. 33: Measured positions of debris flow fronts for all experiments as a function of time based on video recordings. (a) represents 18-degree slope and (b) presents 12-degree slope. Dashed lines in black represents the mean response of tests conducted on 18- and 12-degree slope angle.

Figure 5. 34 presents the averaged velocity profiles for all tests at given slope angle. Due to data processing and necessary adjustments regarding established coordinate system in TRAKCER, the presented velocity profiles follow an offset. This offset can be observed in Figure 5. 33 and Figure 5. 34, and can be associated to uncertainties related measurements, or changes due to changing slope angle.

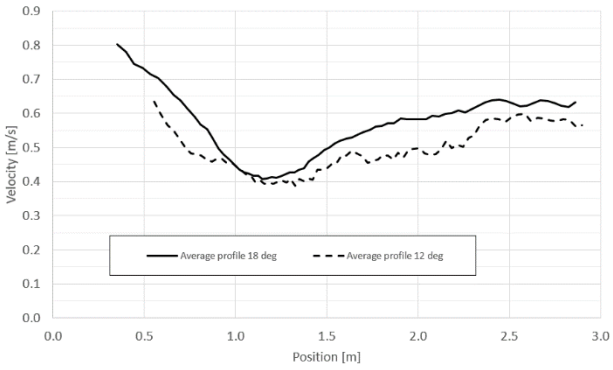

Figure 5. 34: The average velocity profile based on video recordings and data processing in TRACKER. 18° is showed by a solid line and 12° is showed as a dashed line.

The established velocity profile for both slopes resemblances a distinct behavior. The flow path decreases through the initiation

phase and as it establishes steady flow conditions it starts accelerating again before the sampling is stopped right before the impact pile (see Figure 4. 2 and Figure 4. 3 for illustration). This behavior is heavily related to the slurry disintegration, remolding and the onset of hydroplaning. Figure 5. 35 (a-e) captures the transition from initiation through remolding and the onset of hydroplaning. During this flow phase complex interactions of high dynamic pressure leads to a lifting and deformation of the material, which further governs a surface wave. This substantial lift of the flow head is caused by large pressure on the flow front and suction from the water disturbance causing the material to deaccelerate. Figure 5. 35 (a-c) captures this event as the slide front pressures the water down causing a surface wave. As the pressure increases, the slide front collapses causing turbidity which can be seen in (d) and (e), leading to a smaller front area and an acceleration of flow material. Through this slide transition a small well-defined boundary layer of water is established beneath the slide body erasing ground contact. As this onset of hydroplaning occurs, the friction decreases immensely leading to an acceleration of the flow body as it approaches steady flow conditions as illustrated in (f). The red dots represent sampling points as the slide progresses and for (d) the calibration tool is also illustrated.

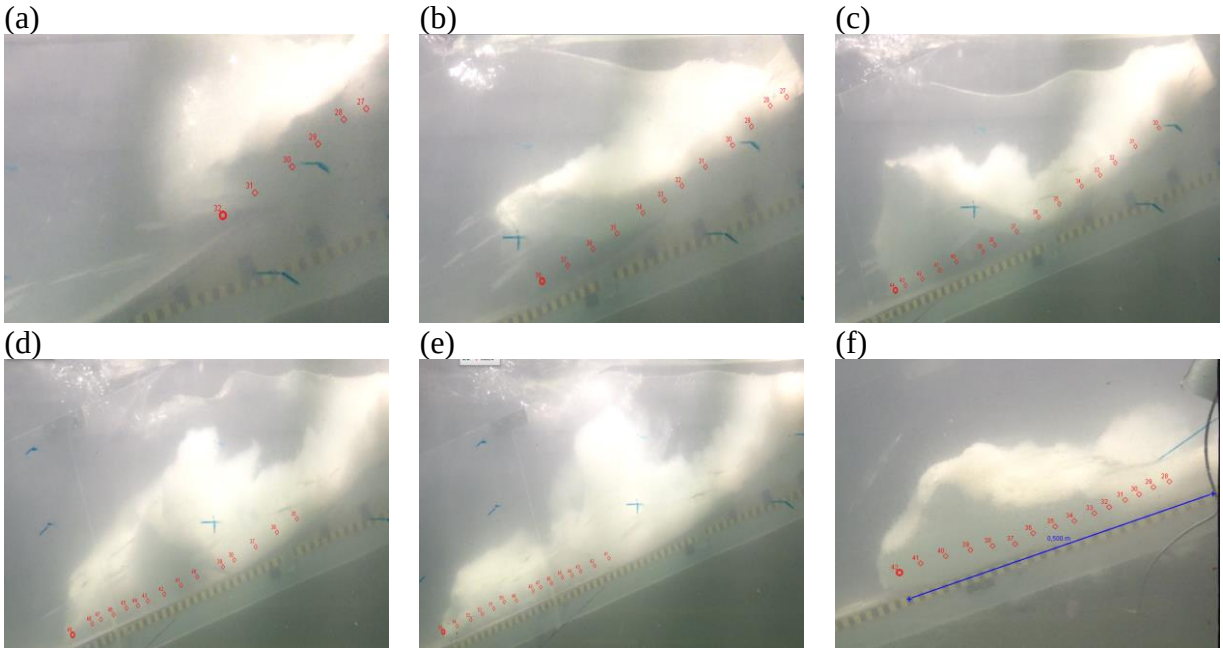

Figure 5. 35: The remolding process during the deacceleration phase of Test 8.at 18 °slope. Red dots presents TRACKER sampling points.

Similar events can also be presented for investigations conducted at 12° slope. However, due to a lower inclination the initial velocity becomes smaller leading to a smaller frontal pressure. These characteristics can be seen in Figure 5. 36 (a-c), showcasing similar but more modest behavior than Figure 5. 35. The slide front experiences a similar uplift only smaller, and the surface wave generation can also be observed as more moderate compared to 18° slopes. Due to smaller impact from surrounding forces, the material remains more intact causing less turbidity. Similar to Figure 5. 35, we can observe a small basal layer establishing under the soil even after the uplifting. This layer is identified as hydroplaning causing the slide front to accelerate.

The effect of these events can also be reflected in the velocity profile in Figure 5. 34, as the slide front velocity is more affected for 18 ° slope rather than 12° slopes. However, as steady flow is established, we can observe a higher acceleration and steady state speed for steeper slope.

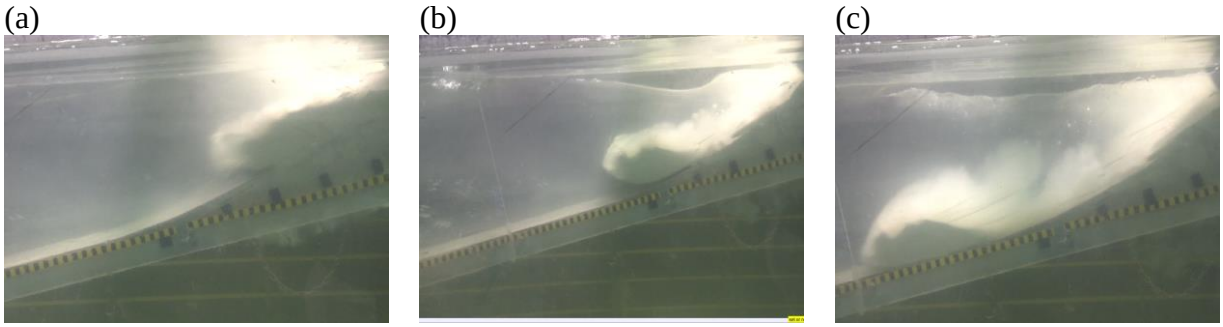

Figure 5. 36: The remolding process during the deacceleration phase of Test 21 at 12° slope.

Longitudinal deformation and velocity field development

The steady state velocities for conducted model flume tests are presented in Figure 5. 37. The displayed steady state velocity is established through PWP-measurements detecting the change in PWP with time, as illustrated in Figure 5. 38. The variations in steady state velocity for increased water content can be considered as small. While there can be observed a small increase in steady state velocity for remolded tests versus 1d consolidated. As expected, and in good agreement with the velocity profile from video recordings, the average steady state velocity increases with the slope angle.

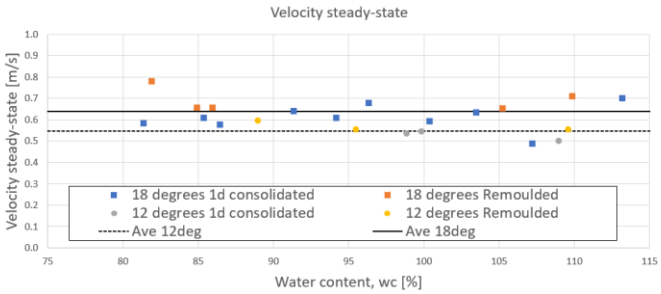

Figure 5. 37: Steady state velocity for all tests distinguished into remolded and 1d consolidated tests for 18° and 12° slope.

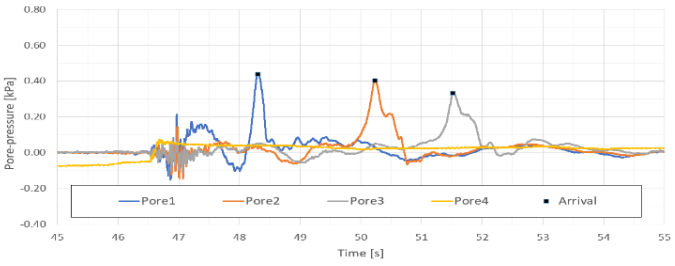

Figure 5. 38: Data processed PWP measurements of Test 8. Pore1 represents first measuring point after initiation, Pore 2 and 3 follows afterwards. Pore 4 did not measure during impact testing.

However, as the slide progresses downstream, an internal change in velocity can be observed. This can be observed through video recordings or PWP measurements. Figure 5. 38 captures this development, as the flow head velocity increases compared to the flow body as the slide progresses downwards. This change in internal velocity resulting in stretching and elongation of the body. This mechanism can be caused due to higher bed friction for the flow body than the flow head, ultimately leading to a separation of the flow head and body. During this process, induced shear

planes and localized shearing can arise leading to cracks in the slide material. As these cracks increases, the water intrusion escalates affecting the slide rheology and changing the flow coherency. This process is also referred to as necking, a typical phenomenon for clay rich debris flows (Ilstad et al. (2004)).

Flow coherency

Figure 5. 39 shows the variation in flow characteristics regarding kaolin samples with low water content and samples with higher water content. For this example, test 8 (holding wc 81%) is presented in (a) and test 15 (holding wc 113%) presented in (b) are displayed. Pictures are based on video recordings taken from the overview camera. These model experiments exhibit very different flow behavior and flow characteristics which are governed by the internal yield strength of the material. However, any effects due to initial state conditions such as consolidated or remolded material state was not observed regarding flow characteristics, and therefore not discussed.

(a) (b)

Figure 5. 39: (a) presentsTest 8 a strongly coherent flow for 18° slope, (b) presents Test 15 a weakly coherent flow for 18° slope.

Figure 5. 39(a) demonstrates a strongly/moderately coherent flow where the dynamic stresses acting on the slide front are not sufficient to induce laminar shearing layer within the slide material. The kaolin-drift occurring behind the slide masses can be affiliated as small turbidity flows but are however also a result of erosion of individual particles from the induced shear stress occurring at the shear surface between stagnant water and moving slide masses. The slide masses in (b) displays large amounts of turbidity exhibiting characteristics of a weakly coherent flow. Weakly coherent flows experience turbulent mixing of the slide material, especially at the slide front. These materials are exposed to dynamic stresses causing water infiltration and further reducing the yield strength. Consequently, the grain structure falls apart and the material undergoes a flow transition which leads to increased turbulence and a reduced bulk density.

The appearance of turbidity is closely related to the connection between the dynamic pressure and internal yield stress of slide material. As the dynamic pressure surpasses the internal yield stress Hampton (1972) suggested that the material goes from an strongly coherent flow to moderately coherent flow. However, Mohrig & Marr (2003) investigated this statement and introduced a way of quantifying this transition from strongly to moderately coherent flow through the relation between the dynamic stagnation pressure and yield stress.

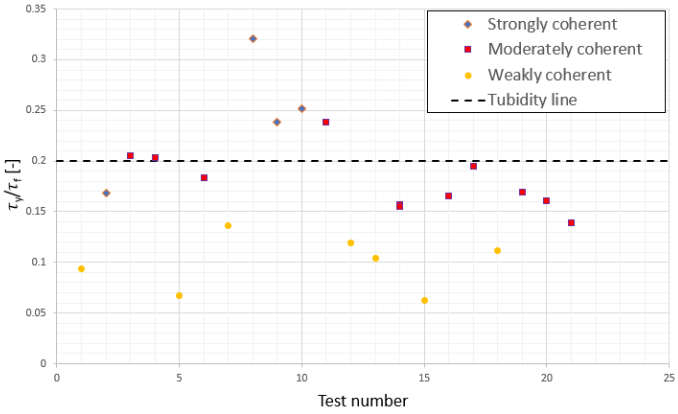

Figure 5. 40: Shows the coherency of any particular slide experiment. Ratio of yield strength, τ_y, to dynamic stress, τ_f, for 21 experimental flows. The turbidy line presents a treshold value for strongly coherent flow similar to Mohrig & Marr (2003) findings.

The stagnation pressure, τ_f, originates from the Bernoulli equation presented in Eq. 2.15. The yield stress, τ_y, can be found using the power functions established in Table 5. 7. Figure 5. 40 presents the yield stress – stagnation pressure ratio (τ_y/τ_f) for each test, where higher τ_y/τ_f often indicates stronger coherence. This data shows the transition from strongly coherent flow to moderately coherent flows occurring over relatively narrow span. The labeling of flow occurrence is based on visual inspections. Hence, we can see some uncertainties by quantifying such behavior. The turbidity line marks where moderately and weakly coherent flows are found. This establishment can be associated with values $\tau_y/\tau_f < 0.2$. This value was also found by Mohrig & Marr (2003), and supports the original proposal made by Hampton (1972) that a change in character of the interface between the front section of a flow and the surrounding fluid occurs as the dynamic stresses acting on the head exceeds the yield strength for the slide material.

However, considering the transition from moderately to weakly coherent flow, the data pattern shows no distinct trend. This lack of definition can be explained by uncertainties related to initiation the slide and remolding during early slide phase. Because of this uncertainty, a suggestion that this transition can be associated with τ_y/τ_f values somewhat smaller than the critical turbidity line at 0.2. However, it is worth assessing this characterization in relation to the effective Reynolds number.

Figure 5. 41 illustrates an intermediate flow behavior characterized as strongly/moderately coherent flow for 12° slope.

Figure 5. 41: Test 21 which exhibits an intermediate flow behavior characterized as strongly coherent flow for 12° slope

Reynolds and Froude number

Further information of the flow regimes can be quantified by investigating the Reynolds and Froude number. However, a significant uncertainty remains due to break up and remolding effects affecting the material composition during flow. This comes from segregation, remolding and water infiltration changing the material rheology and material properties. As more water infiltrates, the density changes together with inherent strength properties. As these flows exhibit non-Newtonian flow in accordance with Herschel Bulkley rheology, the Reynolds number can express this behavior as a function of strain related strength based on Zakeri et al. (2008) formulation presented in Eq.2.18. For the Reynolds number we can find a trend between characterization of flow turbidity and the Reynolds number, where very low Reynolds number (<5) rheological measurements confirms a laminar regime. However, this method is highly uncertain for turbulent flows, making Mohrig & Marr (2003) approach of quantifying the flow coherency more suitable.

As explained in chapter 2.8 and visually illustrated in Figure 5. 35 and Figure 5. 36, the hydroplaning of subaqueous flow is caused by the dynamic stagnation pressure as a function of submerged debris load. As the velocity increases, the resulting stagnation increases, or when the water content/water infiltration increases, the submerged debris load decreases. The simple balance can be expressed through the Froude number, and therefore be used as an indicator of onset of hydroplaning. However, regarding the change in properties due to segregation and remolding of the slide material, a significantly uncertainty still remains when predicting the Froude number, especially considering weakly coherent flows. Considering that clay is low permeable and video observations verifying intact slide material, an attempt of expressing the Froude number in relation to hydroplaning is attempted.

Figure 5. 42 presents the Froude number based on slide velocity between PWP measurement 1 -2 and 2-3 (see Figure 4. 2) and initial density, ρ_s. The general trend reflects the velocity profile presented in Figure 5. 34, where the Froude number increases as the slide front progresses downwards. Mohrig et al. (1998) proposed a range for the onset of hydroplaning related to the Froude number. Through experimental investigation he suggested a threshold value of 0.3-0.4 Frd for hydroplaning to occur. This claim fits well with observations and calculations from conducted experiments. As Figure 5. 42 indicates based on Mohrig et al. (1998) proposal, all conducted experiments should have experienced hydroplaning, which also is the case. For all conducted model slide experiments hydroplaning was observed. Leading to a substantially effect on the flow velocity and change in flow behavior.

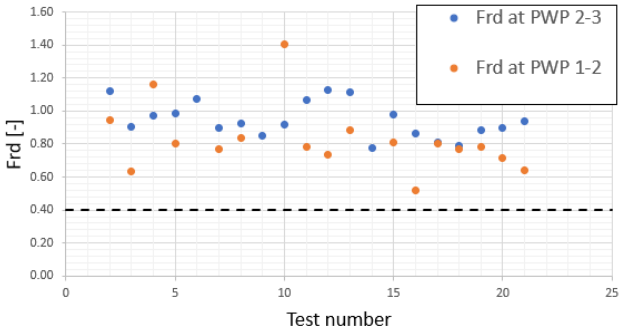

Figure 5. 42: Value of the densimeteric Froude nuber, F_{rd}, at given test number. Values are tabulated in Table 5. 8. Dashed line indicates the treshold number for hydroplaning.

5.2.2 Run-out Distance

3 run out experiments were conducted, Test 1, Test 6 and Tests 7, with variating water content. Within this configuration, all experiments were repeats of each other following the same procedure including identical triggering mechanism, water level and volume. However, the amount of material which was triggered could vary. Some material was often never discharged from the triggering box, and in some cases slide material settled in the runout section of the flume.

Figure 5. 43 presents the total volume discharge for each test based on water content. Similar parameters are listed in Table 5. 8 for each experiment. This shows that the total discharge increases with water content and is slightly increased for remolded material.

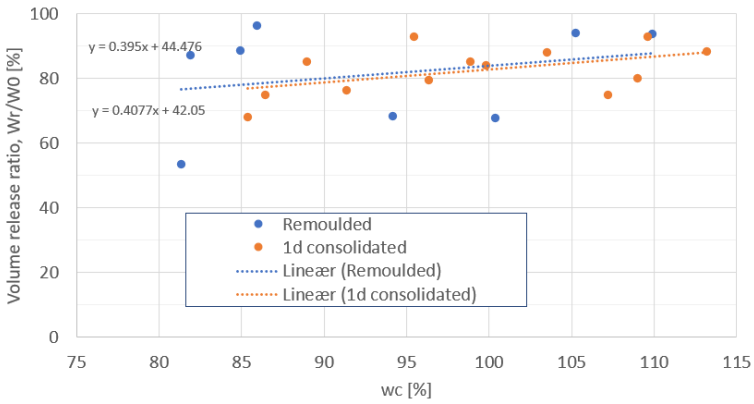

Figure 5. 43: Total volume discharge for all tests plotted against water content.. Remolded material

As might expected, the runout distances of the 3 experiments correlated strongly to the coherent flow mass and the slurry rheology. This can be summarized into that flow mass, yield stress and viscosity were decisive components regarding the runout length. Figure 5. 44 illustrates conducted runout tests and its respective slide deposition in the deposition flume.

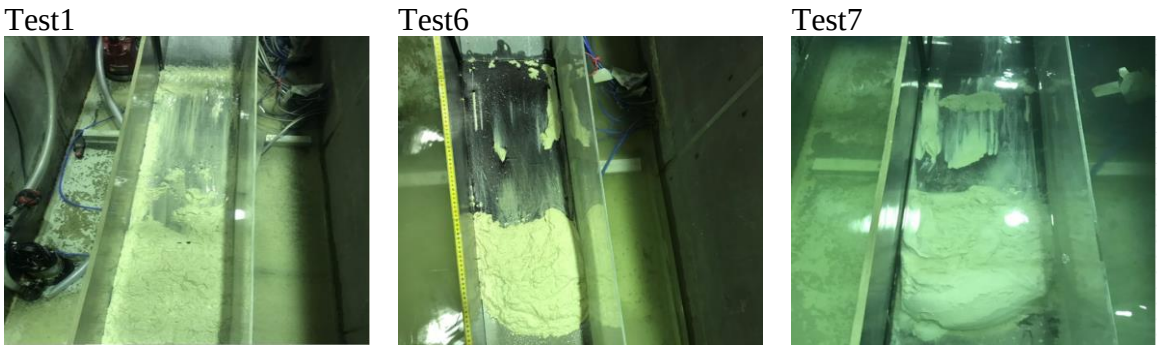

Figure 5. 44: Slide deposits from runout experiments. Test 1 reached 168cm while Test 6 and 7 reached 80cm.

Test 1 represents the most liquid slurry containing the lowest yield stress and viscosity and most volume discharged. The respectively test was measured to a runout distance of 168cm from the transition between run-out and deposition section holding a debris thickness of approximately 5-6cm.

Test 6 and Test 7 seems to exhibit similar characteristics. Holding water contents of 95% and 100% and similar discharge volumes, both materials measured runout distances of 80 cm from the start of the deposition section. The relative deposition height was approximately 6 cm.

It can be observed that each subaqueous flow propagated well beyond the breakup of the slope. However, considering Test 1 compared to Test 6 and Test 7, we can measure a runout distance twice the length for Test 1. This supports the claim that the slide mobility is highly dependent on the clay rheology and surrounding processes such as hydroplaning.

Both test 6 and 7 there were incidents of necking, causing a thin layer of deserted material between upslope deposits, as the flow head ran out ahead of the body, illustrated in Figure 5. 45. Ultimately, the runout distance can be understood as a result of complex interactions between clay rheology, hydroplaning and volume effects, where further investigation is necessary to determine any distinct pattern.

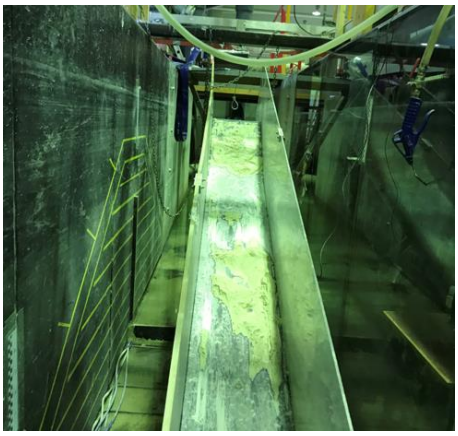

Figure 5. 45:Early slide deposits segregated from the slide head due to necking. Picture from Test 6.

5.2.3 Impact Force

In total 18 experiments were carried out studying impact forces on a cylindrical pile covering the impact forces at various flow behaviors and slope inclinations. The flow head velocity near the impact pile ranged between 0.5 m/s and 0.8m/s exhibiting Reynolds numbers between 3 and 15. The debris flow heights spanned between 80mm and 187 mm displaying an average flow height of 125mm for 18° slopes and 108mm for 12° slope. This distinct flow height trend can be a result

of discharge or lifting/remolding mechanisms during early stages of the slide. However, considering the discharge for each test, this seems unlikely, leaving the lifting/remolding mechanism as a plausible reason.

Figure 5. 46 shows the typical impact force response in flume experiments. This represents Test 21 showcasing approximately 1.5 seconds of a full slide run. Figure 5. 47 presents the video observations for Test 21 as slide impact occurs. Such impact events were often over in only a second or two, as the flow continued past the cylinder.

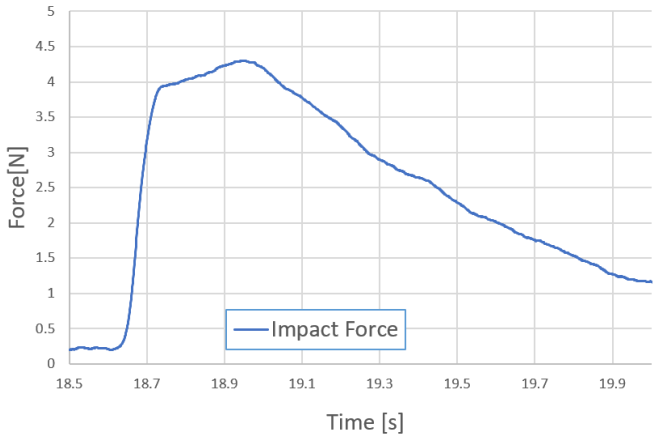

Figure 5. 46: Impact force response from Test 21, illustrated by video recordings in Figure 5. 47.

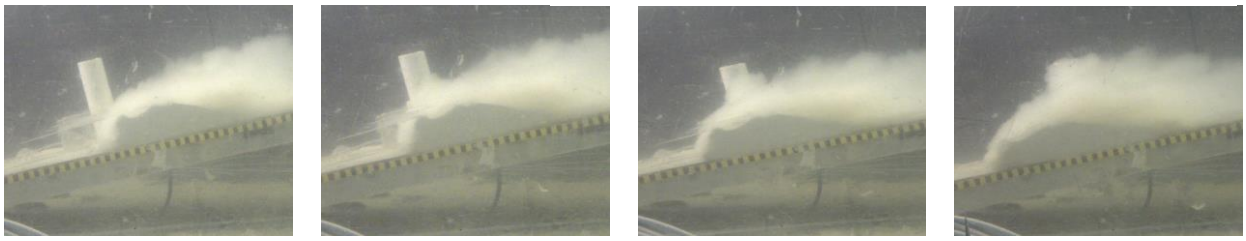

Figure 5. 47: Model slide and impact pile interaction for Test 21, load response is presented in Figure 5. 46.

The shape of the impact force, also called total drag force, curve reflects in many ways the slide geometry. By ignoring the turbidity around and behind the slide body, a certain slide formation can be recognized, showcasing a steep front and declining body behind. As the flow collides, the response is striking. This may explain a homogenous response indicating a volume to force response relation. The impact force response considered in this study is the peak force measured, often represented by the flow head. This peak force is normally considered as the most crucial when submarine constructions are suddenly impacted (Zakeri, 2008). The slurry flow passing the impact cylinder seemed unaffected regarding head velocity unlike the coherency, which seemed affected by disintegration from the impact.

The responding impact force for each conducted flume experiment is presented in Figure 5. 48 (a). Together with investigating the change of flow and impact behavior for increased water content, the effect of initial material state and slope angle was studied. Observations indicates a distinct trend for max impact force related to water content. As the water content decreases and flow coherency increases, the responding max impact force increases. It shows that experiments holding remolded material exhibits an increased force compared to consolidated material for 18° slope.

For experiments conducted on 12° slope, no such trend can be observed as the material response of remolded and consolidated samples alternates.

The impact forces are fundamentally a result of complex interactions between soil strength, slide mass, volume and plug size, and velocity. By studying Figure 5. 48 (b) and (c) and the established dependency towards remolded shear strength with increased water content from Figure 5. 28, the effect of these interaction can be better understood. Figure 5. 48 (b) displays the relationship between steady state velocity and water content, while (c) shows the discharge volume in relation to water content, and as laboratory studies showed, we experience a radical soil strength decrease with increased water while the soil density decreases.

It can be observed a quite flat trend regarding the steady state velocity for most consolidated and remolded tests in both 12° and 18° slopes. However, considering discharge volume from (c), a greater variation can be observed. Remolded tests exhibit throughout the experiments a greater discharge than consolidated samples, which is reasonable considering the intermolecular effects occurring during consolidation.

With this in mind, the max impact force response in Figure 5. 48 (a) seems fitting. The high impact force response for 18° remolded material can be explained by the high discharge volume. This shows also how volume effects exceeds rheological and intermolecular effects from consolidation.

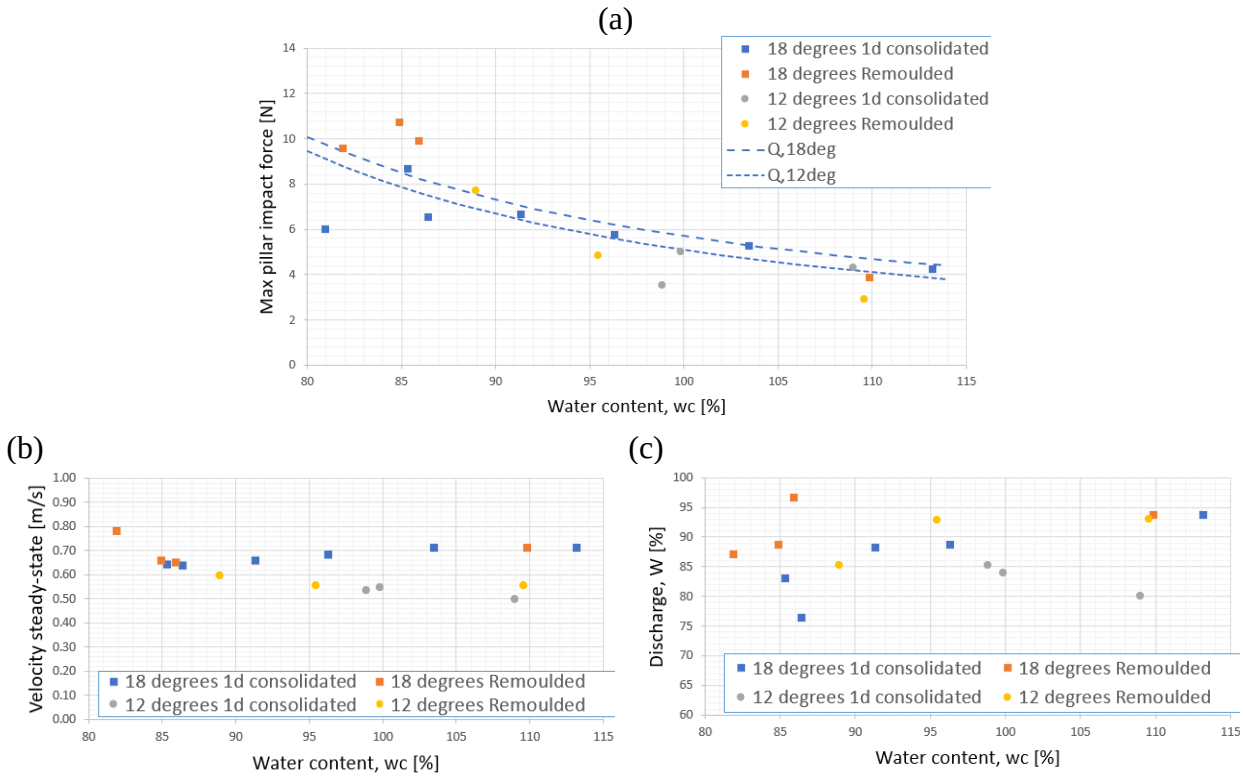

Figure 5. 48: (a) max impact force response in relation to water content for all model tests correlated with theoretical approach based on geotechnical and fluid dynamical components (Q,18deg and Q,12deg). (b) steady state velocity in relaiton to water content, (c) Discharge volume in relation to water content for all experiments.

The dashed lines in Figure 5. 48 shows the theoretical approximations based on a combined geotechnical and fluid dynamical approach in correlation with experimental data. This approach introduces 3 components, the stagnation pressure, earth pressure and dynamic pressure. The stagnation pressure presents the slide-pile interaction and the pressure caused by the inherent material strength. This mechanism is similar to the T-bar test, where the slide and pile interaction is considered as a failure mechanism based on the bearing capacity. By summing up the contributing forces a comparison between experimental data and theoretical approximation can be made. This relationship resemblance a good agreement between the experimental tests and theoretical approximation as the material composition changes.

Drag force and Reynolds number

The effects of the steady state velocity and Reynolds number on the drag force were further investigated. Figure 5. 49 (a) presents the relation between steady state velocity and drag force, F_D, characterized by water content, and (b) presents the effects of water content on drag force, where 18 ° slope is characterized by squares and 12° slope is characterized as circles.

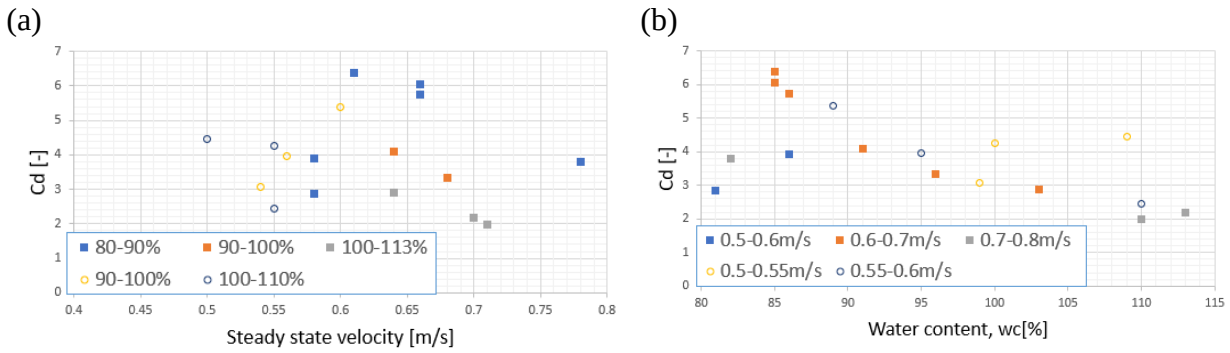

Figure 5. 49: (a) Effects of velocity on drag force, 18° slope represented as squares and 12° represented as circles. (b) Effects of water content on drag force, 18° slope represented as squares and 12° represented as circles.

It can be observed that the effect of velocity is much less significant than the effect of water content. Considering the idea of viscous or dynamic flow, the force should be proportional to the velocity squared. However, considering the dynamic pressure as one of the contributing components regarding the impact response, we can see the proportion of the viscous effects from the slide impact. Considering that the dynamic effect is nearly neglectable, this tells us that the drag force in clay is cohesive, furthering the claim that the inherent rheology is important in evaluating the slide impact response. This observation is in good agreement with the findings from Towhata & Alhussaini (1988).

The total drag force exerted by the slide material and water flow on the impact pile surface can be expressed in relation to the Reynolds number. This is presented in Figure 5. 50 as a semi logarithmic presentation. As the non-Newtonian Reynolds number is rate dependent, a reference shear stress reflecting the slide shear rate must be established. The slide interactions between slide material and impact pile can be recreated through the T-bar. By using the established penetration

rate to shear rate relationship from Eq. 5.1, an approximated shear rate can be found from the steady state velocity. The pile diameter is 54mm and considering the range of steady state velocities for both 18° and 12° slope ranging between 0.5-0.8m/s, shear strain rates between 13.8-22.2s^{-1} are representative. Compared to the strain rate study from conducted soil investigation (see chapter 5.1.7) this range induces small changes in the soil response. Hence, correlated shear stresses, τ, for various water contents are established through T-bar experiments on a strain rate of 11.25s^{-1}.

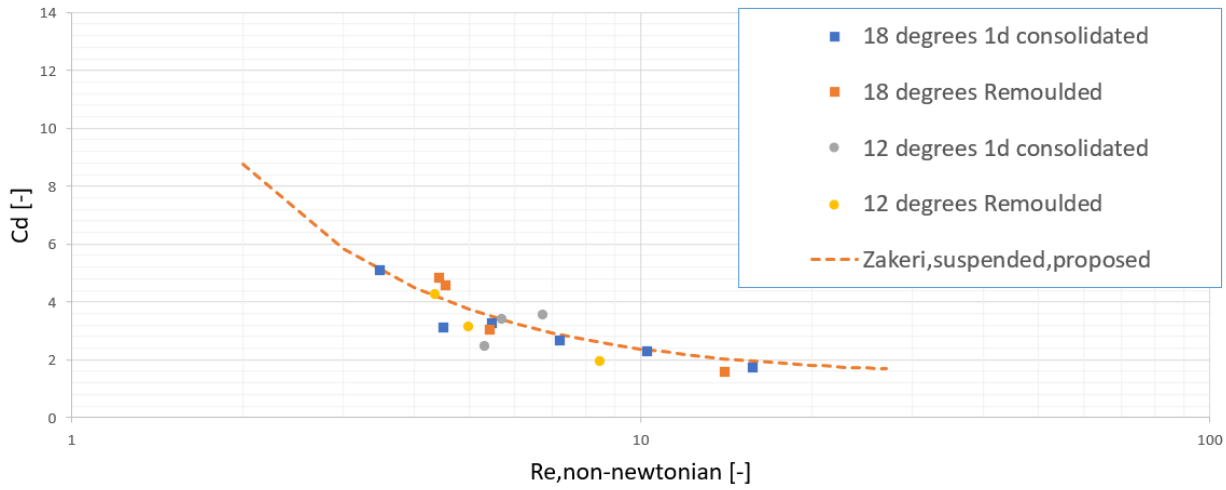

Figure 5. 50:Drag coefficient, C_D, vs non-Newtoninan Reynolds number for all model tests this is plotted against Zakeri et al. (2009) findings on a suspended pipe

The dependency of the drag force, C_d, on the Reynold number has been investigated by numerous authors (Liu et al., 2015; Yin & Rui, 2018; Zakeri et al., 2008). Zakeri et al. (2008) proposed a $C_d - Re$ relationship based on experimental and numerical data for suspended pipelines. This proposed relation can be obtained as:

$$C_d = 1.4 + \frac{17.5}{Re_{non-Newtonian}^{1.25}} \tag{5.5}$$

which can be observed as the orange dashed "Zakeri"-line in Figure 5. 50. In case of the cylindrical impact pile, the experimental results and suggested relation from Zakeri et al. (2008) yield a strong correlation for drag coefficients at established Reynolds number. This can be observed for the experimental results at both 18° and 12° slopes, suggesting that Zakeri et al. (2008) formulation on drag coefficient relation to non-Newtonian Reynolds number for suspended pipes may also be applicable for freestanding cylinders. These findings suggest a similar impact and flow around mechanism for a suspended pipeline and freestanding cylinder, further validating the acquired results.

Impact flow mechanism and limitations

The total drag force, F_D, on an indulged cylinder or pipeline immersed in a flow is resultant to the summarized shear stress and pressure stress distributions. This force can vary in magnitude on the cylinder surface as it contributes to the drag coefficient, C_d, see Eq. 2.22. For variations in the shear stress distribution, this can be explained through a boundary layer immediately outside the pipe surface, illustrated in Figure 5. 51. Inside this zone, viscous effects can be considered as dominant compared to outside, where they are considered less important (Zakeri et al., 2009). The assumption, made by converting the velocity to shear strain rate based on T-bar findings, treats the impact material flowing outside the boundary layer as shear dissuaded as the flow behaves as a plug.

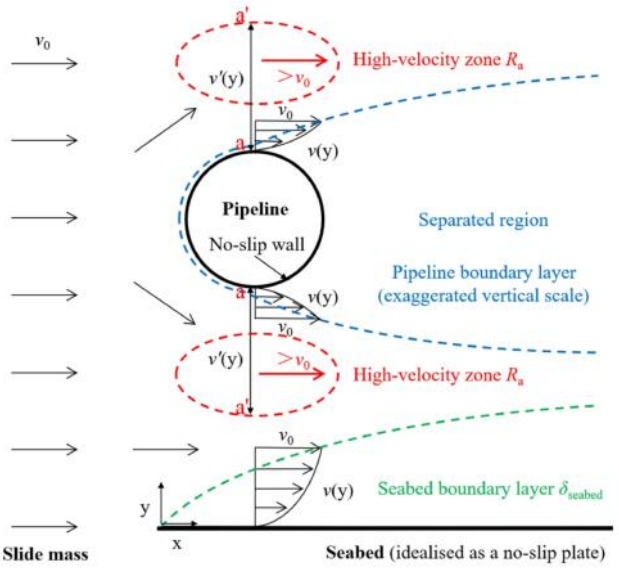

Figure 5. 51:Flow velocity characteristics around a pipeline during slide mass-pipe interaction (Ning et al., 2021)

This separated region defined by the boundary layer could not be observed for the flume experiments. As the impact cylinder was placed perpendicular in the middle of the flume, no video recordings could observe the flow mechanism from above. This proposed a challenge regarding flow behavior during impact as the horizontally placed cameras cannot capture these elements, see Figure 5. 47. Hence, effects presented by the boundary layer cannot be evaluated, this further includes the size of this separated region.

6. Conclusion and Further Work

6.1 Conclusion

This thesis has investigated the submarine slide behavior of clay rich slurries from initiation until impact or deposition, and further explored the impact force response on cylindrical impact pile through 21 experimental small-scale submarine slide tests. Geotechnical and rheological properties of subjected model clay have been retrieved through a substantial soil investigation, consisting of fall cone, viscometer, T-bar, DSS and cyclic triaxial tests, and further used to understand and describe the flow and impact behavior of conducted flume tests. To demonstrate a link to field conditions, the slide and impact behavior has been characterized through dimensionless number as well as that rheological and geotechnical properties of artificial model clay and real clay has been compared.

The material composition and strength evolution, spanning from slide initiation to slide development and flow behavior, extends from the in-situ material state, applicable for the geotechnical domain, until flow behavior and strength magnitudes related to fluid dynamics. The laboratory experiments conducted through the soil investigation has been used based on their application to exploit the strength evolution over a wide range of water contents, spanning from solid to liquid regions. The findings showed a material behavior which could be described within the soil mechanics framework resulting in 6 power function capturing the strength paths based on viscometer, fall cone and T-bar tests for kaolin and BF clay. These power functions represent the strength evolution with increased LI which is made up of two constants unique for the represented material and strain rate. The LI constitutes a normalized water content parameter based on Atterberg limits, which has proven to be a suitable normalization when comparing kaolin and BF clay. However, it can be observed from conducted laboratory tests that the investigated LI range is somewhat unequal for kaolin and BF clay, with kaolin spanning from LI: $0.82 - 3.05$ and BF clay spanning from LI: $0.21 - 1.62$ (including DSScy).

The Herschel Bulkley model is approximated for viscometer, T-bar and DSScy tests. This explores the strain rate behavior ranging between 0.00025-247s^{-1} and captures the non-linearities related to shear thinning fluids well. The non-Newtonian shear thinning flow curves are established through algebraic operations based on best fit estimates for the consistency parameter, *K,* and curvature exponent, *n.* Trends can only be found for both *K* and *n* with increased LI within each laboratory test, moving outside this domain, the behavior starts alternating. The yield stress, τ_y, has been approximated through fall cone and T-bar investigations due to the unphysical approach of the Herschel-Bulkley method. The results exhibit a significant relationship which is captured through 3 power functions on the same form as for the remolded strength evolution.

Interpretation of the strain rate dependency has been carefully considered when comparing results from various laboratory experiments. The importance of recognizing the relative induced strain rate applied and relating behavior for specific shear mechanism has been pointed out and adjusted. The material rate dependency proves to be substantial for plastic state for both kaolin and BF clay, as the LI increases this effect decreases, almost becoming neglectable. However, the rate effects

are more substantial for kaolin compared to BF clay despite being small. The strength behavior related to water dominance has been pointed out and can be further recognized for the flume model experiments.

The model slides were investigated for kaolin at various water contents ranging between 80-113% using 2 slope angles, namely 12° and 18°. In total, 3 experiments were completed investigating slide runout, while 18 experiments were completed investigating impact force responses. For lower water content, the flow characteristics exhibited either strong or moderately coherent flow. As the water content increased the flow turbidity increased displaying characteristics of a weakly coherent flow. The early phase remolding can be identified in almost all model tests. However, this effect is more prominent for steeper slopes and can be further explained due to the triggering mechanism and model flume design. A thin water layer, identified as hydroplaning, intrudes underneath the flow head after remolding and provides an efficient lubrication layer as steady flow is established. This effect was observed through video recordings and velocity profiles for all experiments and further quantified and compared with literature. Some model tests experienced necking, an internal velocity variation leading to stretching and in some cases detachment, as only parts of the slide materials were sustained by hydroplaning. All material behavior and relating effects are in agreement with the findings from the soil investigation, as the yield stress and inherent shear strength of clay slurries shows a dramatic dependency towards water content.

As only 3 runout experiments were conducted, any distinct pattern is hard to determine. However, the conducted tests exhibit a clear relation towards clay rheology, hydroplaning and volume effects, where increased water content and greater discharge volume implies longer runout distance as long as hydroplaning occurs. It is worth noting that literature points out a dependency between hydroplaning and rigid behavior of slide material, implying that for very liquid slurries hydroplaning will not occur as the material transforms into a turbidity flow.

The impact forces were analyzed through a fluid dynamic approach using the rheological properties to establish the non-Newtonian Reynolds number. The measured impact force response corresponds to the drag force and exhibits a greater dependency towards water content and discharge volume than velocity. It was found that the slide-impact pile collision exerted similar failure mechanism as T-bar tests. Hence, a conversion from velocity to strain rate could be established the same way as for T-bar. Finally, the impact drag force obtained from the model experiments were non-dimensionalized and analyzed through the drag coefficient, C_D, and presented in relation to the Reynolds number. The Re-C_D curves are in good agreement with the Zakeri et al. (2009) findings, suggesting that Zakeri et al. (2008) formulation for suspended pipes may also be applicable for freestanding cylinders.

As a part of establishing a numerical tool for simulating submarine landslides and impact forces, this study remains fundamental for incorporating the submarine flow characteristics and the related material dependency regarding water intrusion, heavy remolding, strain rates and strength deterioration. By establishing a material model, the mechanical processes related to weakening of layers, slide initiation, flow characteristics and impact response for various material compositions and slope angels can be simulated, predicting the potential of future slide events and its consequences.

6.2 Further Work

This study has completed a comprehensive soil and model slide investigation. A substantial amount of laboratory tests has highlighted the intent behavior, describing the flow characteristics as well as obtaining a material model for numerical simulations. However, some parts of the model slide investigation remain yet to be completely understood. This can be summarized into:

To obtain a better understanding of dynamic and viscous behavior of the soil – impact pile interactions and relating boundary layer, further investigations with improved camera footage highlighting this zone should be conducted. By getting a visual footage of the material interaction and flow behavior in the boundary zone, flow characteristics from numerical modelling can be compared to video recordings for further improvement. It is also convenient to reinforce offshore structure against highly viscous submarine slides in such zones due to the interaction with water (and not slide material), making a good understanding of the dynamic and viscous effects in this zone of great interest.

A better understanding regarding the runout characteristics and distance can be further considered as important. Determining runout patterns and elements affecting the runout distance based on 3 slide investigations is insufficient. Similar investigations should also include variating slope inclination and deposition areas. This implies also a better visual understanding of the flow characteristics when the slope angle changes between the runout channel and deposition channel.

7. References

Adamson, M. (2017). *Flow Behaviour of Fine-Grained Soils*. https://ntnuopen.ntnu.no/ntnu-xmlui/handle/11250/2458152

Ashenafi, L. (2020). *Model testing of a screen-type countermeasure for debris-flow hazard reduction along highway-E39*.

Astarita, G. (1990). Letter to the Editor: The engineering reality of the yield stress. *Journal of Rheology*, *34*(2), 275–277. https://doi.org/10.1122/1.550142

Bjerrum, L. (1954). Geotechnical Properties of Norwegian Marine Clays. *Géotechnique*, *4*(2), 49–69. https://doi.org/10.1680/geot.1954.4.2.49

Blasio, F. V. D., Engvik, L. E., & Elverhøi, A. (2006). Sliding of outrunner blocks from submarine landslides. *Geophysical Research Letters*, *33*(6). https://doi.org/10.1029/2005GL025165

Bohlin88BV. (2010). *Technical Manual for the BOHLIN VISCO 88BV*. https://mail.google.com/mail/u/0/#search/erik.sorlie%40ntnu.no?projector=1

Boukpeti, N., & White, D. (2016). Interface shear box tests for assessing axial pipe–soil resistance. *Géotechnique*, *67*, 1–13. https://doi.org/10.1680/jgeot.15.P.112

Boukpeti, N., White, D. j., Randolph, M. f., & Low, H. e. (2012). Strength of fine-grained soils at the solid–fluid transition. *Géotechnique*, *62*(3), 213–226. https://doi.org/10.1680/geot.9.P.069

Bryn, P., Berg, K., Forsberg, C. F., Solheim, A., & Kvalstad, T. J. (2005). Explaining the Storegga Slide. *Marine and Petroleum Geology*, *22*(1), 11–19. https://doi.org/10.1016/j.marpetgeo.2004.12.003

Carty, W. M. (2001). The Colloidal Nature of Kaolinite. I *Materials & Equipment/Whitewares: Ceramic Engineering and Science Proceedings* (s. 31–31). John Wiley & Sons, Ltd. https://doi.org/10.1002/9780470294673.ch7

Coussot, P., & Piau, J. M. (1994). On the behavior of fine mud suspensions. *Rheologica Acta*, *33*(3), 175–184. https://doi.org/10.1007/BF00437302

Einav, I., & Randolph, M. F. (2005). Combining upper bound and strain path methods for evaluating penetration resistance. *International Journal for Numerical Methods in Engineering*, *63*(14), 1991–2016. https://doi.org/10.1002/nme.1350

Elverhøi, A., Harbitz, C., Dimikis, P., Mohrig, D., Marl, J., & Parker, G. (2000). On the Dynamics of Subaqueous Debris Flows. *Oceanography*, *13*(3), 109–117. https://doi.org/10.5670/oceanog.2000.20

Fisher, R. V. (1983). Flow transformations in sediment gravity flows. *Geology*, *11*(5), 273–274. https://doi.org/10.1130/0091-7613(1983)11<273:FTISGF>2.0.CO;2

Fitton, T. G., & Seddon, K. D. (2012). *Relating Atterberg limits to rheology* (s. 273–284). Australian Centre for Geomechanics. https://doi.org/10.36487/ACG_rep/1263_23_Fitton

Georgiadis, M. (1991). Landslide Drag Forces on Pipelines. *SOILS AND FOUNDATIONS*, *31*, 156–161. https://doi.org/10.3208/sandf1972.31.156

Graham, J., Crooks, J. H. A., & Bell, A. L. (1983). Time effects on the stress-strain behaviour of natural soft clays. *Géotechnique*, *33*(3), 327–340. https://doi.org/10.1680/geot.1983.33.3.327

Grue, R. H. (2015). Rheological Parameters of Norwegian Sensitive Clays, Focusing on the Herschel-Bulkley Model. *126*. https://ntnuopen.ntnu.no/ntnu-xmlui/handle/11250/2349972

Hampton, M. A. (1972). The role of subaqueous debris flow in generating turbidity currents. *Journal of Sedimentary Research*, *42*(4), 775–793. https://doi.org/10.1306/74D7262B-2B21-11D7-8648000102C1865D

Hansbo, S. (1957). *A new approach to the determination of the shear strength of clay by the fall-cone test*. Royal Swedish Geotechnical Institute.

Hartnik, L. (2021). *E39 Fjord crossing over Bjørnafjorden: The use of kaolin as a model clay for submarine slides*. NTNU.

Henkel, D. J., & Gilbert, G. D. (1952). The effect of the rubber membrane on the measured triaxial compression strength of clay samples. *Geotechnique*, *3*(1), 20–29. Scopus. https://doi.org/10.1680/geot.1952.3.1.20

Hossain, M. S., Hu, Y., Randolph, M. F., & White, D. J. (2005). Limiting cavity depth for spudcan foundations penetrating clay. *Géotechnique*, *55*(9), 679–690. https://doi.org/10.1680/geot.2005.55.9.679

Ilstad, T., De Blasio, F. V., Elverhøi, A., Harbitz, C. B., Engvik, L., Longva, O., & Marr, J. G. (2004). On the frontal dynamics and morphology of submarine debris flows. *Marine Geology*, *213*(1), 481–497. https://doi.org/10.1016/j.margeo.2004.10.020

Imran, J., Parker, G., Locat, J., & Lee, H. (2001). 1D Numerical Model of Muddy Subaqueous and Subaerial Debris Flows. *Journal of Hydraulic Engineering*, *127*(11), 959–968. https://doi.org/10.1061/(ASCE)0733-9429(2001)127:11(959)

Irgens, F. (2014). *Rheology and Non-Newtonian Fluids*. Springer International Publishing. https://doi.org/10.1007/978-3-319-01053-3

Jeong. (2013). The viscosity of fine-grained sediments: A comparison of low- to medium-activity and high-activity clays. *Engineering Geology*, *154*, 1–5. Scopus. https://doi.org/10.1016/j.enggeo.2012.12.006

Jeong, S., Locat, J., Leroueil, S., & Malet, J.-P. (2010). *Rheological properties of fine-grained sediment: The roles of texture and mineralogy*. https://cdnsciencepub.com/doi/10.1139/T10-012

Jeong, S. W., Locat, J., & Leroueil, S. (2012). The Effects of Salinity and Shear History on The Rheological Characteristics of Illite-Rich and Na-Montmorillonite-Rich Clays. *Clays and Clay Minerals*, *60*(2), 108–120. https://doi.org/10.1346/CCMN.2012.0600202

Jeong, S. W., Locat, J., & Leroueil, S. (2015). Geotechnical and Rheological Characteristics of Saguenay Fjord Sediments Near the Transition from Solid to Liquid. *Marine Georesources & Geotechnology*, *33*(3), 239–252. https://doi.org/10.1080/1064119X.2013.848252

Jung, B., & Biscontin, G. (2006). Modeling of Strain Rate Effects on Clay in Simple Shear. I *GeoCongress 2006: Geotechnical Engineering in the Information Technology Age* (Bd. 2006, s. 6). https://doi.org/10.1061/40803(187)161

Koumoto, T., & Houlsby, G. (2001). Theory and practice of the fall cone test. *Geotechnique*, *51*, 701–712. https://doi.org/10.1680/geot.51.8.701.40475

Kundu, P. K. (2004). *Fluid mechanics* (3rd ed.). Elsevier Academic Press.

Kvalstad, T. J., Andresen, L., Forsberg, C. F., Berg, K., Bryn, P., & Wangen, M. (2005). The Storegga slide: Evaluation of triggering sources and slide mechanics. *Marine and Petroleum Geology*, *22*(1), 245–256. https://doi.org/10.1016/j.marpetgeo.2004.10.019

Lefebvre, G., & Pfendler, P. (1996). Strain Rate and Preshear Effects in Cyclic Resistance of Soft Clay. *Journal of Geotechnical Engineering*, *122*(1), 21–26. https://doi.org/10.1061/(ASCE)0733-9410(1996)122:1(21)

Liu, J., Tian, J., & Yi, P. (2015). Impact forces of submarine landslides on offshore pipelines. *Ocean Engineering*, *95*. https://doi.org/10.1016/j.oceaneng.2014.12.003

Locat, J., & Lee, H. J. (2005). Subaqueous debris flows. I M. Jakob & O. Hungr (Red.), *Debris-flow Hazards and Related Phenomena* (s. 203–245). Springer. https://doi.org/10.1007/3-540-27129-5_9

Lozano, J.-M., & Sánchez-Silva, M. (2019). Improving decision-making in maintenance policies and contract specifications for infrastructure projects. *Structure and Infrastructure Engineering*, *15*(8), 1087–1102. Scopus. https://doi.org/10.1080/15732479.2019.1581818

Luckham, P. F., & Rossi, S. (1999). The colloidal and rheological properties of bentonite suspensions. *Advances in Colloid and Interface Science*, *82*(1), 43–92. https://doi.org/10.1016/S0001-8686(99)00005-6

Lunne, T., Andersen, K., Low, H. E., Randolph, M., & Sjursen, M. (2011). Guidelines for offshore in situ testing and interpretation in deepwater soft clays. *Canadian Geotechnical Journal*, *48*, 543–556. https://doi.org/10.1139/t10-088

Lunne, T., Berre, T., Andersen, K., Strandvik, S., & Sjursen, M. (2011). Effects of sample disturbance and consolidation procedures on measured shear strength of soft marine Norwegian clays. *Canadian Geotechnical Journal*, *43*, 726–750. https://doi.org/10.1139/t06-040

Lunne, T., Randolph, M., Chung, S. F., Andersen, K. H., & Sjursen, M. (2005). Comparison of cone and T-bar factors in two onshore clay sediments: Comparison of cone and T-bar factors in two onshore clay sediments. *Proceedings of the International Symposium on Frontiers in Offshore Geotechnics*, *n/a*, 981–989.

Major, J. J., & Pierson, T. C. (1992). Debris flow rheology: Experimental analysis of fine-grained slurries. *Water Resources Research*, *28*(3), 841–857. https://doi.org/10.1029/91WR02834

Martin, C. M., & Randolph, M. (2006). Upper-bound analysis of lateral pile capacity in cohesive soil. *Géotechnique*, *56*(2), 141–145. https://doi.org/10.1680/geot.2006.56.2.141

Martinez, A., & Stutz, H. (2018). Rate effects on the interface shear behaviour of normally and over-consolidated clay. *Géotechnique*, *69*. https://doi.org/10.1680/jgeot.17.p.311

Masson, D. g, Harbitz, C. b, Wynn, R. b, Pedersen, G., & Løvholt, F. (2006). Submarine landslides: Processes, triggers and hazard prediction. *Philosophical Transactions of the Royal Society A: Mathematical, Physical and Engineering Sciences*, *364*(1845), 2009–2039. https://doi.org/10.1098/rsta.2006.1810

Mayne, P. W. (2013). *Evaluating Yield Stress of Soils From Laboratory Consolidation and in-Situ Cone Penetration Tests*. 405–419. https://doi.org/10.1061/9780784412770.027

Meyer, V. (2015). *Frontiers in Offshore Geotechnics III*. CRC Press.

Mohrig, D., Ellis, C., Parker, G., Whipple, K. X., & Hondzo, M. (1998). Hydroplaning of subaqueous debris flows. *GSA Bulletin*, *110*(3), 387–394. https://doi.org/10.1130/0016-7606(1998)110<0387:HOSDF>2.3.CO;2

Mohrig, D., & Marr, J. (2003). Constraining the efficiency of turbidity current generation from sumarine debris flows and slides using laboratory experiments. *Marine and Petroleum Geology - MAR PETROL GEOL*, *20*, 883–899. https://doi.org/10.1016/j.marpetgeo.2003.03.002

Mojid, Md. A. (2011). Diffuse Double Layer (DDL). I J. Gliński, J. Horabik, & J. Lipiec (Red.), *Encyclopedia of Agrophysics* (s. 213–214). Springer Netherlands. https://doi.org/10.1007/978-90-481-3585-1_41

Nanda, Sivakumar, Hoyer, & Gavin. (2017). *Effects of Strain Rates on the Undrained Shear Strength of Kaolin*. https://www.astm.org/gtj20160101.html

NGI. (2019a). *E39 Bjørnafjorden; DATA INTERPRETATION AND EVALUATION OF REPRESENTATIVE GEOTECHNICAL PARAMETERS*.

NGI. (2019b). *E39 Bjørnafjorden; Field Operationsand and Premilinary Results*.

NGI. (2019c). *E39 Bjørnafjorden; Measured and Derived Geotechnical Parameters and Final Results*.

NS 8001. (1982). Geoteknisk prøving - Laboratoriemetoder -støtflytegrensen. https://www.standard.no/no/Nettbutikk/produktkatalogen/Produktpresentasjon/?ProductID=135186

NS 8013. (1982). Eurokode 7: Geoteknisk prosjektering - Del 2: Regler basert på grunnundersøkelser og laborotorieprøver. https://www.standard.no/no/Nettbutikk/produktkatalogen/Produktpresentasjon/?ProductID=135194

NS 8015. (1988). Eurokode 7: Geoteknisk prosjektering - Del 2: Regler basert på grunnundersøkelser og laboratorieprøver https://www.standard.no/nettbutikk/produktkatalogen/produktpresentasjon/?ProductID=135196

NS-EN ISO 17892-4. (2016). Geotekniske felt- og laboratorieundersøkelser - Laboratorieprøving av jord - Del 4: Bestemmelse av kornstørrelsesfordeling https://www.standard.no/no/Nettbutikk/produktkatalogen/Produktpresentasjon/?ProductID=877569

NS-EN ISO 17892-8. (2018). Geotekniske felt- og laboratorieundersøkelser - Laboratorieprøving av jord - Del 8: Ukonsolidert udrenert treaksialprøving. https://www.standard.no/no/Nettbutikk/produktkatalogen/Produktpresentasjon/?ProductID=978571

NS-EN ISO 17892-9. (2018). Geotekniske felt- og laboratorieundersøkelser - Laboratorieprøving av jord - Del 9: Konsolidert treaksial trykkprøving av mettet jord. https://www.standard.no/no/Nettbutikk/produktkatalogen/Produktpresentasjon/?ProductID=985112

NS-EN ISO 17892-12. (2018). Geotekniske felt- og laboratorieundersøkelser - Laboratorieprøving av jord - Del 12: Bestemmelse av flyte- og plastisitetsgrenser https://www.standard.no/no/Nettbutikk/produktkatalogen/Produktpresentasjon/?ProductID=997238

NTNU. (2015). *Geotechnics Field and Laboratory Investigations*. Norwegian University of Science and Technology.

Nyquist, & Shannon. (1949). *Communication in the Presence of Noise*.

Pazwash, H., & Robertson, J. M. (1975). Forces on Bodies in Bingham Fluids. *Journal of Hydraulic Research*, *13*(1), 35–55. https://doi.org/10.1080/00221687509499719

Perrot, A., Rangeard, D., & Levigneur, A. (2016). Linking rheological and geotechnical properties of kaolinite materials for earthen construction. *Materials and Structures*, *49*(11), 4647–4655. https://doi.org/10.1617/s11527-016-0813-9

Quinn, T. a. C., & Brown, M. J. (2011). Effect of strain rate on isotropically consolidated kaolin over a wide range of strain rates in the triaxial apparatus. *Proceedings of the Fifth International Symposium on Deformation Characteristics of Geomaterials*, 607–613. https://doi.org/10.3233/978-1-60750-822-9-607

Randolph, M. F., Hefer, P. A., Geise, J. M., & Watson, P. G. (1998). *Improved seabed strength profiling using T-bar penetrometer*. https://www.osti.gov/etdeweb/biblio/695334

Randolph, M. F., & Houlsby, G. T. (1984). The limiting pressure on a circular pile loaded laterally in cohesive soil. *Géotechnique*, *34*(4), 613–623. https://doi.org/10.1680/geot.1984.34.4.613

Randolph, M. F., & White, D. J. (2012). Interaction forces between pipelines and submarine slides—A geotechnical viewpoint. *Ocean Engineering*, *48*, 32–37. https://doi.org/10.1016/j.oceaneng.2012.03.014

Ranekka, K., Andersson-Sköld, Y., Hultén, C., Larsson, R., Leroux, V., & Dahlin, T. (2004). *Quick clay in Sweden*.

Sahdi, F., Gaudin, C., Tom, J., & Tong, F. (2019). Mechanisms of soil flow during submarine slide-pipe impact. *Ocean Engineering*, *186*. https://doi.org/10.1016/j.oceaneng.2019.05.061

Schramm, G. (1994). *A Practical Approach to Rheology and Rheometry*. 291.

Shimobe, S., & Spagnoli, G. (2020). Relationships between undrained shear strength, liquidity index, and water content ratio of clays. *Bulletin of Engineering Geology and the Environment*, *79*(9), 4817–4828. https://doi.org/10.1007/s10064-020-01844-5

Skempton, A. W. (1953). The Colloidal ?Activity? Of Clays. I *SELECTED PAPERS ON SOIL MECHANICS* (Bd. 1–0, s. 60–64). Thomas Telford Publishing. https://doi.org/10.1680/sposm.02050.0009

Statens vegvesen. (2018). *Håndbok 016 Geoteknikk i vegbygging*. 624.

SVV. (2019). K12 – Marine geotechnical design. I *90* [Report]. Statens vegvesen. https://vegvesen.brage.unit.no/vegvesen-xmlui/handle/11250/2660411

SVV. (2021). *E39 Stord–Os (Hordfast)*. Statens vegvesen. https://www.vegvesen.no/vegprosjekter/europaveg/e39stordos/

Saasen, A., & Ytrehus, J. (2019). *Viscosity Models for Drilling Fluids: Viscosity Parameters and Their Use*. https://doi.org/10.1115/OMAE2019-96595

Takahashi, T. (1981). Debris Flow. *Annual Review of Fluid Mechanics*, *13*(1), 57–77. https://doi.org/10.1146/annurev.fl.13.010181.000421

Thanh Duong, N., & Van Hao, D. (2020). Consolidation Characteristics of Artificially Structured Kaolin-Bentonite Mixtures with Different Pore Fluids. *Advances in Civil Engineering*, *2020*, e8856404. https://doi.org/10.1155/2020/8856404

Towhata, I., & Alhussaini. (1988). *LATERAL LOADS ON OFFSHORE STRUCTURES EXERTED BY SUBMARINE MUDFLOWS*. https://www.jstage.jst.go.jp/article/sandf1972/28/3/28_3_26/_article

ur Rehman, Z., Khalid, U., Farooq, K., & Mujtaba, H. (2018). On yield stress of compacted clays. *International Journal of Geo-Engineering*, *9*. https://doi.org/10.1186/s40703-018-0090-2

Wazer, J. R. V. (1963). *Viscosity and Flow Measurement: A Laboratory Handbook of Rheology*. Interscience Publishers.

White, D. j., Gaudin, Boylan, & Zhou. (2010). *Interpretation of T-bar penetrometer tests at shallow embedment and in very soft soils*. https://cdnsciencepub.com/doi/10.1139/T09-096

White, D., & Randolph, M. (2008). Upper-bound yield envelopes for pipelines at shallow embedment in clay. *Geotechnique*, *58*, 297–301. https://doi.org/10.1680/geot.2008.58.4.297

Wichtmann, T., & Triantafyllidis, T. (2018). Monotonic and cyclic tests on kaolin: A database for the development, calibration and verification of constitutive models for cohesive soils with focus to cyclic loading. *Acta Geotechnica*, *13*(5), 1103–1128. https://doi.org/10.1007/s11440-017-0588-3

Yafrate, N., DeJong, J., DeGroot, D., & Randolph, M. (2009). Evaluation of Remolded Shear Strength and Sensitivity of Soft Clay Using Full-Flow Penetrometers. *Journal of Geotechnical and Geoenvironmental Engineering*, *135*(9), 1179–1189. https://doi.org/10.1061/(ASCE)GT.1943-5606.0000037

Yin, M., & Rui, Y. (2018). Laboratory study on submarine debris flow. *Marine Georesources & Geotechnology*, *36*(8), 950–958. https://doi.org/10.1080/1064119X.2017.1402975

Zakeri, A. (2008). Review of State-Of-The-Art: Drag Forces on Submarine Pipelines and Piles Caused by Landslide or Debris Flow Impact. *Journal of Offshore Mechanics and Arctic Engineering*, *131*(1). https://doi.org/10.1115/1.2957922

Zakeri, A., Høeg, K., & Nadim, F. (2008). Submarine debris flow impact on pipelines — Part I: Experimental investigation. *Coastal Engineering*, *55*(12), 1209–1218. https://doi.org/10.1016/j.coastaleng.2008.06.003

Zakeri, A., Høeg, K., & Nadim, F. (2009). Submarine debris flow impact on pipelines — Part II: Numerical analysis. *Coastal Engineering*, *56*, 1–10. https://doi.org/10.1016/j.coastaleng.2008.06.005

Åhnberg, H., & Larsson, R. (2012). *Strength degradation of clay due to cyclic loadings and enforced deformation*.

Appendix A

Cyclic Triaxial Tests

Method

The cyclic triaxial tests were conducted in the geotechnical lab at NTNU. Such tests had never been conducted on available apparatus before. Therefore, necessary testing routines were established in accordance with lab technicians before experiments were conducted.

An important tool for measuring dynamic- and cyclic soil properties at various strain levels is the cyclic triaxial test (Meyer, 2015). A cylindrical specimen, placed between top and bottom loading plates with a surrounding rubber membrane, is subjected to radial and axial stresses. The difference between axial and radial stress is defined as the deviator stress. During cyclic triaxial testing, the deviatoric stress can be applied cyclically in two various ways, stress- or strained-controlled conditions. For this study, a strain-controlled environment was used.

Equipment

A total of 6 strain-controlled tests with 3 different axial strain rates were conducted for this study (3%/hr, 60%/hr and 1200%/hr). These strain-controlled cyclic triaxial tests were conducted on both BF and kaolin clay, with one test for each speed. For each test 10 cycles were completed, illustrating the cyclic dependency towards remolded shear strength.

A GDS Dynamic Triaxial Testing System (illustrated in A. 1) was used to conduct the tests. The software consisted of operating functions such as advanced loading, which was used for cyclic testing at axial strain rates up to 60%/hr. This program had cyclic loading as an option but was not specially designed for this use. Due to some irregularities in the software, tests with strain rates at 1200%/hr were conducted manually, which meant it was controlled by an operator steering the triaxial apparatus, not a software.

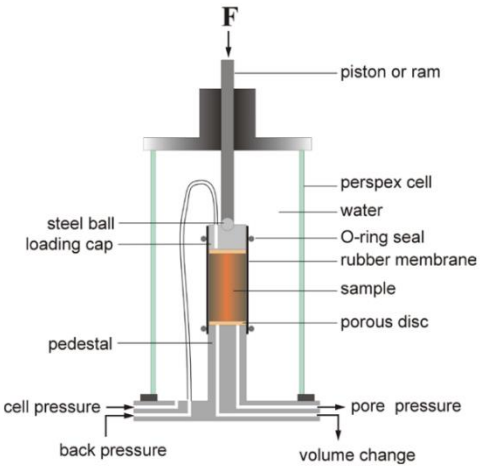

A. 1: Illustration of GDS triaxial apparatus.

Preparation Bjørnafjorden clay

The cyclic triaxial tests on BF clay were conducted from BH-12A 2.10-2.83m and carried out according to *NS-EN ISO 17892-8* (2018). To ensure a good sample quality soil between 2.35 and 2.75m were used for triaxial testing.

Preparation Kaolin clay

For cyclic triaxial tests, the kaolin slurry was pre-consolidated in a 74 mm diameter times 250 mm high Plexiglas cylinder, having an original water content of 100%. This was done on the basis of practical implementation when inserting the sample to the triaxial device. The slurry was pre-consolidated for at least four days. The applied axial loading during the pre-consolidation was applied directly on the surface using gravitational force. Maximum vertical stress was 11 kPa, similarly to the in-situ overburden stress on the BF sample. The pre-consolidated sample ended up having a diameter of $d = 74\ mm$ and a height between $h = 130 - 150mm$.

Afterwards, the clay specimens were trimmed out of centre to fit the triaxial apparatus, meaning $d = 54mm, h = 100mm$. Due to the low strength, sample heights varied between 95mm and 105mm. This was taken account for by the apparatus. Water content was determined through residual mass, low strength of the kaolin clay made it complicated to make precise weight measurements of the whole triaxial specimen. The chosen residual mass for water content was chosen based kaolin studies done by Wichtmann & Triantafyllidis (2018).

Consolidation

Consolidation was applied in similar manor for both kaolin and BF clay. The consolidation stresses for BF clay were determined based on suggested p_0', and K_0' profile from (NGI, 2019c). Challenges with the triaxial apparatus and the very soft test samples made anisotropic consolidation difficult. To avoid anisotropic consolidation and still ensure stress conditions as similar in-situ environment as possible, shallow test samples were used. This meant test samples collected between 2 and 3 meters, with an effective overburden stress $p_0' = 11.5$ kPa and $k_0' > 0.85$. An isotropic consolidation based on the effective overburden stress was considered as good enough under these conditions. However, due to challenges regarding implementation and relating results, it has been speculated that the consolidation was applied in extension circumstances.

Since the kaolin clay is designated as model clay for the BF clay, their soil conditions were designed to be similar. Thus, the same isotropic and effective consolidation stress was chosen for kaolin tests. The consolidation stress with a corresponding backpressure was set to around 200 - 230 kPa ensuring saturation during consolidation of the test.

To verify fully saturated tests before shearing, a beta tests was applied. According to *NS-EN ISO 17892-9* (2018)an attempt to reach a B-value of at least 0.95 should be made for static tests. For cyclic tests, there are no national guidelines. According to NGI (2019c)and Quinn & Brown (2011), a B-value of 0.98 should be reached for cyclic tests, which was also used as a benchmark for this study. Before beta testing, the backpressure was set to around 200 kPa, keeping an effective stress of 11.5 kPa. The test itself was conducted by applying an additional 15 kPa on top the already 211.5 kPa confinement pressure. This was done according to procedures used on very soft clays by NGI on the BF clay.

Shearing

The specimen is sheared at a constant rate of axial strain in an undrained environment. During shearing, the total radial stress is kept constant from the consolidation stage while the total axial

stress is increased in compressions stages and decreased in extension stages. The tests have been performed with a symmetric strain period, having a 10mm amplitude in both compression and extension. To keep undrained conditions, the valves were closed during shearing. Tests were terminated at 10 cycles, which meant a large time difference (0.5h-133h) in time consumptions for given test depending on strain rate.

A. 2: Triaxial properties summarized

Parameter	*Kaolin Clay*			*BF Clay*		
Test id	$K_{1.1.1}$	$K_{2.2.2}$	$K_{3.3.3}$	$BF_{1.1.1}$	$BF_{2.2.2}$	$BF_{3.3.3}$
Velocity (mm/min)	20	1	0.05	20	1	0.05
Frequency (Hz)	0.0083	$4.2 \cdot 10^{-4}$	$2.1 \cdot 10^{-5}$	0.0083	$4.2 \cdot 10^{-4}$	$2.1 \cdot 10^{-5}$
Height (mm)	100	100	100	100	100	100
Amplitude (mm)	10	10	10	10	10	10
Displacement each cycle(mm)	40	40	40	40	40	40
Shear Strain rate(%/hr)	8000	400	20	8000	400	20
Shear *Strain rate* (s^{-1})	0.022	$1.1 \cdot 10^{-3}$	$5.5 \cdot 10^{-5}$	0.022	$1.1 \cdot 10^{-3}$	$5.5 \cdot 10^{-5}$
Number of cycles (N)	10	10	10	10	10	10

Results

Obtained cyclic triaxial results are presented in A. 3, A. 4, A. 5A. 6, A. 7, illustrating challenges and following data processing for each test. A. 3 is a representation of what the triaxial software from NTNU produced of $BF_{2.2.2}$. A. 4 (a) shows corresponding unprocessed data where deviatoric stresses are calculated from initial measurements (load and cell pressure), while (b) presents data processed results for$BF_{2.2.2}$, and A. 4 (c) and (d) shows the equivalent ESP line for unprocessed and processed data. Similarly, A. 5 (a-d) illustrates the corresponding material behavior for 1mm/min kaolin test. A. 6 compares the processed data of $BF_{2.2.2}$and $BF_{1.1.1}$, and A. 7 shows the corresponding ESP path of $BF_{1.1.1}$.

All processed triaxial data is based on the established membrane stiffness with the assumption of impact from both axial and radial effects, see 5.1.5.

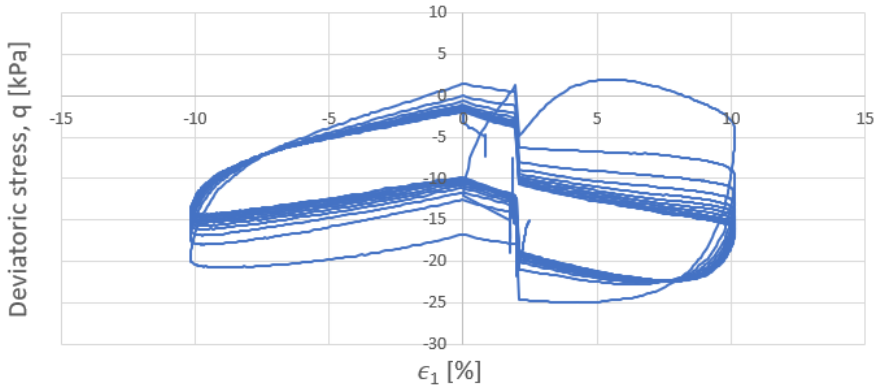

A. 3: $BF_{2.2.2}$

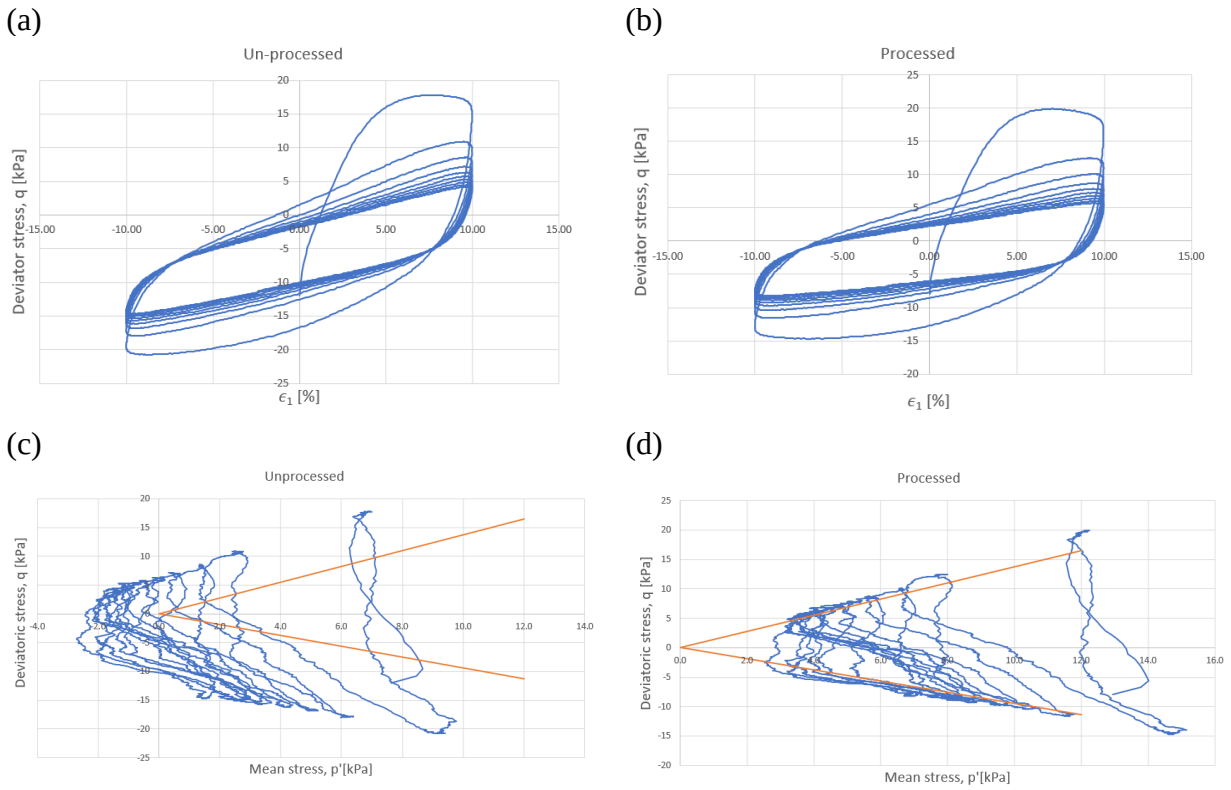

A. 4: Shows $BF_{2.2.2}$. (a-b) Unprocessed and processed hystersis loops. (c) and (d) shows the full effective stress path in a critical state format for unprocessed and processed data.

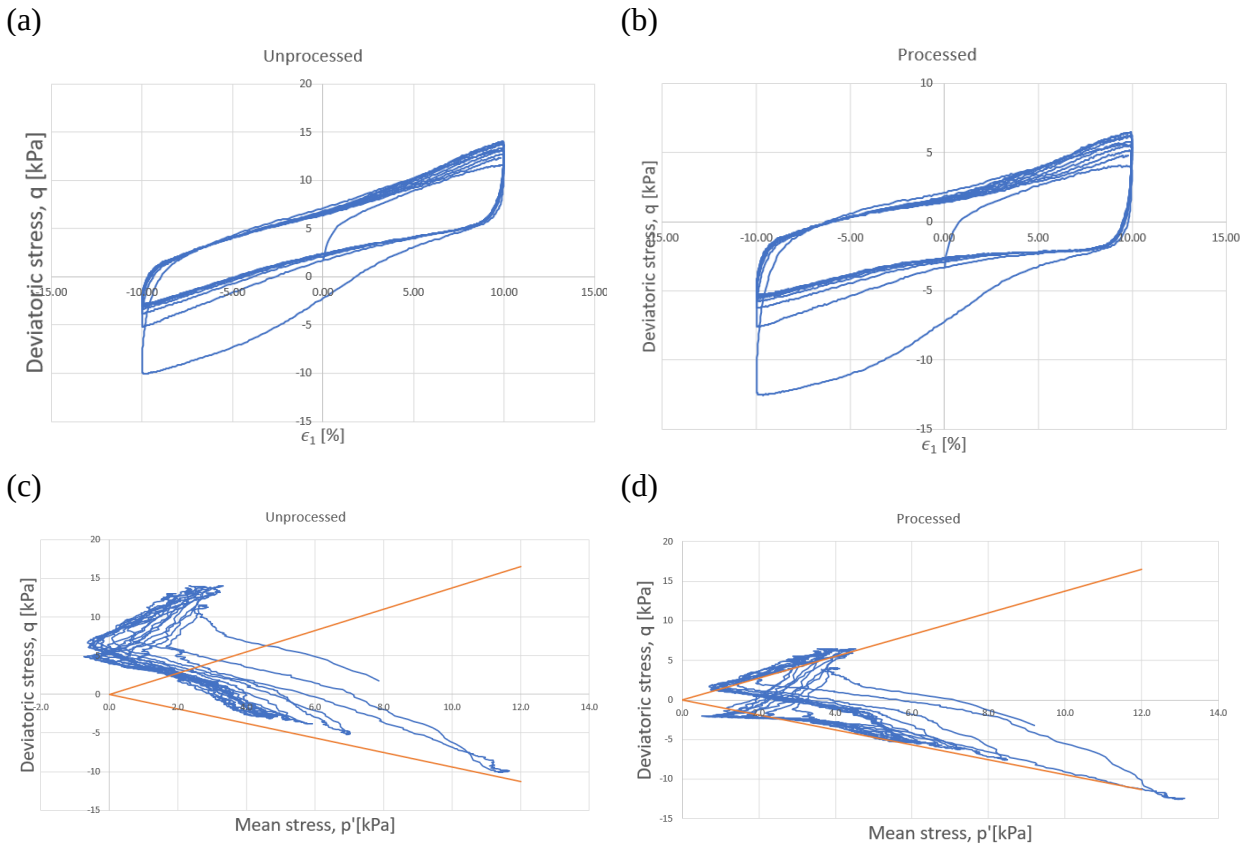

A. 5: Shows $K_{2.2.2}$. (a-b) Unprocessed and processed hystersis loops. (c) and (d) shows the full effective stress path in a critical state format for unprocessed and processed data.

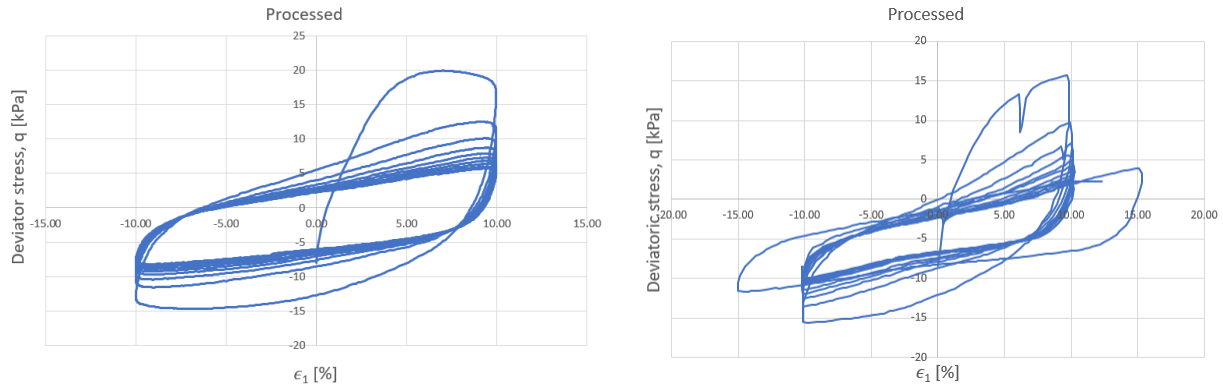

A. 6: Hysteresis loops of $BF_{2.2.2}$ on the left side and $BF_{1.1.1}$ on the right side

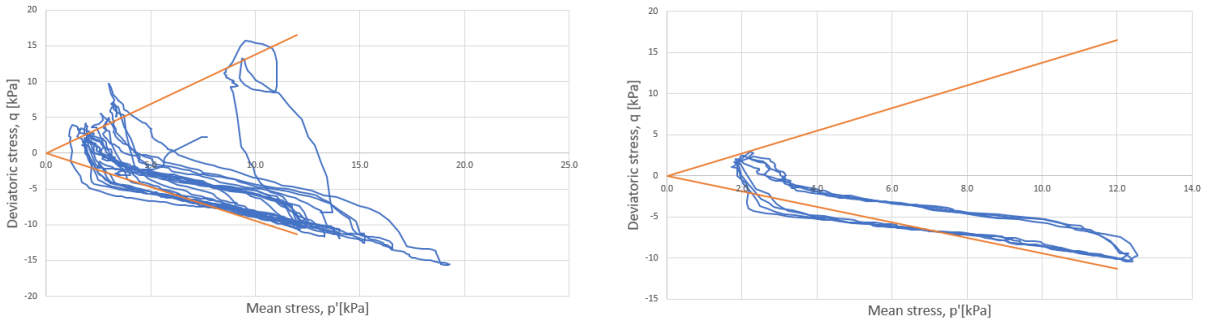

A. 7:Shows $BF_{2.2.2}$. Right side: Full effective stress path in a critical state format. Left side: Last cycles of effective stress path.

Discussion

The cyclic results exhibit a distinct trend having clearly unphysical attributes if we consider correct implementation and $K_0 = 1$ consolidation. However, this trend of offsets results can be justified if we consider that the sample experienced consolidation on the extension side, meaning $K_0 > 1$ for some of the tests. This behavior is prominent for both $K_{2.2.2}$ as the shear strength increases for increased cycling, and $BF_{2.2.2}$ as the strength increases on the extension side for the first cycle. The introduced membrane correction attempts to correct for these effects, as no critical state line can describe this behavior. By correcting for the ESP path, we can acquire a more reasonable behavior. However, these adjustments and explanations are heavily reliant on the adjusted membrane effects, and the assumption that consolidation occurred in extension. Considering the ESP path of $BF_{1.1.1}$ a somewhat peculiar behavior can be observed. The material seems to experience large volume changes (dilatant and contractant behavior) on extension side compared to compression. This behavior is also prominent for the kaolin tests. The strain rate dependency presented in A. 6 shows an increased strength for lower strain rate. This is in direct opposition from the obtained DSScy results and considered as an important reason for not using the cyclic triaxial results in evaluating the rate effects. This behavior can be observed for both processed and unprocessed data.

As the uncertainties concerning implementation, consolidation and general load measurements during testing are so substantial, using these results to capture the material behavior is very difficult. Hence, it has been provided a correction which adjusts for what is considered as disruptive elements. This correction has however its limits leading to an uncertainty regarding the result. This, together with the abnormal rate dependency displayed for both materials, can be considered the principal reason for not including the triaxial tests in the soil investigation. However, it can be noted that the cyclic strength deterioration results for triaxial tests are in good agreement with the DSScy tests.

Appendix B

Cyclic DSS results

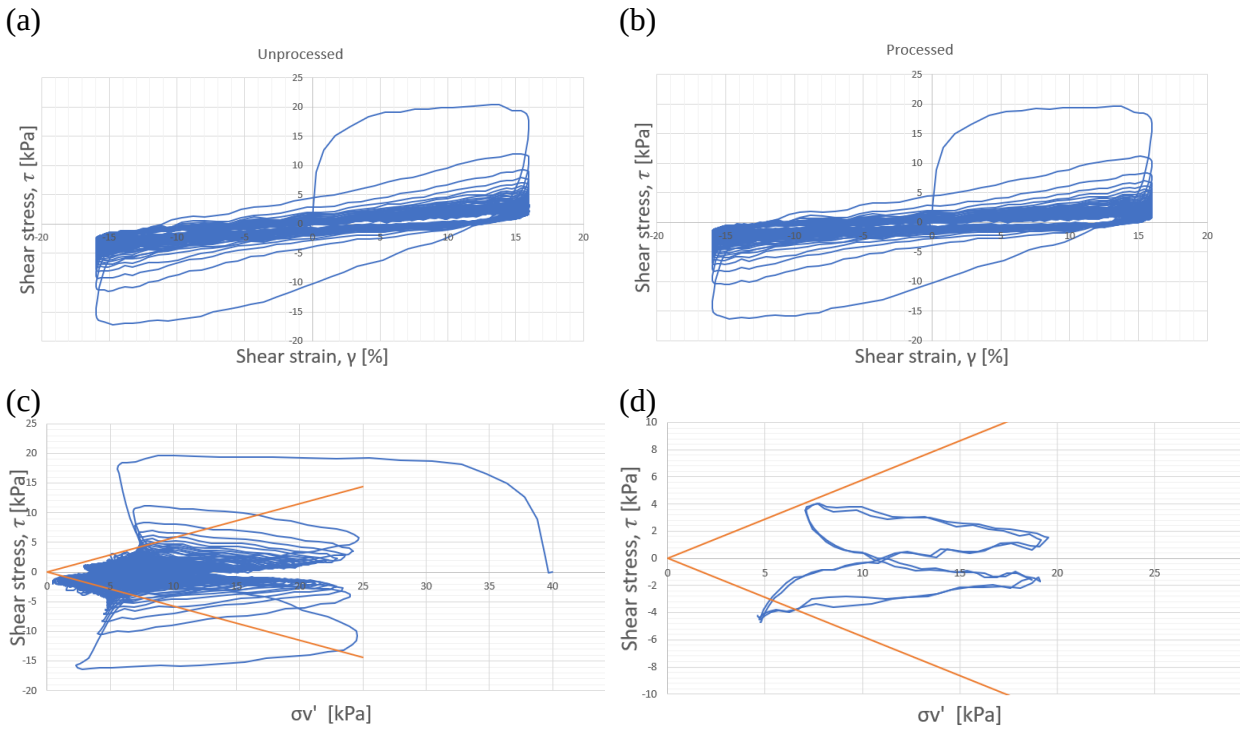

B. 1: Shows $DSS_{BF1.1.1}$ (a-b) Unprocessed and processed hystersis loops. (c) Full effective stress path in a critical state format, and (d) shows the last cycle.

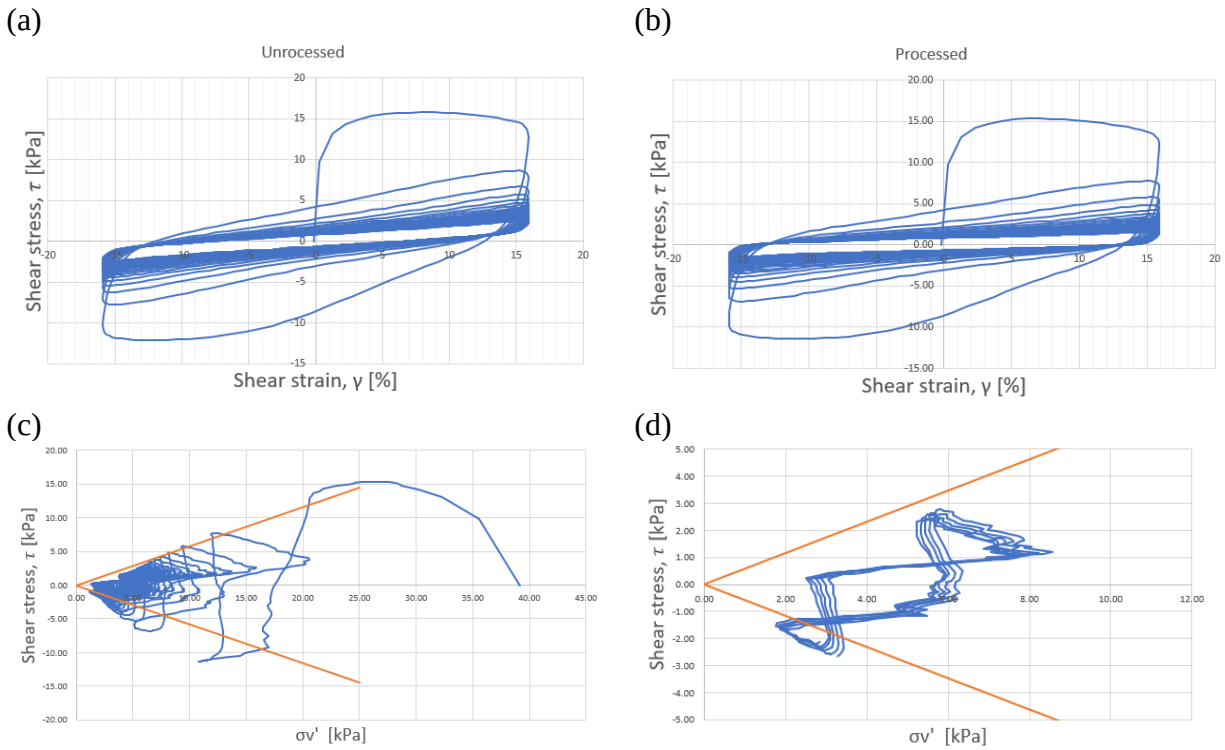

B. 2: Shows $DSS_{BF2.2.2}$ (a-b) Unprocessed and processed hystersis loops. (c) Full effective stress path in a critical state format, and (d) shows the last cycle.

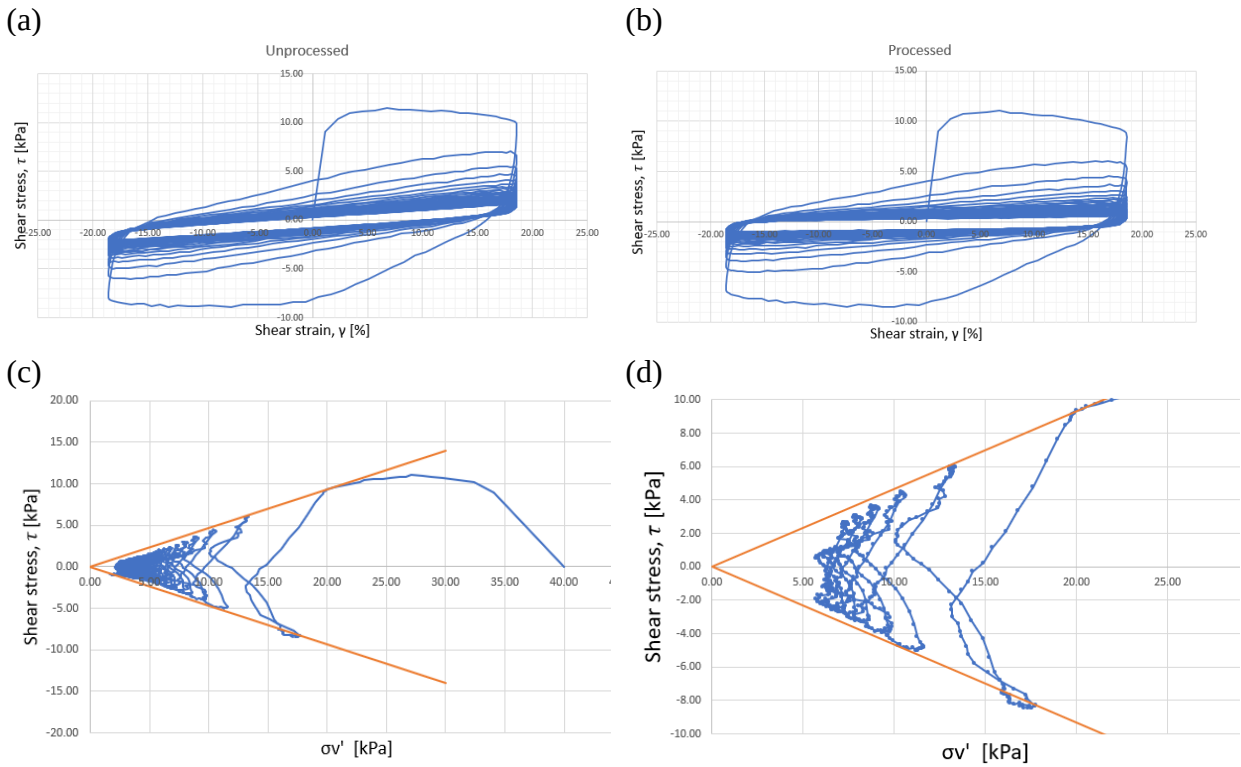

B. 3: Shows $DSS_{BF3.3.3}$ (a-b) Unprocessed and processed hystersis loops. (c) Full effective stress path in a critical state format, and (d) shows the last cycle.

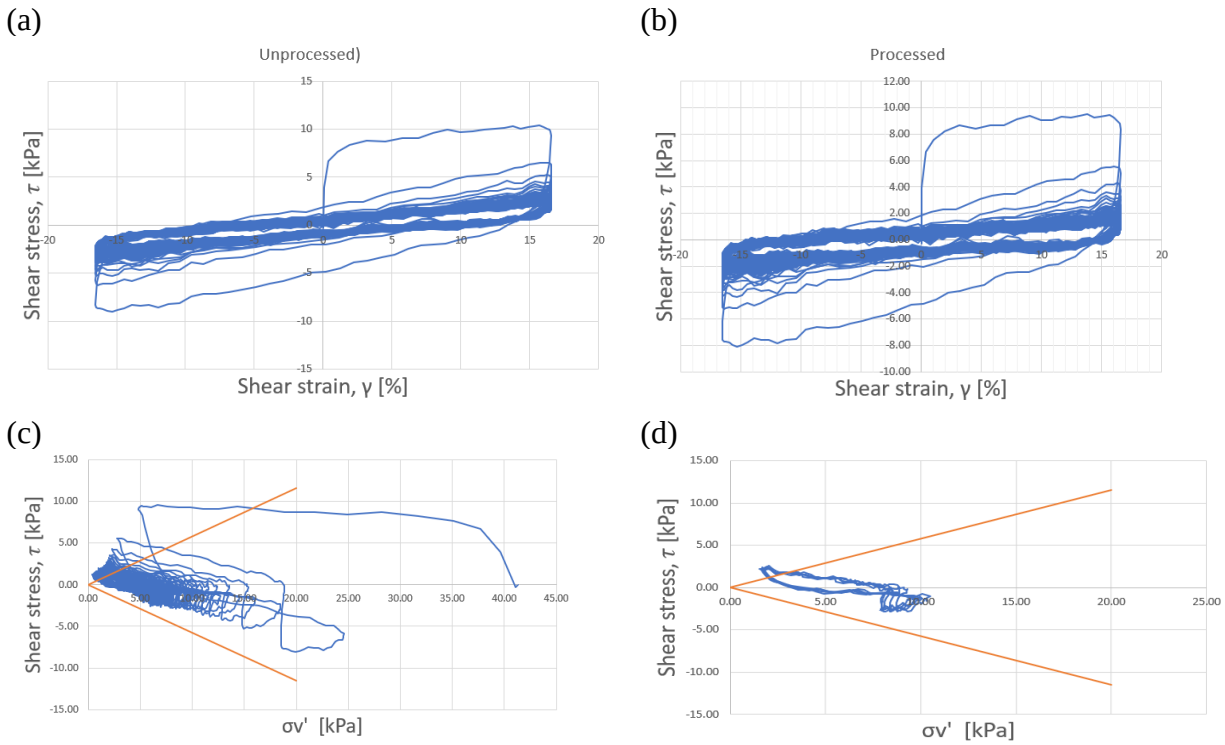

B. 4: Shows $DSS_{K1.1.1}$ (a-b) Unprocessed and processed hystersis loops. (c) Full effective stress path in a critical state format, and (d) shows the last cycle.

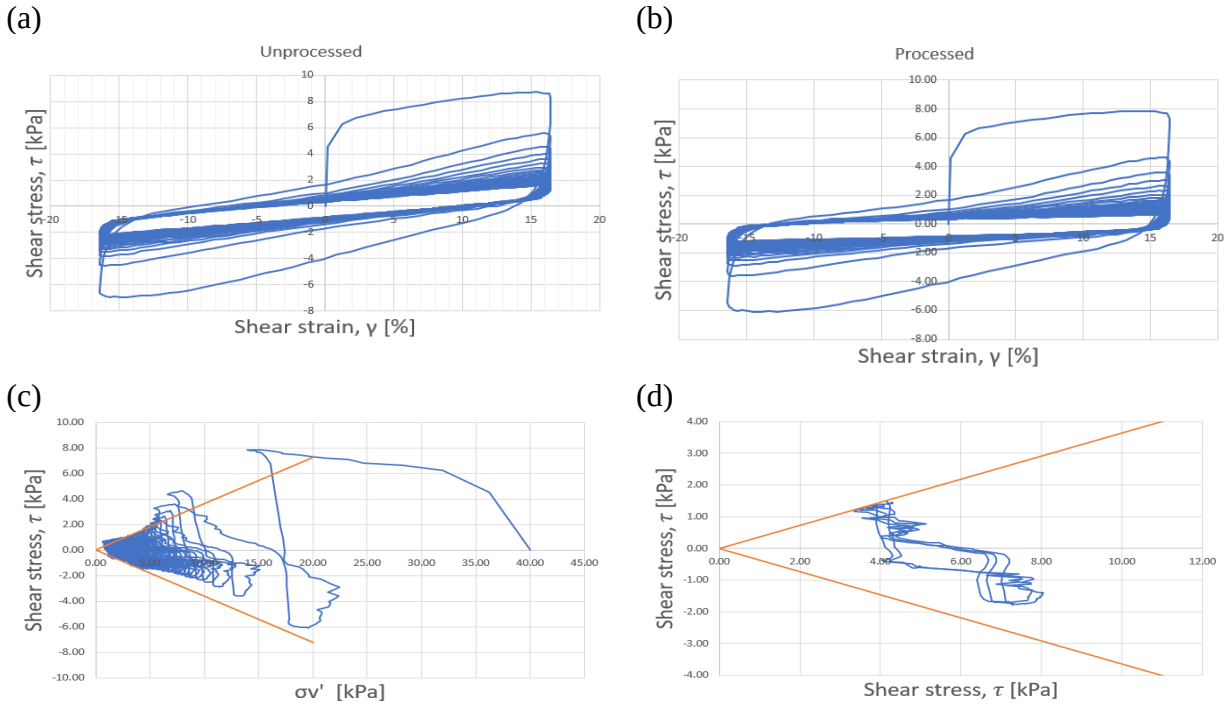

B. 5: Shows $DSS_{K2.2.2}$ (a-b) Unprocessed and processed hystersis loops. (c) Full effective stress path in a critical state format, and (d) shows the last cycle.

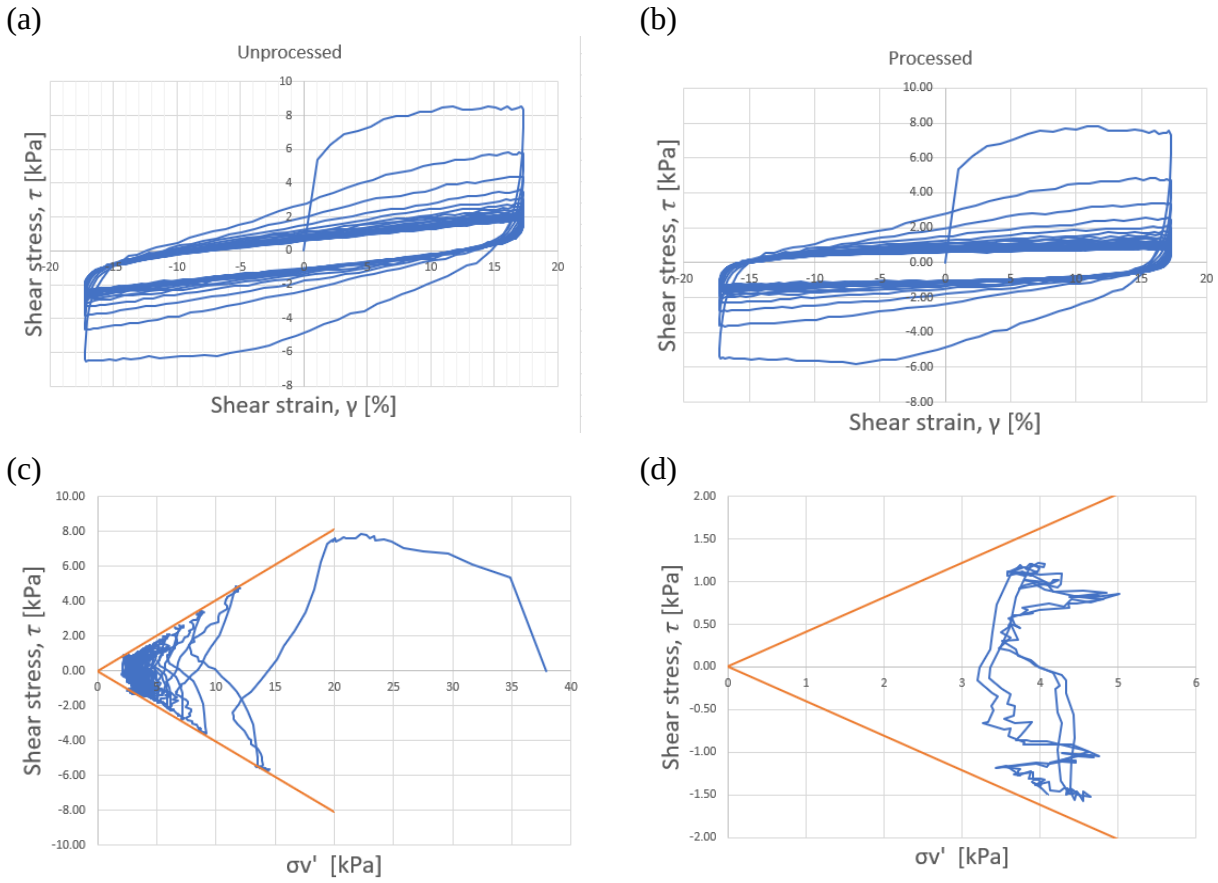

B. 6: Shows $DSS_{K3.3.3}$ (a-b) Unprocessed and processed hystersis loops. (c) Full effective stress path in a critical state format, and (d) shows the last cycle.

Appendix C

Working procedure Model tests submarine landslides

The purpose of this document is to give a working procedure for how to perform the model tests for submarine landslides. All model tests shall be performed in accordance with the outlined procedure.

In addition to the procedure below, photos should be taken from each model tests, and saved in appropriate folders.

Procedure model tests

1. Ensure appropriate working clothes. Minimum requirement is protection shoes
2. Perform a visual check of the water; ensure that the water sufficiently clear for good recordings.
3. Check whether the flume is clean from previous sliding mass. Previous sliding mass shall be removed prior to test
4. Check camera settings:
    a. Power supply
    b. Recording settings
    c. Camera positions
    d. Tilt; should be no tilt
5. Check pore-pressure readings:
    a. The tubes shall be flushed prior to testing
    b. When the tubes are placed into the sensors, the sensors shall be saturated, with water table at the edges
    c. The tubes shall be placed into the sensors with care; too fast installation may harm the sensors
    d. Check with software that all sensors show similar values
    e. Ensure that the sensors are being logged 1000 frames per second
    f. Ensure that the “write to file” is ticked on, so that a log file will be generated during the test
6. Check force-logger software
    a. Ensure that system is connected correctly
    b. Perform a test with trigger; minimum logging time 60 seconds
    c. Apply a test name of: ddmm_Material_consolidation_purpose:
        i. Material may be kaolin, sand or other material used for the test
        ii. Consolidation may be 1d, 12hr or rem (remoulded) or similar
        iii. Purpose may be Impact or runout
    d. Note: No space shall be used in logging file
    e. Important: Minimum 60s logging time
7. Ensure proper functioning and positioning of the spotlights
8. Turn main pump on

9. Remove plastic sealing from the consolidation box; Control a proper contact between the soil box and the flume
10. Fill up water to correct water elevation. The final water elevation should be 3cm less than the top elevation of the soil in the soil box. The filling should be performed in a controlled way with limited water discharge.
11. Turn main pump off
12. Remould the soil bottom and the walls in the soil box by using a U-profile. The remoulding should be performed two times. Special care to only remould the soil adjacent to the walls and the bottom of the soil box.
13. Turn spotlights on
14. Close the door at the tent. This to improve the videorecording
15. Remove internal supports inside the soil box
16. Remove the tape from the soil box. The front gate of the soil box should be kept in place by one dedicated person.
17. Start cameras. A stopwatch shall be placed in front of each camera when pressed on recording. This to synchronize the data in the post-processing.
18. Start logger-PC for pore-pressure measurements. Ensure “write to file” and 1000 frames per second.
19. Start force-logging.
20. The dedicated person at the soil box shall remove gate, and keep some distance to the soil box
21. The person inside the tent shall release soil box by pressing the weight at the flume bed. The force applied when pressing should be similar to 10kg
22. After slide event, turn off:
    a. Logger-PC
    b. Cameras
    c. Stoplights
23. Weight the remaining soil in the soil box
24. Perform water content of the soil remaining in the soil box
25. Write general observations of the slide event
26. Upload camera files in Teams in the proper folder with proper names
27. Upload force plot files in Teams in the proper folder with the proper name
28. Upload logger PC-file in Teams in the proper folder with the proper name

Appendix

Appendix